UCLouvain

AGRO LOUVAIN

Faculté des bioingénieurs

Intact desorption and soft-landing of non-covalent complexes using ToF-SIMS

Auteur : William Borsos
Promoteurs : Christine Dupont & Arnaud Delcorte
Lecteurs : Sophie Hermans & Marie-France Herent
Année académique 2020-2021
Mémoire de fin d'études présenté en vue de l'obtention du diplôme de Bioingénieur : chimie et bio-industries

Remerciements

Je tenais tout d'abord à remercier mes promoteurs, Pr. Christine Dupont et Pr. Arnaud Delcorte, de m'avoir gentiment accueilli au sein de l'équipe et sans qui ce mémoire n'aurait pas pu être réalisable. Leurs aides et éclaircissements m'ont grandement aidé à l'élaboration de ce travail de fin d'étude.

Je voulais ensuite énormément remercier mon encadrant, Vincent Delmez, qui m'a suivi, soutenu et encouragé au jour le jour ce qui m'a permis de continuer ce travail avec plaisir tout au long de l'année même dans des moments plus difficiles. Grâce à lui, j'ai pu apprendre beaucoup sur la vie de chercheur qui pourrait m'intéresser pour plus tard. Il a passé un temps considérable à m'aider et me conseiller sur la réalisation de ce travail et pour cela, je lui suis extrêmement reconnaissant !

Je remercie aussi toute l'équipe du C2 que j'ai appris à connaître tout au long de l'année et qui m'a, elle aussi, apporté son aide lorsque j'avais des questions d'ordre plus pratiques. Un tout grand merci à Claude Poleunis qui m'a patiemment appris à utiliser le ToF-SIMS et à Thomas et Benjamin qui m'ont aidé à corriger certaines parties de ce manuscrit.

Je voudrais bien évidemment remercier Pr. Sophie Hermans et Pr. Marie-France Herent d'avoir bien voulu faire partie de mon jury ainsi que pour leur temps passer à lire mon mémoire.

Je tiens aussi à remercier mes co-mémorants et partenaires de bureau, Maureen et Hadelin avec qui l'ambiance est toujours très bien passée. Un énorme merci à Antoine qui n'a pas arrêté de prendre des nouvelles alors qu'il avait déjà fini son master !

Enfin, je tenais à remercier Maria, qui m'a aidé et soutenu en moments de rush, ma famille et mes amis qui ont toujours été là quand il fallait, que ce soit pour m'aider ou pour décompresser ! Merci à Hélène qui m'a même motivé à travailler un peu en vacances.

Merci enfin à tous ceux qui prendront la peine de lire mon mémoire, j'espère que vous l'apprécierez autant que j'ai apprécié l'écrire !

Abstract

Nowadays, surfaces biofunctionalization is a subject of utmost interest, especially in medical and paramedical applications. Even if the immobilization of biomolecules from aqueous solutions has already shown efficiency, these methods suffer from negative aspects. Among others, the issues intrinsic to the drying process, such as the denaturation of the immobilized proteins, the limitation to monolayers and the poor control of spatial delivery, can reduce the achievable functions of the engineered biomaterials. Hence, researches and methods are increasingly being developed to counteract these drawbacks.

This master thesis investigates the detection and transfer of non-covalent complexes, using small bismuth and large argon cluster ion beams, with a time-of-flight secondary ion mass spectrometer (ToF-SIMS). The ultimate goal of this study is to succeed in the intact desorption from a surface and the soft-landing onto another without breaking weak interactions linking the two involved partners, in addition to covalent bonds. Two non-covalent systems have been studied in different conditions. These systems are, firstly, vancomycin, a glycopeptide antibiotic, which can specifically bind to small (acetyl-L-Lys-)D-Ala-D-Ala polypeptide and to itself by forming dimers and secondly, chromium trifluoroacetylacetonate ($Cr(tfac)_3$), *i.e.* more robust metallic complexes. Various parameters were tested: primary ion beam nature, cluster size and energy, sample thickness and substrate's hardness which are among the most impactful ones.

First, some reference analyses were achieved using Bi_5^+ and $Ar_{1500-3000-5000}^+$ beams to (i) make sure these complexes could be detected (and so desorbed intact) by ToF-SIMS and (ii) to identify their mass spectral signature. Second, these non-covalent complexes were transferred using large $Ar_{3000-5000}^+$ beams from a target, a silicon wafer on which high quantities of complexes have been deposited, onto a cleaned surface, the collector. These collectors were finally analyzed to assess if these complexes were transferred intact. A study on vancomycin fragmentation has also been achieved in function of the layer thickness, confirming previous theories and bringing additional information on ionization mechanisms of vancomycin pseudomolecular ions. Using optimized parameters, all complexes were successfully detected confirming that non-covalent complexes can be desorbed intact using ToF-SIMS. After being transferred, $Cr(tfac)_{1-2}$ complexes were detected on the collectors in positive mode. For the vancomycin-ligand complexes and the vancomycin dimers, it resulted that these were too weakly bonded to allow detection after an additional ion impact compared to the analyses. Nevertheless, intact vancomycin molecules were transferred with a semi-circular deposition pattern confirming that large argon clusters, with their low energy per atom, reduced significantly the molecules fragmentation upon ion impacts.

List of abbreviations

AA	D-Alanyl-D-Alanine
amu	Atomic Mass Unit
DD	Dried Droplets
ESI	Electrospray Ionization
GCIB	Gas Cluster Ion Beam
IEP	Isoelectric Point
KAA	Acetyl-Lysine-D-Alanine-D-Alanine
LMIG	Liquid Metal Ion Gun
MALDI	Matrix Assisted Laser Desorption Ionization
M-L	Metal-ligand
MS	Mass Spectrometry
NCI	Non-Covalent Interaction
pMS	Preparative Mass Spectrometry
SC	Spin-Coating
SDS-PAGE	Sodium Dodecyl Sulfate-PolyAcrylamide Gel Electrophoresis
SL-pMS	Soft-Landing Preparative Mass Spectrometry
UHV	Ultra High Vacuum
V	Vancomycin
vdW	van der Waals

Contents

1 Introduction

1.1 State of the art

1.1.1 The importance of surfaces

Interfaces are ubiquitous in the world and govern an impressive amount of phenomena in both biological and inorganic systems. But what exactly are interfaces and why are they so interesting from a scientific point of view? An interface or a surface is a region, composed of a small number of atomic layers, delimiting two distinct phases and where properties will be affected by physical or chemical changes with respect to one or the other of the two phases considered. Because different gases mix when put together, there only exist 5 types of interfaces ; solid-solid, solid-liquid, solid-gas, liquid-liquid and liquid-gas.[1-4]

In the bulk, *i.e.* in the mass of a material, molecules surrounded by others are energetically favoured over those at the surface which are only partially encircled by others. Figure 1.1 shows that molecules are bound to each other thanks to attractive interactions (van der Waals forces, hydrogen bonding, etc). If they were not attracted to each other, everything would be in the gas phase since condensed matter would not exist. [1, 5]

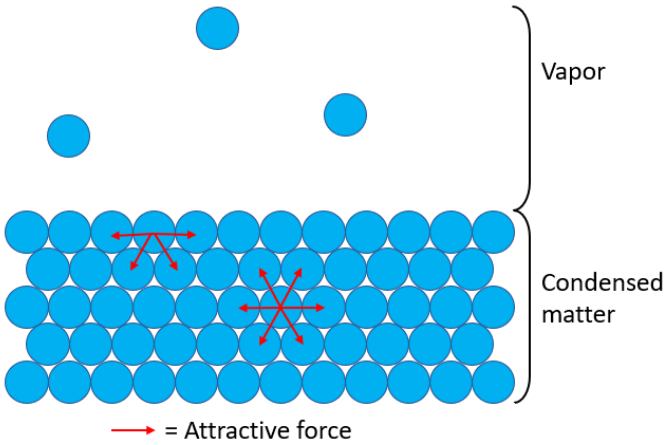

Figure 1.1: Schematic molecular structure of an interface between a gas and condensed matter (inspired from [1]).

Four consequences ensue from this lower coordination number at interfaces [6] :

- Since intermolecular forces are unbalanced at interfaces, the surface region of a material is at relatively high energy compared to the bulk. The driving force for phenomena taking place at interfaces is thus the reduction of this surface energy;
- The surface electronic structure is quite different from that of the bulk;
- Since atoms may diffuse or move at the surface, the surface crystallographic structure may differ from that of the bulk;
- Most often, the adsorption of other atoms or molecules is favoured at interfaces as it induces a decrease of the surface energy. If a novel chemical bond is formed it is called "chemisorption" whereas if weak van der Waals interactions are at play, it is named "physisorption". This explains for example why contamination by small molecules is always present on solid surfaces.

For a given mass, the surface area increases with subdividing solid materials and with porosity, it is therefore crucial to understand and control the behaviour of materials such as colloidal systems, powders or porous solids since they develop huge specific surface areas, *i.e.* the surface area developed by a solid divided by its mass. [1, 7]

With this in mind, it is obvious that surfaces play a major role in many phenomena and that it is necessary to be able to characterize but also to finely tune and control their properties. Indeed, the success of a large number of applications in diverse fields including heterogeneous catalysis, biocompatible materials, nanomaterials, semiconductors, adhesives or surface functionalization rely on the surface properties of the material.[8]

1.1.2 Surface biofunctionalization

By optimizing and/or adding specific features, the surface properties and performances can be improved and new functions provided. This process is called surface functionalization. When the surface is functionalized with biomolecules, *i.e. "molecules produced by living cells"*[9] (including proteins, carbohydrates, lipids and nucleic acids), one speaks of biofunctionalization. Once a natural or synthetic material is treated that way, it becomes a biomaterial and can thus interface with biological systems to evaluate, treat, augment or replace tissues, organs or functions of the body with appropriate host response in a specific application (see definitions of "biomaterial" and "biocompatibility" in [9]).

A myriad of applications relying on biomaterials are already in use especially in medicine and paramedical fields, and many more are to come, reinforcing the interest of research in this field. Figure 1.2 shows some examples of tissue repair applications in

different types of muscle [10]. Biofunctionalized surfaces can also be used for biosensing via antibodies immobilization [11]. Enzymes, *i.e.* proteins that present catalytic properties, can also be immobilized at surfaces to form biocatalysts used, for example, in the synthesis of fine chemicals [12].

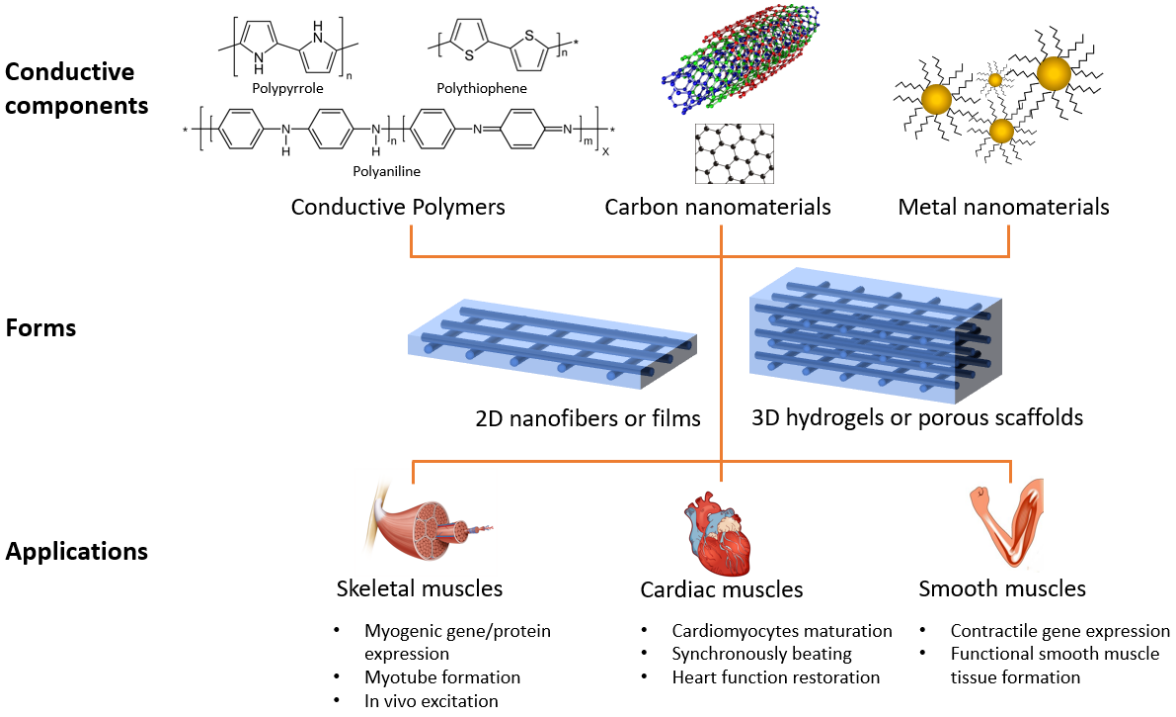

Figure 1.2: Examples of components, forms and application in muscle tissue repair (inspired from [10]).

Biofunctionalized surfaces or materials can be produced from solution through different methods : direct adsorption, immobilization methods, self-assembled monolayers, layer by layer assemblies etc [13]. Only the direct adsorption method will be detailed and discussed, the other techniques being less relevant to what follows.

1.1.2.1 Direct adsorption from aqueous solution

As previously mentioned, since intermolecular forces are unbalanced at interfaces, the driving force for surface phenomena is the reduction of the interfacial energy. Indeed, the process of adsorption tends to lower the interfacial free energy (or surface tension) in a thermodynamic sense. This makes direct adsorption from solution spontaneous in almost all cases and thus by far the easiest way to immobilize proteins on solid surfaces. From a biophysical point of view, proteins can adsorb on surfaces thanks to their "large" size, amphiphilic nature and their relative ease of changing conformation. The adsorption process will depend on a large variety of factors. [13]

In aqueous solution, solid surfaces cannot easily resist protein adsorption. Proteins which are amphiphilic molecules, tend to fold in a way that prevents the apolar moieties to be in contact with the surrounding water molecules. These moieties are thus mostly found in the centre of the protein structure. When they approach surfaces, adsorption can be accompanied by a conformational change. For hydrophilic surfaces, the terms "hard" and "soft" proteins, indicating their ease of conformational change and thus of adsorption, have to be introduced. Soft proteins will easily undergo conformational change and thus adsorb while hard ones significantly less. When it comes to hydrophobic surfaces, any type of protein will very likely adsorb thanks to the dehydration of the surface and of the apolar groups in the protein still contacting water. This dehydration outweighs electrostatic repulsion between the protein and the surface. [14]

However, despite being a simple and straightforward approach for the immobilization of proteins, some disadvantages inherent to the technique can be highlighted:

- This method is restricted to the construction of monolayers. Indeed, proteins cannot interact with themselves in the same stabilizing way as with surfaces. Once the surface is completely covered, the proteins have no room to interact with it, decrease their internal energy and thus adsorb. [15];
- Adsorption may lead to :
  - protein denaturation because of their likely change of conformation [16];
  - the protein active site being hidden between them and the surface due to uncontrolled orientation during immobilisation, rendering them inactive. [15].

Finally, drying issues are quite omnipresent when relying on adsorption from aqueous solution. Indeed, during the surface dewetting process, proteins can undergo reorganization leading to uncontrolled spatial distribution and/or conformational changes and thus denaturation [17]. In order to overcome at least some of these limitations, a series of solvent-free deposition methods, in addition to other strategies mediated by aqueous solution, have been developed. Among them, preparative mass spectrometry has shown promising results.

1.1.3 Preparative mass spectrometry

In preparative mass spectrometry (pMS) techniques, the surface of a solid is functionalized by the deposition of mass-selected molecular ions. These techniques are thus no longer using mass spectrometers for their primary analytical function but to create new nanostructured surfaces. pMS allows a dry deposition of molecules on surfaces, and therefore overcome dewetting issues that are encountered with solvent-based methods. The principle of the method, shown in Figure 1.3, is as follows. First a ionization source - such as electrospray ionization (ESI), gas condensation sources, laser ablation,

matrix assisted laser desorption ionization (MALDI) or electron ionization (EI) [18] - generates ion beams of molecules and molecular fragments of the sample in a wide mass range. Second, instead of being analyzed to produce a mass spectrum, these ionized molecules can be separated thanks to a mass filter, in order to obtain a beam of the molecular ion of interest. The mass filter is, in effect, a mass spectrometer analyser controlled in such a way to allow only ions of interest to pass through by selecting the desired mass to charge (m/z) ratio. Finally, this selected ion beam is focused onto the surface of a material in order to create nanostructures. Some electromagnetic optics to transfer and guide the ions through the instrument before and after the mass filter can also be present [19]. The whole process is carried out under ultra high vacuum (UHV) in order to increase the mean free path of the selected ions, *i.e.* decrease collisions between them and molecules from the gaseous environment. [20]

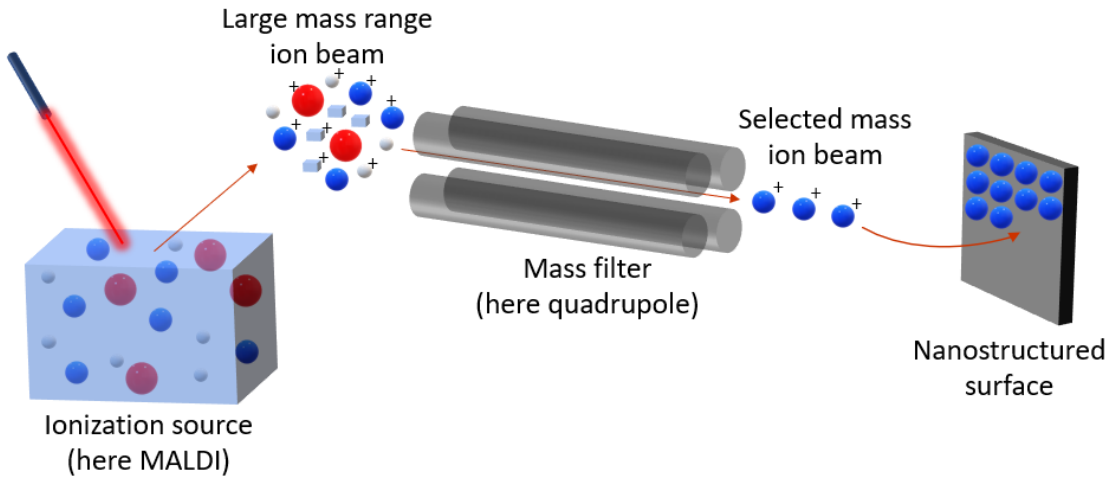

Figure 1.3: Schematic representation of preparative mass spectrometry using in this case MALDI as ion source and a linear quadrupole as mass filter (inspired from [18]).

At first glance, one can already imagine that more robust molecules are more likely to reach the surface intact than more fragile ones. However, by optimizing the conditions, it is possible to attain a soft deposition regime that allows the intact immobilization of fragile molecules such as proteins and peptides. Such conditions have led to a sub category of pMS, soft-landing. Soft-landing preparative mass spectrometry (SL-pMS) is the deposition of an incident species on a surface with a translational kinetic energy low enough to prevent its fragmentation upon impact. In 1996, Benner and Siuzdak demonstrated the deposition of electrosprayed viruses that retained their 3D-structure and viability [21]. In 2003, a study showed that soft-landed trypsin and lysozyme retained their biological activity and that it was also possible to soft-land peptides on liquid surfaces [22]. Another article showed in 2008 that the infrared

spectra of soft-landed peptides presented helical conformation peaks - these α-helixes playing an important role in the protein structure and function [23]. In 2012, Deng et al. demonstrated electrospray ion beam deposition of selectively folded and unfolded cytochrome c protein ions on solid surfaces [24]. Some of these example are illustrated in Figure 1.4.

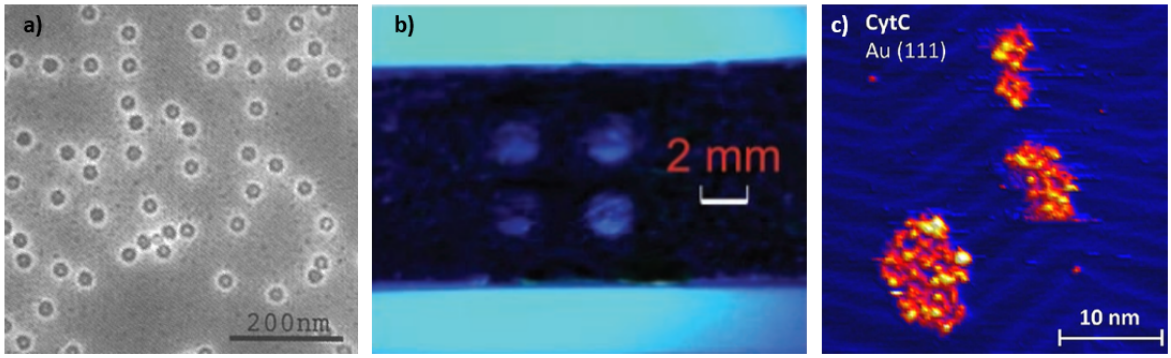

Figure 1.4: a) Transmission electron microscopy image of soft-landed rice mottle yellow virus [21]. b) Photograph of a microarray of four proteins soft-landed onto a gold substrate [22]. c) Scanning tunneling microscopy topography of cytochrome C monomers and dimers on gold [24].

In addition to retaining the protein/peptide 3D structure and activity, SL-pMS offers several advantages over solvent-based methods [19]:

- It allows unparalleled control over the size, the composition and the surface coverage of the delivered ions;
- It permits to avoid complications resulting from dewetting, *i.e.* clumping, or contaminant presence (solvent, counterions);
- In theory, there is no limit to the deposited amount, in contrast to the monolayer limitation in direct adsorption.

Hence, bringing new possibilities, soft-landing preparative mass spectrometry is a promising additional technique to the existing surface (bio)functionalization methods.

1.1.3.1 Electrospray Ionization (ESI)

Since electrospray ionization is the most common ionization source for SL-pMS and because it was used during the master thesis project for mass spectrometry, it will briefly be detailed hereafter.

To explain the ESI technique, we first need to explain the underlying principles of mass spectrometry (MS). MS is an analytical technique that measures the mass to

charge ratio (m/z) of ions (molecular ions and fragments of them) and thus identifies the composition of a sample. Mass spectrometer are composed of four main components and their basic principle is as follows. An ionization source produces ions from the sample. Then these ions are analyzed and detected against their mass. Finally a data processor/digitizer produces a mass spectrum. [25]

Invented in the late 80s, ESI is one of the several ionization methods used overall for MS of non volatile molecules. It is, in effect, the softest one since it allows the detection of macromolecules bound by non-covalent interactions in the gas phase. The principle, shown in Figure 1.5, is the following one ; the sample is ejected, as a spray of multiple charged droplets, from a narrow capillary at high voltage. The solvent in these droplets gradually evaporates leaving them increasingly charged. When the number of charge exceeds the Rayleigh limit, *i.e.* the maximum amount of charge a liquid droplet can carry, the droplet explodes into microdroplets from which the ionized analytes are separated. These gas phase ions are then analyzed. When used for pMS, a collector substrate is placed after the mass selection device instead of a detector. [18, 25]

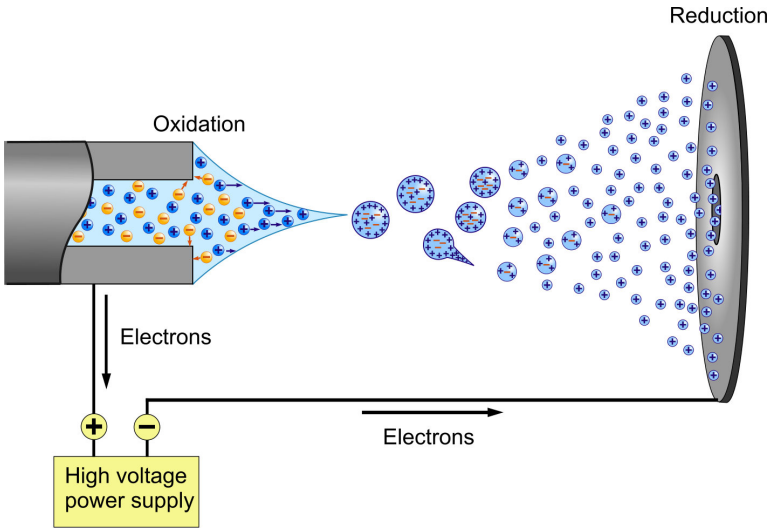

Figure 1.5: ESI schematic representation in positive mode and under high voltage. [26]

Although several studies have shown that SL-pMS is relatively efficient for the deposition of various species, ranging from intact viruses to small metal clusters, there are still some limitations such as the low ion current (at the source and after the mass separation stage) leading to extremely low deposition rate [18]. In the continuity of exploring SL-pMS methods, this master thesis will investigate the feasibility of non-covalent complexes desorption from a surface and their soft-landing on another by using time-of-flight secondary ion mass spectrometry. The following introductory sections will be devoted to the state of the art of this MS technique, the existing non-covalent interactions and the contextualisation of two molecular systems studied during the academic year. Then, the experiments and results will be discussed.

1.1.4 Time-of-Flight Secondary Ion Mass Spectrometry

1.1.4.1 Principle

Time-of-flight secondary ion mass spectrometry (ToF-SIMS) is a surface-sensitive analytical technique that has been developed in the late 60s [27]. Figure 1.6 shows a picture of a recent ToF-SIMS instrument and a schematic representation of its internal components.

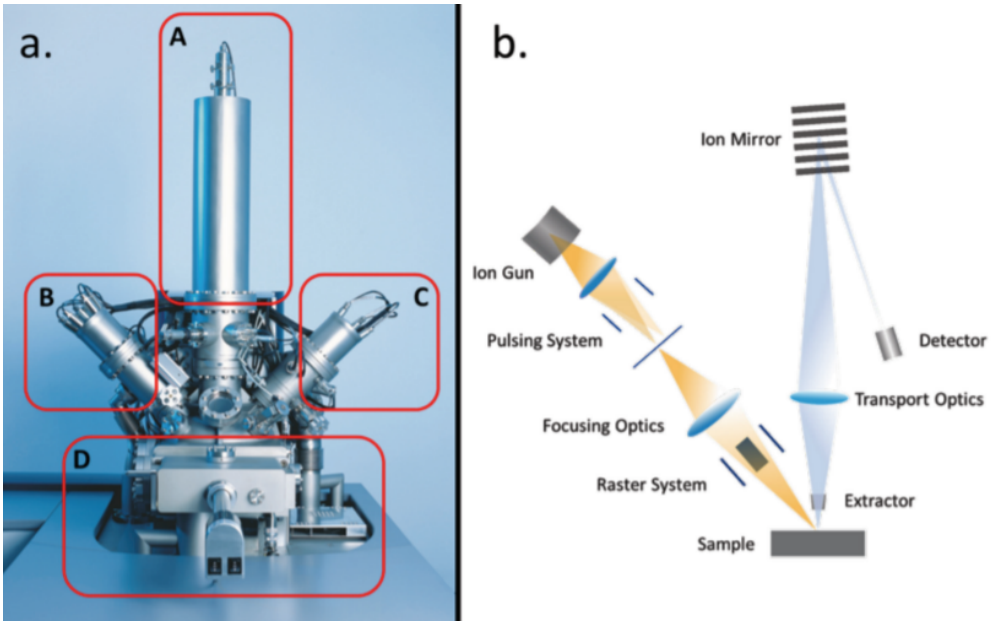

Figure 1.6: (a) A ToF-SIMS V IONTOF instrument with the four principal components labeled, where A is the ToF analyzer, B & C are the different ion sources for sputtering and/or analysis and D is the load lock for introducing samples. (b) A schematic representation of some of the internal components of a ToF-SIMS instrument with parts labeled. [28]

The ToF-SIMS principle is quite easy to conceptualize even if there are hidden complexities. Originally, an energetic (1 to 25 keV) pulsed monoatomic ion beam, whose ions are called primary particles, is focused from the ion source on the sample surface. The impact of the ions on the surface induces a collision cascade (billiard-ball type) between the atoms of the solid during which the kinetic energy of the primary ions is transferred among them. Some of these collisions return to the surface region leading to the sputtering of fragments and molecules, referred to as the secondary particles, in the gas phase. The precise depth of origin of these secondary particles depends on the primary beam nature, energy and angle but it is limited to the topmost layers of the sample. This is depicted in Figure 1.7. [27]

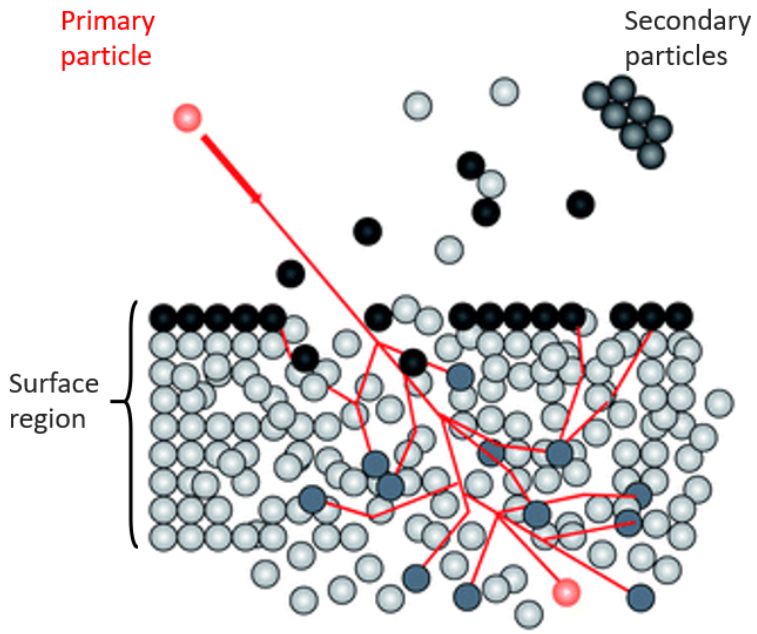

Figure 1.7: Schematic representation of the collision cascade when monoatomic ion beams are used. [29]

A very small fraction of these secondary particles are ionized in the emission region (in or just above the surface) through electron exchange processes, acid base reactions or even cationisation or anionisation of neutral species. If the dose of primary ions is quite low (maximum 10^{13} ions/cm^2), not even 1% of the topmost surface atoms or molecules receive an impact, leaving a surface undamaged from an analytical point of view (static SIMS). For conductive materials, surface charging cannot happen at this scale but for insulators this is another story. Because of the input of positive charges and secondary electrons emission, their surface potential increases very rapidly by several hundreds of volts. This has been resolved by using low energy electron flooding on the surface of the sample. [27]

The charged secondary particles emitted from the surface are then extracted into the time-of-flight analyzer. A chosen positive or negative electric field is applied, accelerating anions or cations respectively while providing them the same kinetic energy. Then, they travel through a field freed zone where they are separated according to their m/z ratio. The equation 1.1 derived from the kinetic energy equation expresses the flight time t.

$$t = L(\frac{m}{2zV})^{1/2} \tag{1.1}$$

Where L is the flight path and V the acceleration potential. Since charged particles usually carry only one charge in SIMS, they are thus separated according to their mass ; the lighter ions being the faster ones. Because of slight differences between identical-mass particle velocities, a reflectron or ion mirror is used to refocus them in time on the detector. The reflectron is a zone in which an increasing retarding field is applied so

that the more energetic ions will penetrate deeper than the less energetic ones before being reflected. Thanks to this ion mirror, the ions are reflected back in the other direction and identical-mass ions arrive at the exact same time on the detector, which is increasing the mass resolution. [30, 31] This can be seen on Figure 1.8.

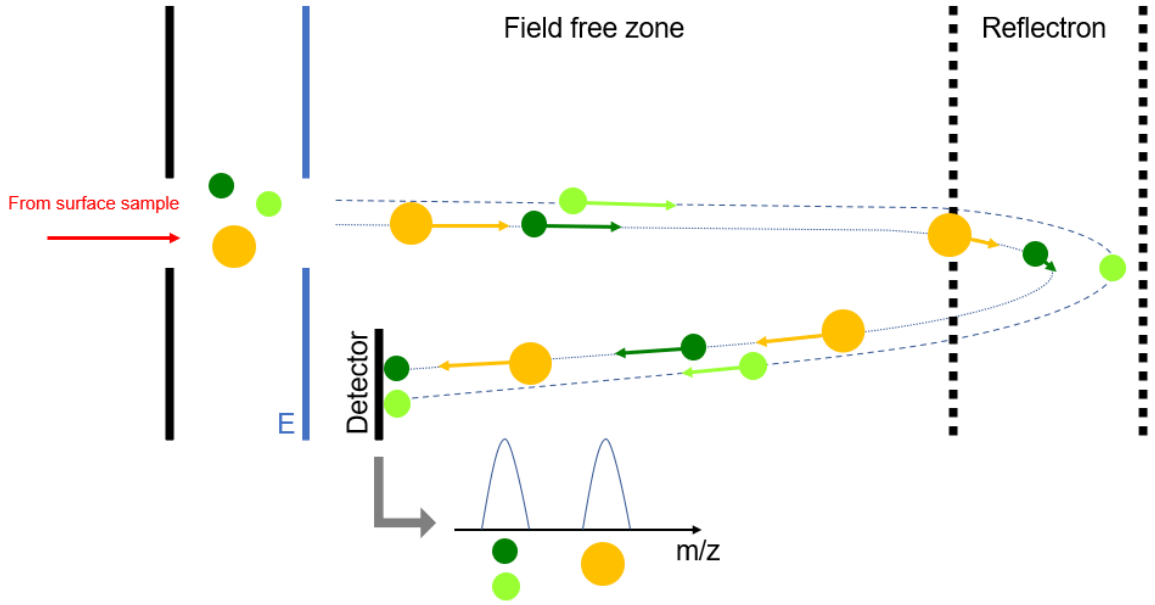

Figure 1.8: Schematic representation of the time-of-fight analyzer process with a reflectron. The yellow ball represent a high mass particle and the greens balls represent identical-low mass ones. The different greens indicate different initial potential energies, the lighter-green ball being the more energetic ion. Inspired from [30]

Finally, a mass spectrum is obtained. All peaks correspond to ionized molecules or fragments and are analytically helpful to characterize the sample. Their intensity is described by the equation 1.2 [27] :

$$I_m = I_p \, y_m \, \alpha^+ \, \theta_m \, \eta \tag{1.2}$$

Where I_m is the secondary ion current of species m, I_p is the primary particle flux, y_m is the sputter yield, α^+ is the ionization probability, θ_m is the fractional concentration of the species m in the sample surface and η is the transmission of the analysis system. In this equation, only valid for atomic ion beam, the sputter yield and the ionization probability are the two fundamental parameters. "y_m is the total yield of sputtered particles of species m, neutral or ionic, per primary particle impact" [27]. This parameter increases non-linearly with the primary particle mass, charge and energy (sputtering occurs at about 20-40 eV and is maximal between 5 and 50 keV). y_m is also monotonically increased by increasing incident angle and has its maximum around 60-80° to the surface normal. Since ionization is strongly affected by

electron and/or cation exchange mechanisms between the outgoing and surface particles the electronic and chemical state of the surface are critical in sputtering events and ionization probability. This is shown in Table 1.1 comparing different sputter yields of the M^+ species from pure metallic materials and from corresponding metallic oxides. The strong differences between the sputter yields, in these particular examples, are mostly due to the oxidation state of the metal atoms and thus to their electronic environment.

Table 1.1: Elemental positive secondary ion yield from a number of metals compared to the corresponding oxides. Inspired from [27]

Metal	**Clean metals M^+ yields**	**Oxide M^+ yields**
Al	0.007	0.7
Si	0.0084	0.58
Ti	0.0013	0.4

1.1.4.2 ToF-SIMS analyses

Different types of measurement and data acquisition can be conducted using a Tof-SIMS instrument. Four of them will be described in this section and are illustrated in Figure 1.9.

1. **Mass spectrum**
   This most common analysis technique allows to characterize the surface of a very small region of the sample (from 50x50 µm² to 500x500 µm²). This so-called "static SIMS" mode is the simplest application of what was presented in the previous section. The obtained mass spectrum (example in Figure 1.9a) is generally presented as the intensity, *i.e.* the number of ion detected, as a function of the m/z ratio. Since the ion charge is usually of 1 in either of the two polarities, the x-axis can also simply be the mass (in amu).

2. **2D imaging** [33, 34]
   In this mode, the primary ions beam scans the surface analyzing small regions one after the other. The obtained chemical information is then gathered to reconstruct images of the intensity (represented as the color in the image) of a given-mass secondary ion (or more) as a function of its position on the sample surface. Since it provides information about the distribution of chemical compounds in cells and tissues at the subcellular spatial resolution, 2D SIMS imaging has become a valuable tool in biological, medical and pharmaceutical researches. SIMS allows the identification of multiple biomolecules in a single experiment and, unlike fluorescence or electron microscopy methods, the target analytes do not have to be known a priori. An example of 2D SIMS image is shown in Figure 1.9b.

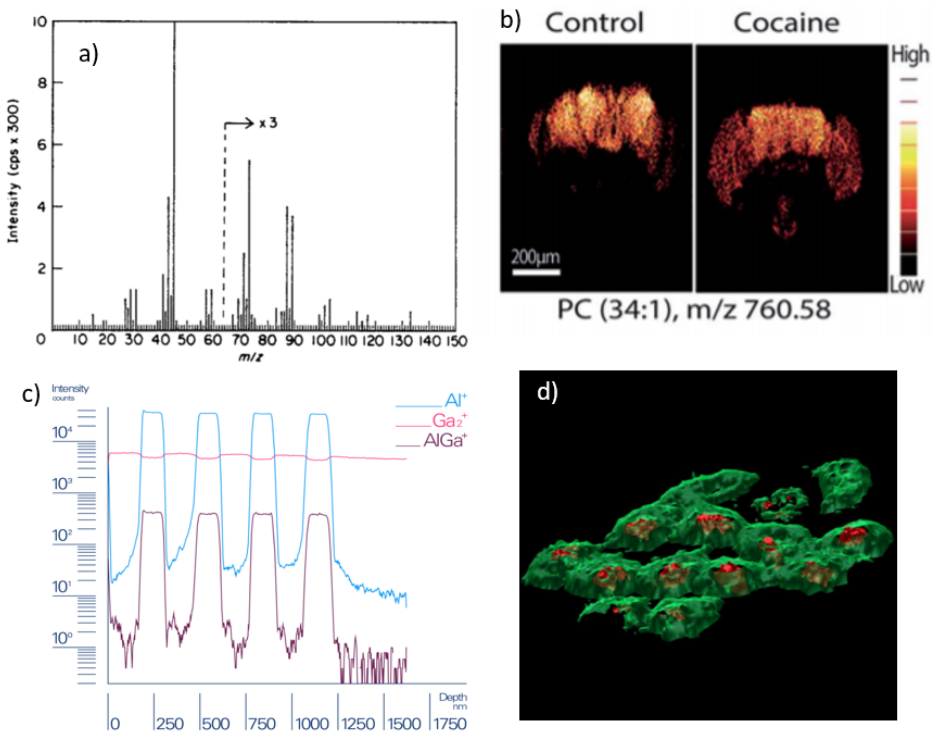

Figure 1.9: (a) SIMS spectrum of poly(ethylene oxide) using Ar^+ [32]. (b) ToF-SIMS image of phosphatidylcholine in control and cocaine treated drosophila brain [34]. (c) Depth profile through a GaN/AlGaN multilayer system using oxygen for sputtering [35]. (d) 3D visualisation of the membrane (green, m/z 184.1, phosphocholine) and nucleus (red, m/z 136.1, adenine) chemistry in the frozen-hydrated HeLa-M cells [36].

3. **Depth profiling** [31, 33]
   As it can be seen in Figure 1.6a, there are generally more than one ion source in the SIMS device. On this picture, one ion source is for analysis (at low primary ion doses) and the other one is for material sputtering (at higher doses), *i.e.* digging a crater into the sample. Both ion sources can be used in an alternated fashion, *i.e.* the dual-beam mode, to produce a depth profile. As this technique modifies the surface of the sample quite severely, it can no longer be referred as "static SIMS" but rather as "dynamic SIMS". An example of a SIMS depth profile is shown in Figure 1.9c.

4. **3D reconstruction**
   This technique is the combination of the two previous ones. While one ion source is digging the sample surface, the other one analyzes it to produce a 2D image. Together, they allow reconstruction of complex structures in three dimensions. Figure 1.9d shows a 3D-image of HeLa-M cells, *i.e.* cells derived from cervical cancer.[36]

1.1.4.3 The clusters revolution

In classical secondary ion mass spectrometry, energetic primary ion beams were composed of monoatomic ions such as Ga^+, Cs^+ or Ar^+ and used to analyze inorganic materials. However, analysis of organic, polymeric and biological materials has been historically limited by low secondary ion yields and beam induced damage effects that result from the use of these ion beams. The "static limit" is the maximal dose of primary ions (often reported as 10^{13} ions/cm^2) to keep the sample surface undamaged. Once above this limit, sensitivity decreases and prevents depth profiling. One revolutionary solution to these limitations is to use small polyatomic aggregates, better known as clusters, instead of monoatomic ions in the primary ion beam. [27, 33, 37] When a cluster ion strikes a surface, it breaks apart and each atom retains only a fraction of the cluster initial energy as described in the equation 1.3 [33].

$$E_c = E_0 \frac{M_c}{M_t} \tag{1.3}$$

Where E_c is the energy of a constituent atom after collision, E_0 is the cluster energy before impact, M_c is the mass of that particular constituent and M_t is the total mass of the polyatomic ion. The result of this fragmentation on impact is a significant reduction in penetration depth of the ion since each individual atom carries only a part of the total kinetic energy (see Figure 1.10 showing the differences between monoatomic and cluster beams). Two consequences arise from this. First, the damage is more localized in the surface region preserving the chemical structure of subsurface regions and thus ensuring satisfactory conditions for depth profiling. Second, since more atoms are striking the sample simultaneously, a larger fraction of the deposited ion energy is used for sputtering leading in the non linear enhancement of the sputter yield, y_m, (*i.e.* sputter yield of $C_n^+ >> nC^+$ [39]). Figure 1.10 also shows that more secondary ions are sputtered when using cluster beams. [33, 37, 38] The depth profiling of soft materials such as organic, polymeric and biological systems, is therefore accessible and now referred to as *molecular depth profiling* [33].

Clusters primary ion sources such as C_{60}^+, Au_3^+, SF_5^+, Bi_n^+ and Ar_n^+ have resulted in significant enhancement in secondary ion yield and decreased beam-induced damage.[33] Note that there is a distinction between "small" and "large" clusters. Bi_{3-5}^+ for instance is not suitable to perform depth profiling without damage as they still penetrate deep and cause a lot of damage in the sample. However, they give very high secondary ion yields when used as analysis beam. In contrast, $Ar_{500-5000}^+$ and, to a lesser extent, SF_5^+ and C_{60}^+ allow for deep molecular profiling of organic compounds. For the latter two, there is also a mass matching effect. Indeed, light ions colliding one by one with carbon will transfer more of their energy and be stopped less deeply. This is illustrated in Figure 1.11. [40]

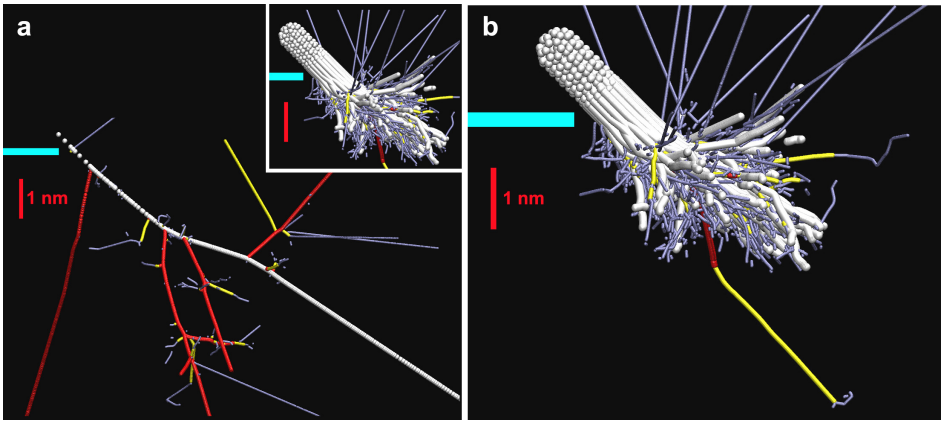

Figure 1.10: Modelling of impact depth using (a) monoatomic ion beam and (b) cluster ion beam [38]

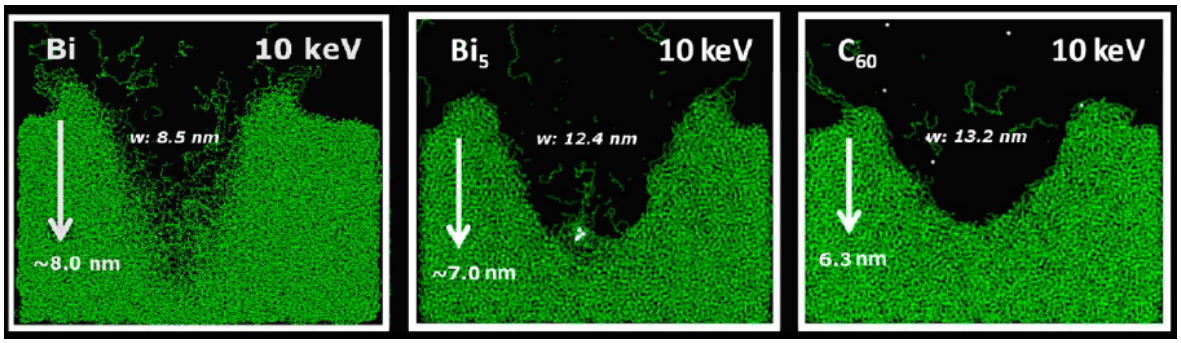

Figure 1.11: Modelling of 10 keV impacts of Bi^+, Bi_5^+, C_{60}^+ projectiles in a polymer sample [40]

Since only Bi_n^+ and Ar_n^+ clusters have been used during this master thesis, here are some details :

- **Bi_n^+ clusters** are formed through a liquid metal ion source or gun (LMIS or LMIG) instrument. It involves melting a metal into a liquid film of low volatility that flows through a solid needle. A sufficiently strong electric field is then applied to deform the liquid film into a conical protrusion. Finally, ions are generated by an electrospray which is itself produced by field evaporation at the sharp tip of the cone.[41] Compared to other LMIG, Bi source was found to be beneficial because it emits larger clusters ($1 \leq n \leq 7$) and produces higher currents of those clusters. [37]

- **Ar_n^+ clusters** are formed through a gas cluster ion beam (GCIB) instrument. GCIB consist of hundreds to thousands of individual gas atoms or molecules that are condensed into neutral clusters generated through cooling in a supersonic expansion. These clusters are then ionized by electron bombardment and finally typically accelerated to >10 keV kinetic energy. [37, 42]

1.1.4.4 The iBeam project

This master thesis was conducted in the framework of the iBeam project, promoted by A. Delcorte (IMCN/BSMA), Ch. Dupont (IMCN/BSMA) and C. Lauzin (IMCN/-NAPS).

The final purpose of this project is to develop a new instrument specially designed for a novel solvent-free method of surface (bio)functionalization by transferring material from a surface to another through the gas phase. The capabilities of ionic cluster beams to transfer neutral species and ions from a reservoir sample surface (the target) onto another (the collector) are thus investigated with a ToF-SIMS instrument.

1.1.4.5 Transfer

In 2016, Lorenz et al. showed that organic molecules could be transferred intact through the gas phase from a solid surface to another by using the Ar-GCIB of a ToF-SIMS instrument derived from its primary analytical function.[43] This study inspired Delmez et al. who succeeded to transfer under UHV intact and still bioactive lysozyme. After being transferred by large Ar cluster ion beams (Ar^{+}_{5000}), the proteins were analyzed by ToF-SIMS, identified by SDS-PAGE coupled to a mass spectrometer and their bioactivity was measured by enzymatic assays. An illustration of the experimental set-up is depicted in Figure 1.12. [44]

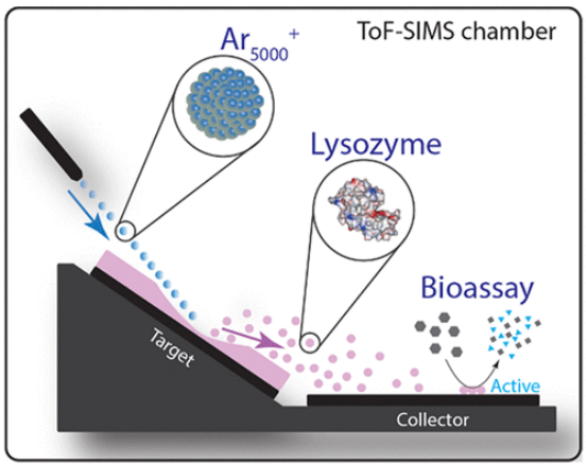

Figure 1.12: Schematic representation of lysozyme transfer from a target onto a collector using Ar cluster beams [44].

The results of the fluorescent-based enzymatic activity assay, performed directly on the collector, suggest that more or less 0.9 µg of lysozyme were deposited on the collector. If they were homogeneously deposited, the quantity of proteins would correspond to, at least, two to four molecular layers since a monolayer of lysozyme is approximately of about 0.115-0.230 µg/cm^2 and and the collector surface area roughly of 2

cm^2. This new technique of deposition thus allows to overcome the thickness limitation (monolayers) and drying issues inherent to direct adsorption from solution. Moreover, it permits to increase the deposition rates in comparison with other ion soft-landing techniques. [44]

However, even if some lysozyme molecules could be transferred without fragmentation, there are still a lot of covalent bond scissions upon impact because of the cluster size distribution. Indeed, the majority of argon cluster has a size of 5000 atoms (E/n = 2 eV/atom since they are accelerated at 10 keV) but higher E/n clusters induce more bond breaking. [44]

Knowing that proteins could be transferred without fragmentation encouraged us to move one step further. An interesting point to be studied is the feasibility to desorb non-covalent complexes from a surface and land them softly on another one by using large argon cluster and all this without breaking neither a covalent bond nor a non-covalent interaction.

1.1.5 Non-covalent interactions

Non-covalent interactions (NCI) are any relatively weak chemical bonds that do not involve an intimate electron sharing in opposition to covalent bonds, *i.e.* stable chemical forces that hold the atoms in molecules together by sharing one or more pairs of electrons. Indeed, they rather involve more dispersed variations of electromagnetic interactions between molecules or within a molecule. The multiplicity of non-covalent bonds often stabilizes the macromolecule conformation and allows specific interactions between molecules (see Figure 1.13). [45]

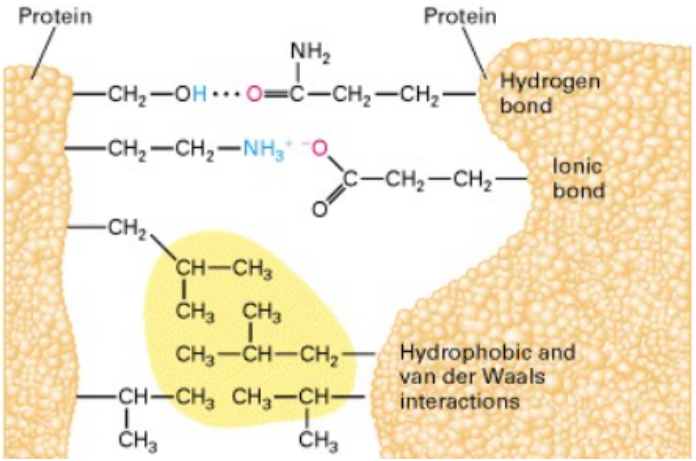

Figure 1.13: Representation of the structural surface complementarity of two hypothetical proteins giving rise to a particular combination of non-covalent interactions and hence to the specificity of binding. [45]

In this section, the different kind of NCI's will be briefly introduced. To be able to compare with the NCI's that will follow, Table 1.2 shows the energies of some of the covalent bonds found in biological molecules. [45]

Table 1.2: Energy required to break covalent bonds found in biological molecules (inspired from [45] and [46]).

Type of Bond	**Energy (kJ/mol)**	**Type of Bond**	**Energy (kJ/mol)**
SINGLE BOND		DOUBLE BOND	
O—H	464	C=O	741
H—H	436	C=N	615
P—O	350	C=C	611
C—H	415	P=O	503
C—O	350	TRIPLE BOND	
C—C	345	C≡ O	1080
C—N	290		

1.1.5.1 van der Waals interactions

van der Waals (vdW) interactions are weak nonspecific distance-dependent forces due to dipoles, *i.e.* small, transient asymmetric electron distributions around atoms. The vdW forces can be considered as resulting from three additive terms, the London forces, the Debye forces and the Keesom forces, as shown in Equation 1.4 and occur in all types of molecules, both polar and apolar [45, 47] :

$$F_{vdW} \approx F_{London} + F_{Debye} + F_{Keesom} \tag{1.4}$$

The Keesom forces induce orientation effects because of interactions between two permanent dipoles. The Debye forces occur when a permanent dipole induces a dipole moment in the electron cloud of a neighbouring species leading to an interaction. Finally, the London forces, which are present in every single interaction, occur between two induced dipoles. The typical potential energy of these van der Waals interactions range from 0.5 to 65 kJ/mol. [48, 55]

1.1.5.2 Hydrogen bonding

Hydrogen atoms have the ability to form an additional weak bond with an electronegative atom (the hydrogen bond acceptor), when they are covalently bound to another electronegative atom (the donor). The bond must therefore be polar and the acceptor must have at least one free electron pair for the hydrogen bond to form. This weak interaction is therefore often described as a mix between a dipole-dipole interaction (Keesom force) and a covalent bond. [45, 49] Their bonding energy is typically of the order of 4–50 kJ/mol but ranges from 1–2 kJ/mol (the weak non traditional ones) to 161.5 kJ/mol (the strongest one, *i.e.* FH···:F) [50]. Moreover, multiple (non)linear hydrogen bonds help to stabilize the three-dimensional structures of many large biomolecules such as proteins, base pairs in nucleic acids, cellulose, etc. [45]

1.1.5.3 Interactions involving π systems

Non-covalent forces that occur between a π system and another one, ions, metals and polar bonds form $\pi - \pi$, cation-π & anion-π, metal-π and polar-π interactions respectively. NCI's involving π systems are crucial to biological events such as protein-ligand recognition, drug design or catalysis. These interactions have a binding energy that can range from 1-2 kJ/mol to 50 kJ/mol or even more in function of the environment nature. [51, 52]

1.1.5.4 Ionic interactions

Ionic interactions are attractive electrostatic forces that occur between oppositely charged ions or between atoms with highly different electronegativities. In the second scenario, the difference in electronegativity between the atoms is such that the electrons that should be involved in a covalent bond are no longer shared. The less electronegative atom gives one or more electrons to the more electronegative one making them both ionic. This force can also be repulsive if the two ions have the same polarity. Coulomb's law (Equation 1.5) describes the potential energy (E) between two ions of charge q_1 and q_2 at a distance r from each other. This potential energy is inversely dependent to the dielectric constant of the medium(ε). [45, 51]

$$E = \frac{q_1 q_2}{4\pi\varepsilon r} \tag{1.5}$$

The bond energy can thus vary between 0 and 200kJ/mol in aqueous solutions or from 170 to 1500 kJ/mol in the solid state. [46, 53]

1.1.5.5 Metal-ligand coordination

Coordinate bonds are particular interactions that can be formed between transition metal centers (one or more metal atoms or ions) and ligands, *i.e.* neutral or ionic atoms or molecules. Over the years, tremendous work has been achieved in an attempt to formulate theories describing the binding in coordination compounds. A few of them are worth mentioning. According to the valence bond theory, these species act like Lewis acid and base respectively since the ligands donate electrons to the metal to form a dative bond. Crystal field theory considers metal ions as positive point charges and ligands as negative ones and thus presumes that the only interaction between the metal ion and the ligands is an electrostatic or ionic interaction. In molecular orbital theory, *i.e.* a method used to describe the electronic structure of molecules relying on quantum mechanics, approximated by the linear combination of atomic orbitals method, orbitals overlapping and electrons sharing have to be considered. Although the two first theories are now outdated, they still serve as a backdrop for the evaluation of new models as they have shaped thinking about coordination compounds in the recent past. [55]

When a ligand, often an organic compound, has more than one atom involved in coordination interactions with the same metal centre, it is called chelation. This chelate effect offers additional stability mainly due to an entropic effect. Denticity then refers to the number of donor atoms in a single ligand that bind to the central metallic atom. The coordination number of the central atom is the number of atoms, molecules or ions that can bond to it. The values of coordination binding energies can vary between ~200 and 650 kJ/mol. [54, 55]

1.1.5.6 Hydrophobic effect

Molecules that do not contain any charged moiety or dipole moment, *i.e.* non-polar molecules, and that cannot become hydrated and dissolve (or nearly so) in water are called hydrophobic molecules. The hydrophobic effect is the tendency of such molecules or non-polar parts of molecules to aggregate to minimize contact with their aqueous environment. In fact, it is equivalent to the energy needed to introduce a non-polar molecule into the water. According to Hermann (1972), the hydrophobic effect depends on the number of water molecules surrounding a non-polar solute, which is proportional to its solvent accessible surface. Since hydrophobic compounds cannot form hydrogen bonds with H_2O molecules, they force the water molecules to take a different conformation which is a cage of H-bonded water molecules surrounding the compound. This is called the iceberg model. [45, 56, 57]

Depending on the method used to calculate hydrocarbon surface areas, the binding energy of the hydrophobic effect for such molecules varies from 84 to 120 J/molÅ^2 [56]. Others claimed that it can ranges between 63 and 314 J/molÅ^2 [51].

1.1.5.7 Summary of binding energies

Hereunder, Table 1.3 gives a summary of the binding energies of the different non-covalent interaction types.

Table 1.3: Relative strength of molecular forces

Interaction	**Binding energy (kJ/mol)**
Covalent	100-1000
van der Waals	0.5-65
Hydrogen bond	4-50
Involving π systems	2-50
Ionic	170-1500
Metal-ligand coordination	200-650
Hydrophobic effect	63-314 J/molÅ^2

This is an approximate comparison. The exact values of the binding energy will differ depending on the molecules and atoms involved, as well as with their environment.

1.1.6 Non-covalent complexes

As previously mentioned, the possibility to desorb and soft-land non-covalent systems was investigated using a time-of-flight secondary ion mass spectrometer. In this section, the two non-covalent systems that were studied throughout the year are presented.

1.1.6.1 Vancomycin

Vancomycin (molecular formula $C_{66}H_{75}Cl_2N_9O_{24}$, further denoted as V) is an antibiotic glycopeptide, and is, alongside the β-lactams, an inhibitor of the cell-wall peptidoglycan synthesis in Gram-positive bacteria. This drug is particularly of clinical importance since it is the last resort against methicillin-resistant *Staphylococcus aureus*.

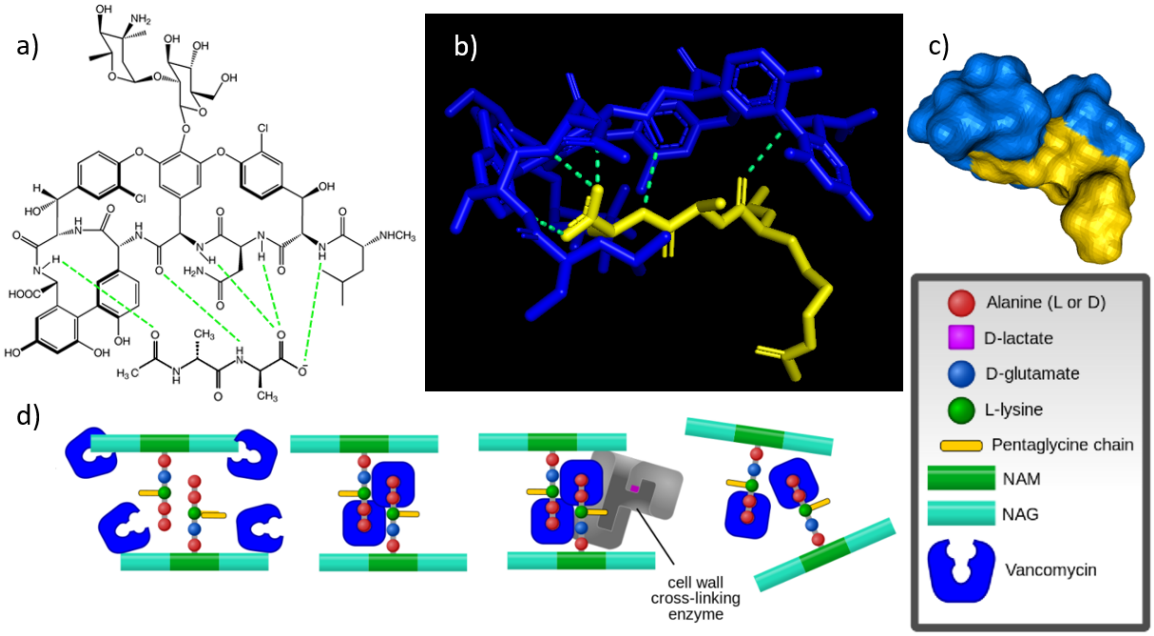

Figure 1.14: (a) Chemical structure of vancomycin 5 times H-bonded with an acetylated-AA. (b) 3D structural representation of V+KAA complex, the vancomycin being in blue, KAA in yellow and H-bonds in green (done by using Pymol program). (c) 3D Surface representation of V+KAA complex [59]. (d) Schematic representation of the vancomycin action mechanism [60].

Thanks to the research of many scientists, it is now well established that the vancomycin activity is foremost a direct result of non-covalent interactions, *i.e.* five hydrogen bonds, electrostatic and hydrophobic interactions. These interactions allow to bond the antibiotic molecule and the peptidoglycan precursor UDP-N-acetylmuramylpentapeptide. Actually, the H-bonds are situated between the vancomycin and the terminal dipeptide of this precursor, the D-Alanyl-D-Alanine moiety (Figure 1.14a-b-c). Vancomycin and this precursor form thus a stable non-covalent complex that inhibits the transpeptidation, *i.e.* the crosslinking of the cell-wall peptidoglycan monomers, resulting in the

bacterial death (Figure 1.14d). In most experimental study, D-Ala-D-Ala (AA) and L-Lysine-D-Ala-D-Ala (KAA) peptides were used to mimic the precursor. [58]

This system has become a model for the study of the receptor-ligand recognition processes and proved to be an ideal model system for exploring non-covalent interactions using MS techniques. ESI-MS, which is a quite soft method, allowed for this particular example, the analysis of the intact complex without breaking weak non-covalent interactions through the ionization process. An ESI-MS spectrum of this system is shown in Figure 1.15. The measurements accomplished in the study of T.J.D. Jørgensen et al. proved that vancomycin-ligand system could be analyzed intact via ESI-MS and allowed the direct determination of the solution association constants between vancomycin and 3 different ligands. The arithmetical mean of these constants used further are $K_{A,[V+AA]} \approx 1.6667 * 10^4$ and $K_{A,[V+KAA]} \approx 8.1333 * 10^5$. [58, 61, 62]

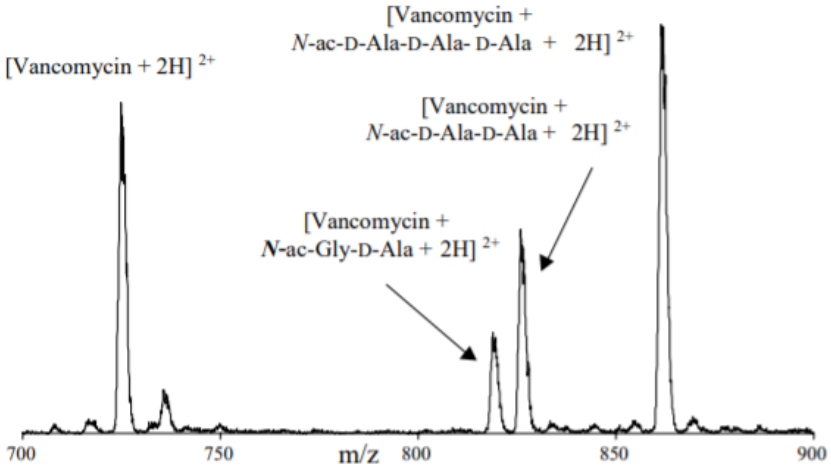

Figure 1.15: ESI-MS spectrum of an equimolar (50 µM) mixture of vancomycin with the three peptides Ac-Gly-D-Ala, Ac-D-Ala-D-Ala and Ac-D-Ala-D-Ala-D-Ala [61].

Moreover, it has been suggested that formation of dimers may affect the efficacy of glycopeptide antibiotics. Indeed, dimers of vancomycin, which are also non-covalent complexes as they are linked through H-bonds, could enhance the antibacterial activity by cooperating with ligand binding. The dimer conformation thus allows the binding to two peptidoglycan precursors in opposite direction at the same time as depicted in Figure 1.16. [58, 63]

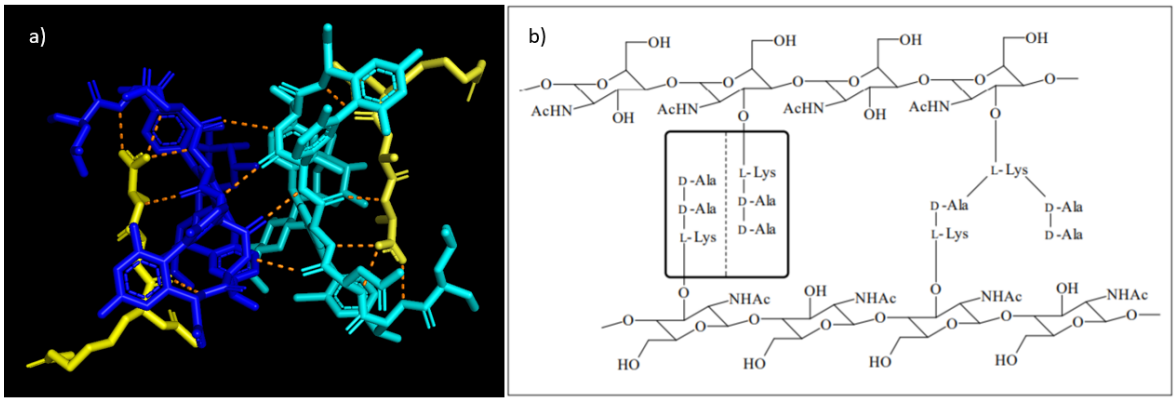

Figure 1.16: a) 3D structural representation of the vancomycin dimer complex doubly bonded to KAA, the vancomycin molecules being in blue, KAAs in yellow and the H-bonds in orange (Pymol program). b) Schematic insertion of the vancomycin dimer (the two halves of the box represent the two monomers) between two peptidoglycan chains, preventing the crosslinking between them as shown on the right of the figure [63].

Finally, in 2018, Du et al. investigated surface chemistry and chemical structures of controlled-release drug delivery systems using ToF-SIMS. They succeeded to identify characteristic fragments of the vancomycin molecule in both positive and negative modes, the pseudomolecular ion $[V+H]^+$ in positive mode and the decarboxylated molecular ions $[V\text{-}COOH]^-$ in the negative mode. Spectra of the latter are shown in Figure 1.17 but details will be given in the "results and discussion" section. [64]

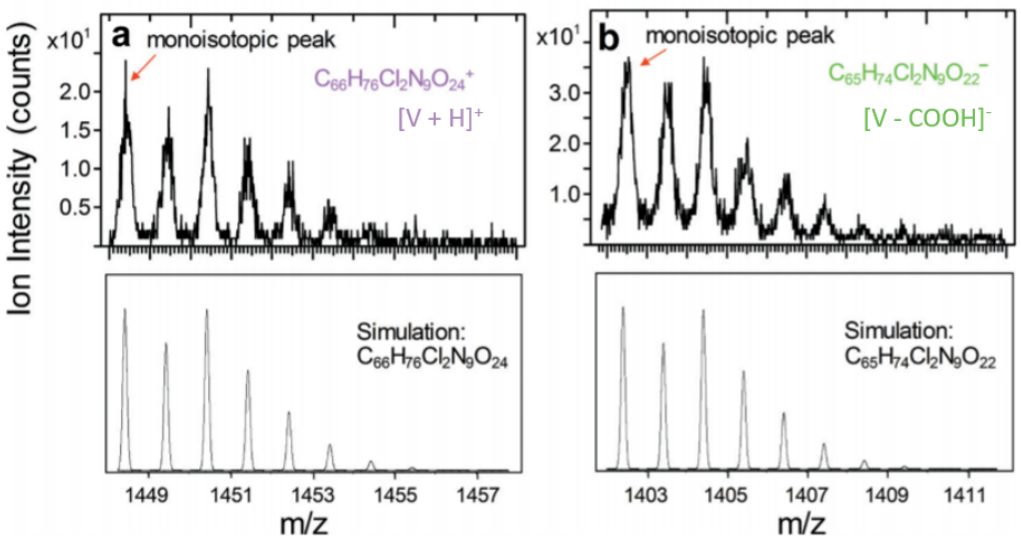

Figure 1.17: (Upper cases) Positive (a) and negative (b) SIMS spectra showing the isotopic distribution of the pseudomolecular ions $[V+H]^+$ and decarboxylated ions $[V\text{-}COOH]^-$ of vancomycin respectively. (Lower cases) Simulation of the isotopic distribution of these uncharged molecules. [64]

Driven by these reported experimental results, we found relevant to select these V+(K)AA model systems and vancomycin dimers as candidates in our quest towards the transfer of weakly bound non-covalent complexes using a ToF-SIMS instrument.

1.1.6.2 M(tfac)$_n$

Ligands derived from pentanedione (commonly known as acetylacetone) can form particularly stable complexes, thanks to the "chelate" effect. Indeed, these bidentate ligands can bind to the metal center via two oxygen atoms to form chelates. The different metal complexes used during this master thesis were composed of chromium, nickel, copper or cobalt and two or three trifluoroacetylacetone (1,1,1 trifluoro-2,4-pentanedione, molecular formula $C_5H_5O_2F_3$, denoted as "tfac") ligands based on the metal charge. Each ligand must get rid of one proton from its central carbon atom in order to be negatively charged and readily react with metallic cations to form ML_3 or ML_2 complexes. A synthetic pathway of these complexes is shown in Figure 1.18. [65]

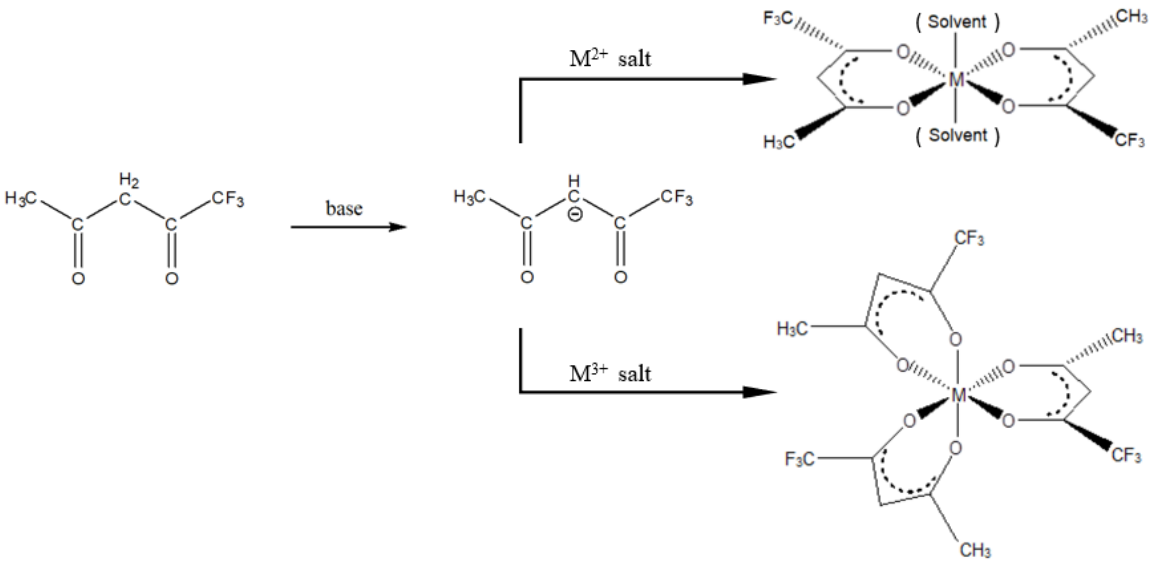

Figure 1.18: Synthesis pathway of M(tfac)$_x$ complexes, x being 2 or 3. M^{3+} metals form complexes with three ligands and M^{2+} metals with two ligands. In some cases the M^{2+} complexes contain solvent molecules coordinated to the metals (indicated with parentheses). Inspired from [65].

Because of their great stability and neutrality (*i.e.* uncharged), some of these octahedral complexes are stable in the gas phase and even under vacuum. This uncommon property of transition metal complexes allows their characterization by MS techniques such as gas chromatography. Since these transition metals usually have many isotopes and that their molecular isotopic distribution can easily be identified on mass spectra, these complexes are generally very recognizable when analyzed by mass spectrometry. For example, copper has two stable isotopes, ^{63}Cu and ^{65}Cu, with a relative abundance of 69.17% and 30.83% respectively. Spectra of molecules containing copper will thus

show molecular ions containing ^{63}Cu and ^{65}Cu and the amounts of these ions will reflect the natural abundance of each isotope. [65]

As this second system is stable in the gas phase and the metal isotopes can be easily recognised by mass spectrometry, we found it interesting to investigate their desorption and soft-landing by ToF-SIMS in order to complement the previous study on V+(K)AA complexes.

1.2 Objective and methodology

As a reminder, the iBeam project investigates the engineering of cluster ion beams, their characterization and utilization to control the ionization and transfer of complex (bio)molecules for the design of new surface architectures and for the enhancement of SIMS sensitivity. Even if intact and still active proteins could already be transferred from a target to a collector, their fragmentation remains more than significant.

In order to improve the knowledge on the desorption and transfer possibilities via large cluster ion beams, this master thesis aims to investigate non-covalent complexes using time-of-flight secondary mass spectrometry, for both surface analysis and soft-landing experiments. The goals of this study are on the one hand to find optimized conditions that best allow the analysis of non-covalently bound compounds, *i.e.* vancomycin-(L-Lysine-)D-Alanine-D-Alanine systems and metal trifluoroacetylacetonate coordination complexes. For that, various parameters can be tuned: primary ion nature, cluster size and energy, sample thickness and substrate's hardness are among the most impactful ones. On the other hand, once the most suitable conditions have been determined, the transfer of these non-covalent complexes will be attempted. Here, the ultimate goal is to achieve the transfer of intact complexes from one surface onto another. The complexes will therefore have to remain intact during all steps (desorption, travel in vacuum, and impact upon landing) in the SIMS instrument. Thus, we hope to demonstrate that sufficiently soft desorption conditions can be achieved in SIMS to emit non-covalent complexes without breaking weak interactions, in addition to covalent bonds.

The methodology to do so is as follows :

- Firstly, the molecules composing the non-covalent complexes must be analyzed individually to obtain reference fragmentation patterns.
- Secondly, complexes will be analyzed by different cluster ion beams, 30 keV Bi_5^+ and 10 keV Ar_{1500}^+, Ar_{3000}^+ and Ar_{5000}^+, to be compared with references and with each other. In addition to the ion beams and their kinetic energies, different parameters will be investigated. For the vancomycin systems, the prepared concentrations will range from 0.1 to 50 g/L and will provide different sample thicknesses, measured by ellipsometry, in order to study thickness effects on sputtering. The ratio between vancomycin and the ligands will be varied from 1:1 to 1:10 to drive the reaction towards the formation of complexes and thus try to enhance their ion yields. As solvent for these solutions, ultra pure water, methanol (30% in volume) and ammonium acetate buffer will be tested. Finally, hard silicon and soft polyethylene terephthalate (PET) substrate will be used in order to study the effect of substrate hardness. For the metal-ligand complexes, since their in-

vestigation started late in the year, much less parameters will be varied. Only the clusters nature, size and energy and the substrates hardness will be varied.

- Finally, once it has been demonstrated, if possible, that these non-covalent complexes can be desorbed intact and analyzed, their transfer on another substrate will be studied. Once again, different cluster ion beams: 30 keV Ar^+_{3000} and Ar^+_{5000}, and different collecting substrates will be used. Then, these collecting surfaces will be analyzed to ensure that these non-covalent complexes were transferred intact.

2 Materials and methods

2.1 Sample preparation

2.1.1 Chemicals

2.1.1.1 Vancomycin-ligand system

- **Vancomycin**: Vancomycin hydrochloride purchased from *Sigma-Aldrich*.
  CAS Number : 1404-93-9
  Empirical formula : $C_{66}H_{75}Cl_2N_9O_{24}.xHCl$
  Molecular mass : 1449.25 Da

- **D-Alanine-D-Alanine**: D-Ala-D-Ala purchased from *Sigma-Aldrich*.
  CAS Number : 923-16-0
  Empirical formula : $C_6H_{12}N_2O_3$
  Molecular mass : 160.17 Da

- **Acetyl-Lysine-D-Alanine-D-Alanine**: Acetyl-Lys-D-Ala-D-Ala purchased from *Sigma-Aldrich*.
  CAS Number : 28845-97-8
  Empirical formula : $C_{14}H_{26}N_4O_5$
  Molecular mass : 330.38 Da

2.1.1.2 M(tfac)$_n$ complexes

Chromium, cobalt, copper and nickel trifluoroacetylacetonates (tfac) were all kindly provided by Pr. Sophie Hermans (SST/IMCN/MOST). They were synthesized by master students during practical works. Molecular masses are given in Table 2.1.

Table 2.1: Molecular masses of the complexes

Complex	**Molecular mass (Da)**
$Ni(tfac)_2$	364.85
$Co(tfac)_2$	365.09
$Cu(tfac)_2$	369.70
$Cr(tfac)_3$	511.23

2.1.2 Solution preparation

2.1.2.1 Vancomycin-ligand system

First, stock solutions (2 mmol/L) were prepared by dissolving approximately 72.46, 8.01 and 6.61 mg of vancomycin, AA and KAA respectively in 25 (for the 2 firsts) and 10 mL volumetric flasks filled with ultra pure water. Volumes were then transferred into 1 and 2 mL aliquots. Two more vancomycin stock solutions (5 and 50 g/L) were prepared by dissolving 10 and 250 mg into 2 and 5 mL of ultra pure water respectively.

An ammonium acetate (NH_4Ac) buffer was prepared by dissolving approximately 77.02 mg into 180 mL of ultra water in a 200 mL volumetric flask. Then 2-3 drops of concentrated HCl were added to adjust the pH to 5.1 and ultra pure water until the volumetric flask line was reached.

The diluted sample solutions for the reference analyses were then prepared according to Table 2.2 :

Table 2.2: References samples method of dilution

Sample	Volumes to be withdrawn [mL]							Final volume [mL]	Final concentration
	Stock solutions (2mM)			Stock solution of V (50g/L)	Stock solution of V (5g/L)	Solution from previous row	Pure water		
	V	AA	KAA						
Vancomycin	/	/	/	4	/	/	1	5	40 g/L
	/	/	/	/	/	3.75	1.25	5	30 g/L
	/	/	/	/	/	3.33	1.67	5	20 g/L
	/	/	/	/	/	3.75	1.25	5	15 g/L
	/	/	/	/	/	3.33	1.67	5	10 g/L
	/	/	/	/	/	2.5	2.5	5	5 g/L
	/	/	/	/	1.2	/	0.8	2	3 g/L
	/	/	/	/	/	0.67	1.33	2	1 g/L
	/	/	/	/	/	1	1	2	0.5 g/L
	/	/	/	/	/	0.4	1.6	2	0.1 g/L
	0.05	/	/	/	/	/	1.45	1.5	66.67 µmol/L
AA	/	0.05	/	/	/	/	1.45	1.5	66.67 µmol/L
KAA	/	/	0.05	/	/	/	1.45	1.5	66.67 µmol/L

The diluted sample solutions for the complexes analyses were then prepared according to Table 2.3 :

Table 2.3: Complexes samples method of dilution

Sample	Ratio	Volumes to be withdrawn [µL]						Final volume [mL]	V:Ligand initial concentration (mM)	Complex theoretical concentration (mM)
		Stock solutions (2mM)			NH_4Ac Buffer	Pure MeOH	Pure water			
		V	AA	KAA						
V+AA	1:1	50	50	/	/	/	1400	1500	0.0667:0.0667	0.0267
		50	50	/	1400	/	/	1500	0.0667:0.0667	0.0267
		100	100	/	/	/	/	200	1:1	0.783
		150	150	/	/	/	/	300	1:1	0.783
	1:2	66.67	133.33	/	/	/	/	200	0.667:1.333	0.616
		100	200	/	/	/	/	300	0.667:1.333	0.616
V+KAA	1:1	50	/	50	/	/	1400	1500	0.0667:0.0667	0.0582
		50	/	50	1400	/	/	1500	0.0667:0.0667	0.0582
		100	/	100	/	/	/	200	1:1	0.9655
		150	/	150	/	/	/	300	1:1	0.9655
		7.5	/	7.5	/	45	90	150	0.1:0.1	0.0895
	1:2	66.67	/	133.33	/	/	/	200	0.667:1.333	0,6658
		100	/	200	/	/	/	300	0.667:1.333	0,6658
		7.5	/	15	/	45	82.5	150	0.1:0.2	0.0988
	1:5	7.5	/	37.5	/	45	60	150	0.1:0.5	0,0997
	1:8	7.5	/	60	/	45	37.5	150	0.1:0.8	0.0998
	1:10	7.5	/	75	/	45	22.5	150	0.1:1	0.0999

In Table 2.3, the [V+AA] complex theoretical concentrations were calculated, via

the mean of the association constants found in [58], simply by resolving the second degree equation (Eq. 2.1) related to the complexation reaction visible in Table 2.4.

Table 2.4: Association reaction between V and AA and concentrations at play

	V	+	AA	⟶	[V+AA]
C_i	$C_{V,i}$		$C_{AA,i}$		0
C_f	$C_{V,i} - x$		$C_{AA,i} - x$		x

$$K_a \approx 16667 = \frac{x}{(C_{V,i} - x)(C_{AA,i} - x)} \tag{2.1}$$

The same reasoning was applied to find the equilibrium concentrations of the [V+KAA] complex (with $K_a \approx 813333$).

2.1.2.2 M(tfac)$_n$ complexes

Solutions of ∼20 g/L were prepared in 200 µL eppendorfs by dissolving approximately 4 mg of each complex into dichloromethane (CH_2Cl_2).

2.1.3 Surface cleaning

Before depositing the sample on the substrates, the latter must be thoroughly cleaned to avoid contamination as much as possible.

2.1.3.1 Silicon wafers

- **Piranha mixture**
  The wafers, originating from Neyco (WAK2PN model, Vanves, France), were immersed 15 minutes in a 3:1 (v:v) solution of concentrated sulfuric acid and 30% hydrogen peroxide. When mixed together, these solutions produce, among other compounds, extremely reactive atomic oxygen species that can dissolve carbon compounds and transform them into CO_2. [66] They were then rinsed 10 times with MilliQ water and dried under N_2.

- **UV/Ozone treatment**
  After that, they were exposed 15 minutes to UV-ozone in a UVOcleaner Model 42 Series (Jelight Company Inc., California, USA). UV-ozone treatment allows the removal of the last organic traces by these reactions [67] :

$$O_2 \xrightarrow{UV(185nm)} 2\,O(3\,P)$$

$$O_2 + O(3\,P) \longrightarrow O_3$$

$$O_3 \xrightarrow{UV(254nm)} O_2 + O(1\,D)$$

$$O(1\,D) + \text{Organic compounds} \longrightarrow CO_2 + H_2O + O_2 + N_2 + ...$$

2.1.3.2 PET wafers

Polyethylene terephthalate (PET) substrates, originating from Goodfellow (ES303010 model, Huntington, England), were immersed in pure ethanol and placed for 15 minutes in a sonicator (Branson IC® Ultrasonic cleaner, model 2510E-MT, Danbury, USA). They were then rinsed with fresh ethanol and dried under N_2.

2.1.4 Deposition of solutions

2.1.4.1 Spin-coating

Some of the non-covalent complex solutions (150µL) were spin-coated 60 seconds at 3000 rpm using a model WS-400B6NPP/LITE (Laurell technologies corporation, Pennsylvania, USA). This technique allows the deposition of thickness-controlled and homogeneous thin films of solid materials on small surface areas [68].

2.1.4.2 Drop-casting

When a thicker film of material was needed, e.g. for transfer, drying droplets onto the wafers was used. It consists in letting a few drops of the solution dry directly on the wafers one after the other. For aqueous vancomycin-ligand solutions, three 15 µL droplets were dried, each during 3 hours. For $M(tfac)_x$ solutions, about twenty 10 µL droplets were dried, each during 30 seconds as dichloromethane evaporates very quickly.

2.2 ESI analyses

ESI-MS analyses using a Q-Exactive spectrometer (ThermoFisher Scientific) were performed with Raoul Rozenberg (IMCN) to validate the presence of vancomycin-ligand complexes and contamination in some solutions. The analyzed solutions were prepared following Table 2.5 :

Table 2.5: ESI samples method of dilution

Sample	Ratio	Volumes to be withdrawn [µL]							Final Volume [µL]	Initial concentration (mM)	Complex theoretical concentration (mM)
		Stock solutions (2mM)			Complex solutions (66.67µM)		Pure MeOH	Pure water			
		V	AA	KAA	V+AA	V+KAA					
V+AA	1:1	/	/	/	200	/	450	850	1500	0.0089:0.0089	0.00103
V+KAA	1:1	/	/	/	/	180	450	870	1500	0.008:0.008	0.00542
		7.5	/	7.5	/	/	45	90	150	0.1:0.1	0.0895
	1:2	7.5	/	15	/	/	45	82.5	150	0.1:0.2	0.0988
	1:5	7.5	/	37.5	/	/	45	60	150	0.1:0.5	0.0997
	1:8	7.5	/	60	/	/	45	37.5	150	0.1:0.8	0.0998
	1:10	7.5	/	75	/	/	45	22.5	150	0.1:1	0.0999
V	/	37.5	/	/	/	/	45	67.5	150	0.5	/
KAA	/	/	/	37.5	/	/	45	67.5	150	0.5	/

The instrument was used with a scan type in full MS and a scan range between 300 and 1700 m/z in positive mode. The resolution was of 140000. The spray voltage was of 3.5 kV and the capillary temperature of 300°C.

2.3 Ellipsometry

A spectroscopic ellipsometer (Accurion GmbH, Goettingen, Germany) was used with an n-k-fix model and a refraction index of 1.5 to measure the deposited thickness of vancomycin references (0,1 to 20 g/L). The thickness of vancomycin was approximated by a silicon oxide layer.

2.4 ToF-SIMS

A ToF-SIMS V instrument (IONTOF GmbH, Münster, Germany) was used for surface analysis and transfer experiments. The software used to control the ToF-SIMS instrument and for data processing is the IONTOF SurfaceLab software.

2.4.1 Analyses

Before analyzing, 1 cm x 1cm wafers are mounted on an IONTOF backmount sample holder (Figure 2.1) which is then inserted into the instrument main chamber. Before (and after) measurement, the ion beam current is measured.

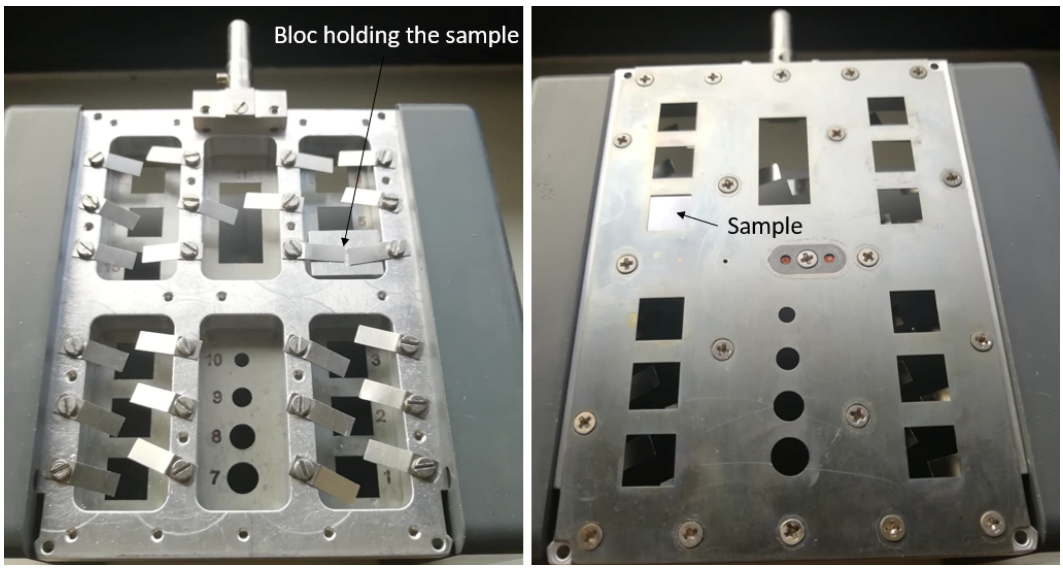

Figure 2.1: (Left) Mounting and (right) analysis sides of the backmount sample holder.

The cluster ion beams used to analyze samples were :

- 30 keV Bi_5^+ cluster ion beam in high current bunched mode, with a current of ±0.045 or ±0.09 pA corresponding to cycle times of 200 and 100 µs respectively. Both polarities of the secondary ions were analyzed for almost all samples. The analysis times were set on 1 minute. The ion dose density was approximately between 5 and 7×10^9 ions/cm^2.

- 10 keV Ar_{1500}^{+} cluster ion beam. The ion current was too low to be measured and the ion dose density was thus impossible to calculate.
- 10 and 20 keV Ar_{3000}^{+} cluster ion beams. The analysis times were set on 5 minutes. The ion current was measured between 0.01 and 0.06 pA. The analysis times were set on 5 minutes. The ion dose density was approximately between 10^{10} and 10^{11} ions/cm^2.
- 10 keV Ar_{5000}^{+} cluster ion beams. The measured ion current was about 0.007 pA. The analysis times were set on 5 minutes. The ion dose density was approximately of 10^{10} ions/cm^2.

For PET substrates, which are insulators, a charge compensation with an electron floodgun of 20 eV was used. At least three acquisitions, with a raster size of 500 µm x 500 µm, were made per sample. During acquisition, the spectrum peaks are shifted and thus need to be calibrated. To do so, a mass calibration was applied using most of the time CH_3^+, $C_2H_5^+$, $C_3H_5^+$ and $C_4H_7^+$ peaks in positive mode and CH^-, C_2H^-, C_3H^- and C_4H^- peaks in negative mode. These non-specific ions have a high probability of formation and originate from collisions between the primary ions and larger surface molecules from the sample or ubiquitous carbonated contamination [31].

2.4.2 Transfer

After the droplets were dried on 1 cm x 0.3 cm silicon targets, the latter are glued with conductive adhesive paper on the IONTOF topmount sample holder topped with a block designed for transfer. The cleaned silicon or PET collectors were taped just below the target as it can be seen in Figure 2.2.

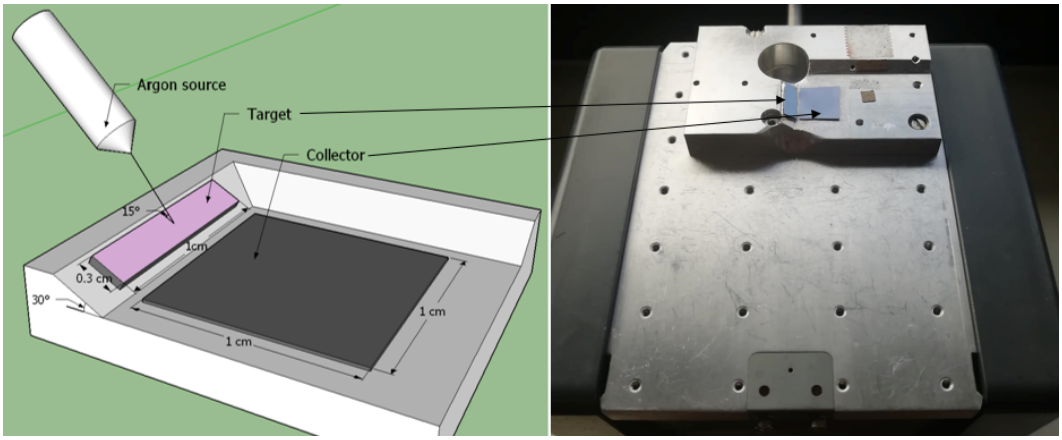

Figure 2.2: (Left from [44]) 3D representation and (right) picture of the topmount sample holder used for transfer experiments

Once inserted into the spectrometer and all pre-settings completed (see section 2.4.1), transfer can begin. The two cluster ion beams used for transfer were :

- 10 keV Ar_{5000}^+ beam with a sputtering current of 1.3-1.4 nA. With this beam, the bombardment was usually overnight (12-15 hours) and the total doses obtained were between 4 and 5×10^{14} ions.
- 10 keV Ar_{3000}^+ beam with a sputtering current of 7.2-8 nA. With this beam, the bombardment usually lasted 2-3 hours and the total doses obtained were between 3.5 and 6×10^{14} ions.

2.4.3 Collectors 2D mapping

Once transfers were finished, the collectors were placed in the backmount sample holder and all the pre-settings were done as in section 2.4.1. Images of positive and negative secondary ions from these samples were obtained by using the stage scan raster mode and the 30 keV Bi_5^+ cluster ion beam. The total images are obtained by merging individual images of small surface areas of 500 µm x 500 µm and with a pixel density of 256x256 (about 1.95 µm between two pixels).

2.4.4 Data processing

The IONTOF software was used to analyze the obtained spectra and to integrate the areas of the peaks of interest. These areas, given in secondary ion counts, were then copied into an Excel sheet to be processed.

At first, they were normalized by the dose density, *i.e.* the number of primary particle impacts per square centimeter [$1/cm^2$], in order to compare results from different experiments. This operation therefore allowed to work with the yield of secondary ions per primary ions and per square centimeter. These yields were then compared between each other and tendencies were shown in histograms.

Later, since the analysis current was often too low to be measured (Ar analysis beams), the software could not calculate dose intensities. The areas of the peaks were then normalized by the total number of counts of their respective spectrum. The results were then processed in the same way, described above.

Tables (shown in Figures 6.1 and 6.2) show in Appendix the summaries of the different SIMS and ESI analyses done during the whole year.

3 Results and discussion

The idea was to start the experiments with the vancomycin-ligand model system firstly because it was already studied by others and especially in mass spectrometry. Secondly to investigate whether weakly bound systems could be (i) desorbed from a surface and (ii) landed on another one intact. This was quite ambitious as SIMS is generally known to break covalent bonds and because this non-covalent system is bound by much weaker interactions which are hydrogen bonds. Many different conditions were explored and their results are presented and discussed in this section.

3.1 Vancomycin-ligand system

3.1.1 References

To be able to compare future mass spectra of the complexes, analyses of samples containing only one of the constituents were carried out using a 30 keV Bi_5^+ primary beam in both polarities. In order not to overload the results section with figures, only the positive spectra will be shown. The negative spectra are shown in Appendix (section 6.2).

3.1.1.1 Vancomycin

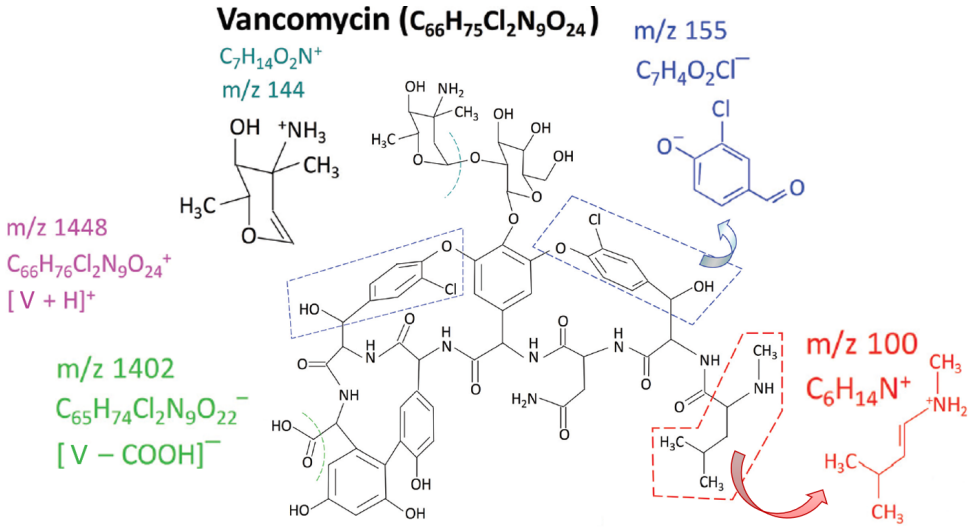

Figure 3.1: Positive and negative characteristic fragments of vancomycin when analyzed by ToF-SIMS [64].

Figure 3.1 shows the vancomycin structure and its positive and negative characteristic ions. The obtained vancomycin reference mass spectra, in adequacy with [64], show peaks of the characteristic fragments and pseudomolecular ions. Figure 3.2 shows the mass spectra of these positive ions while Figure 6.3 shows the negative ones. The peaks shown in Figure 3.2a-b correspond to well defined fragments of vancomycin, *i.e.* $C_6H_{14}N^+$ at m/z 100 and $C_7H_{14}O_2N^+$ (a part of the vancosamine end group) at m/z 144. The leftmost group of peaks in Figure 3.2c correspond to its pseudomolecular ion $[V+H]^+$ (monoisotopic peak at m/z 1448.4) respectively. Another abundant peak at m/z 1305 (Figure 6.4) corresponds to the loss of the fragment at m/z 144. Other groups of peaks could be attributed to large vancomycin fragments (Figure 6.4a-b) but hypothetically. In the negative mass spectra, the $C_7H_4O_2Cl^-$ fragments show the characteristic isotopic distribution of chlorine. Indeed, the peak at m/z 155 correspond to $C_7H_4O_2{}^{35}Cl^-$ while the peak at m/z 157 to $C_7H_4O_2{}^{37}Cl^-$ (Figure 6.3a). The deprotonated vancomycin ion $[V-H]^-$ could not be detected in negative mode but the decarboxylated one could and is visible in Figure 6.3b ($[V-COOH]^-$, monoisotopic peak at 1402.4). This has already be shown by Du et al. [64], but some other interesting peaks could be attributed :

1. The rightmost peak group in Figure 3.2c correspond to $[V+Na]^+$ ions. Indeed, there is a mass difference of 22 Da between the distribution of $[V+H]^+$ (monoisotopic peak at m/z 1448.4) and the one of $[V+Na]^+$ (monoisotopic peak at m/z 1470.4) corresponding to the replacement of the hydrogen atom by a sodium atom. This is more than likely due to sodium contamination, inherent to this type of sample. $[V+H]^+$ and $[V+Na]^+$ peaks, now referred to as the pseudomolecular ions peaks, have often been summed in order to normalize the intensities of fragment and dimer peaks to those ones.

2. In figure 6.3b, two other isotopic distributions at m/z 1384 and 1546 could correspond to a loss of H_2O and to an addition of the vancosamine end group (144 Da) but this was not verified.

3. Moreover, the vancomycin dimers (shown in Figures 3.2d and 6.3d) could be observed in both the negative and positive modes. These peaks groups are rather difficult to interpret, as the peaks intensity and resolution are very low. This can be explained by the low sputtering yield of these dimerized ions as well as the reduced detection efficiency at high mass. Figure 6.5 shows a better view of the dimer isotopic distribution.

4. Finally, a barely visible group of peaks mostly in the negative mode (not shown) at m/z 2850 could correspond to a decarboxylated dimer and another at 2805 to a doubly decarboxylated one. The intensities and resolutions being even lower, these attribution cannot be assured.

The detection of these dimers is a first success for the desorption part of this master thesis since they are composed of two vancomycin molecules linked by 4 hydrogen bonds and thus represent non-covalent complexes. This already means that small Bi_5^+ clusters, having an energy per atom (E/n) of 6 keV/atom, can desorb intact weakly bound non-covalent complexes whose internal energy is small enough to avoid dissociation over the tens of microseconds needed to reach the detector.

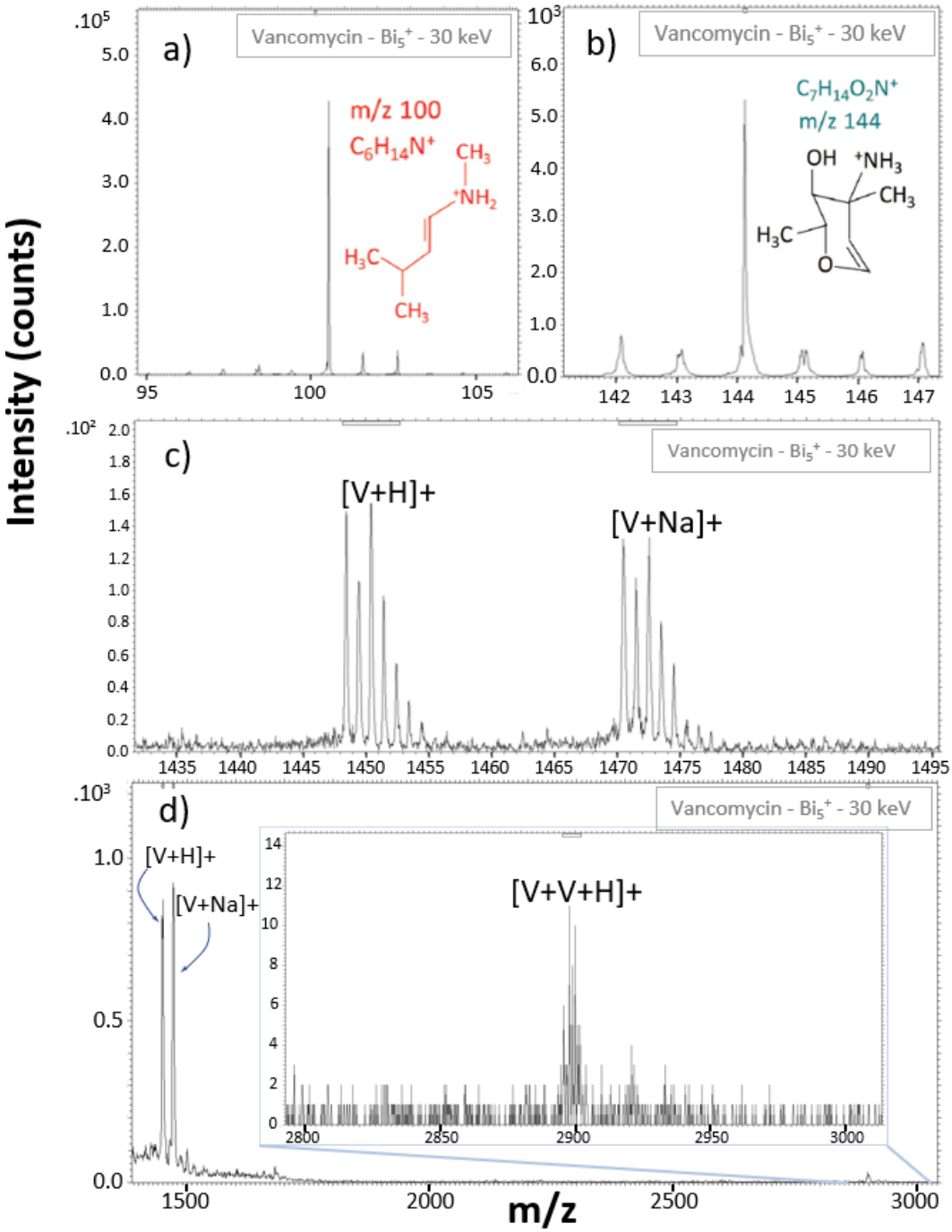

Figure 3.2: Spectra of vancomycin diagnostic ions (a) $C_6H_{14}N^+$ at m/z 101.1, (b) $C_7H_{14}O_2N^+$ at m/z 144.1, (c) pseudomolecular ion ($C_{66}H_{76}Cl_2N_9O_{24} \equiv [V+H]^+$, monoisotopic peak at m/z 1448.4) and Na^+-associated molecular ion ($[V+Na]^+$, monoisotopic peak at m/z 1470.4) and (d) vancomycin dimer ($[V+V+H]^+$, monoisotopic peak at m/z 2895.9).

3.1.1.2 Ligands

Figures 3.3a-b shows the chemical structures of D-Ala-D-Ala and acetyl-L-Lys-D-Ala-D-Ala. These two molecules have a mass of 160.17 and 330.38 Da respectively and their partial positive mass spectra are shown in Figure 3.3c-d.

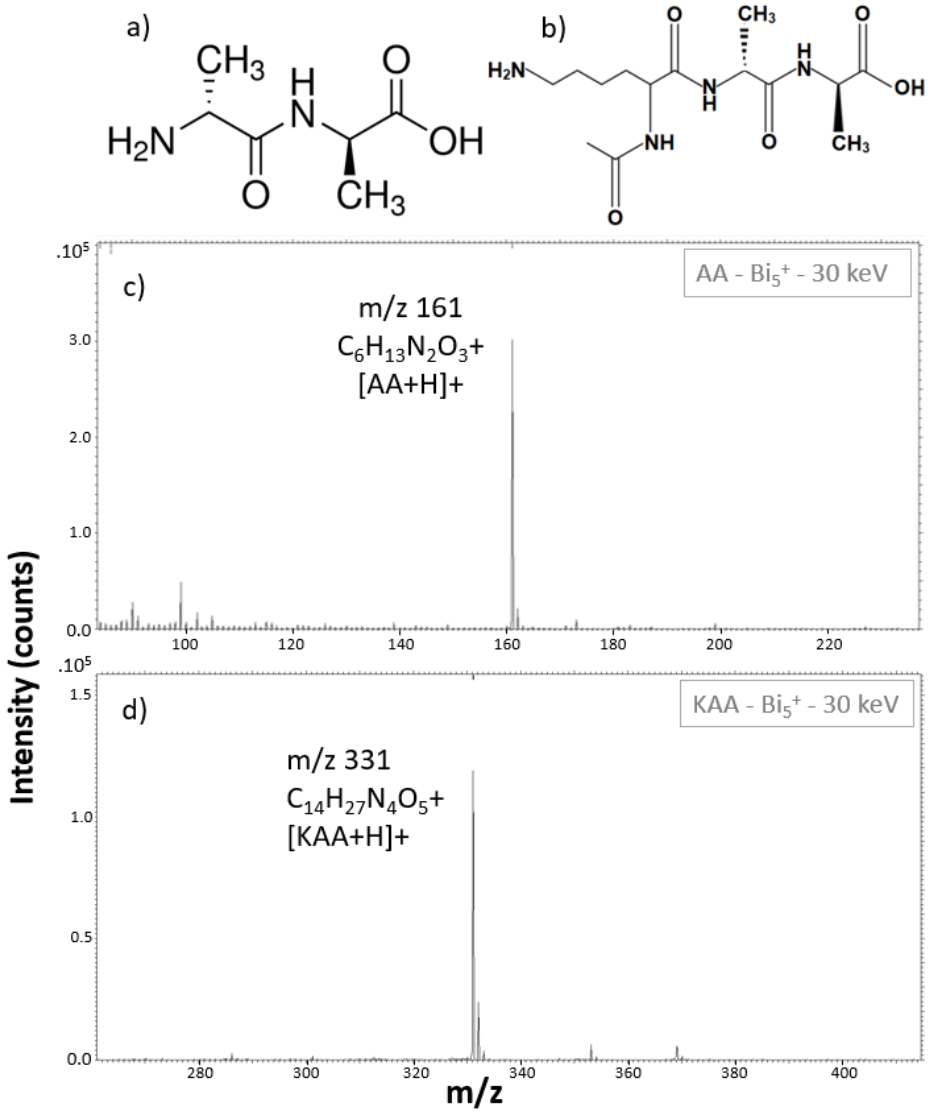

Figure 3.3: Chemical structures of AA (a) and KAA (b) and positive spectra of (c) $[AA+H]^+$ at m/z 161 and (d) $[KAA+H]^+$ at m/z 331.

Their negative mass spectra, shown in Figure 6.6, present the $[AA-H]^-$ and $[KAA-H]^-$ at m/z 159 and 329 respectively. All negative and positive pseudomolecular ion peaks are very intense and are characteristic of these two molecules.

Now that reference solutions have been analyzed, we will first investigate the dynamics of desorption of some characteristic vancomycin fragments, then the desorption of the [V+AA] and [V+KAA] non-covalent complexes and finally, their transfer from a surface onto another.

3.1.2 Investigations on characteristic vancomycin fragments

In addition to the pseudomolecular ions, the characteristic fragments of vancomycin selected for this study were chosen according to the article by Du et al. [64]. Indeed, this research team has already done preliminary work to determine the main fragments in positive and negative modes. However, since working on all positive and negative ions represented a monumental task, especially in terms of data processing, this study will be based on positive ions only. For the discussion, we selected only three characteristic fragments which represent well the behavior of the whole set of obtained data (Table 3.1)

Table 3.1: Positive characteristic ions of vancomycin (chosen from [64]).

Ion	**m/z**
CH_2N^+	28
$C_3H_8N^+$	58
$C_{59}H_{61}Cl_2N_8O_{22}{}^+$	1305
$[V+H]^+$	1450
$[V+Na]^+$	1473

In order to study the effect of layer thickness on the sputtering yield of these characteristic ions (and dimers, see section 3.1.3.4), samples with increasing vancomycin thickness were prepared by spin coating solutions with concentrations ranging from 0.1 to 50 g/L. The thickness was measured by ellipsometry with a n-k-fix model and a refraction index of 1.5 which is a good approximation for proteins. Figure 3.4 shows the obtained calibration curve. As it can be observed, the thickness is directly proportional to the concentration.

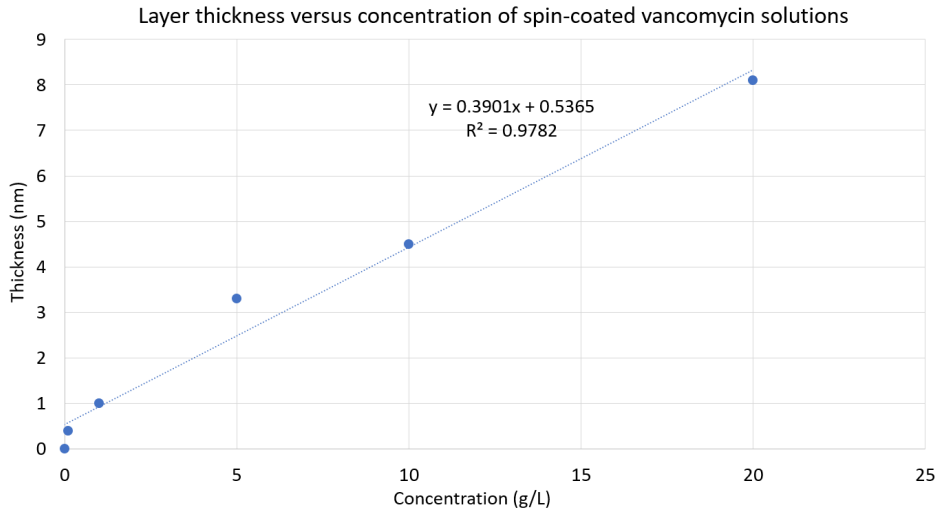

Figure 3.4: Calibration curve of the thickness of the vancomycin layer versus the concentration of the spin-coated solutions.

As it can be seen, the 50 g/L sample is not represented on this graph. This sample was in fact too inhomogeneous (visible to the naked eye) resulting in totally out of range values that were thus rejected. A R-square value of 0.9782 was found, indicating the relatively good quality of the $y = 0.3901x + 0.5365$ linear regression, despite a single set of measurements. The thicknesses shown in the following trends are estimated from this equation in which x is the concentration in g/L. For the 50 g/L solution, the layer thickness was thus extrapolated in order to have an approximation of this sample thickness. Thus, the obtained ±20 nm thickness cannot be taken into account when drawing conclusions and comparisons.

First, Figure 3.5 shows the evolution of CH_2N^+ ion intensity normalized by spectrum total intensity with layer thickness and different ion beams. One can observe that, for Bi clusters, the signal is enhanced with increasing layer thicknesses whereas for Ar-GCIB, it is the opposite.

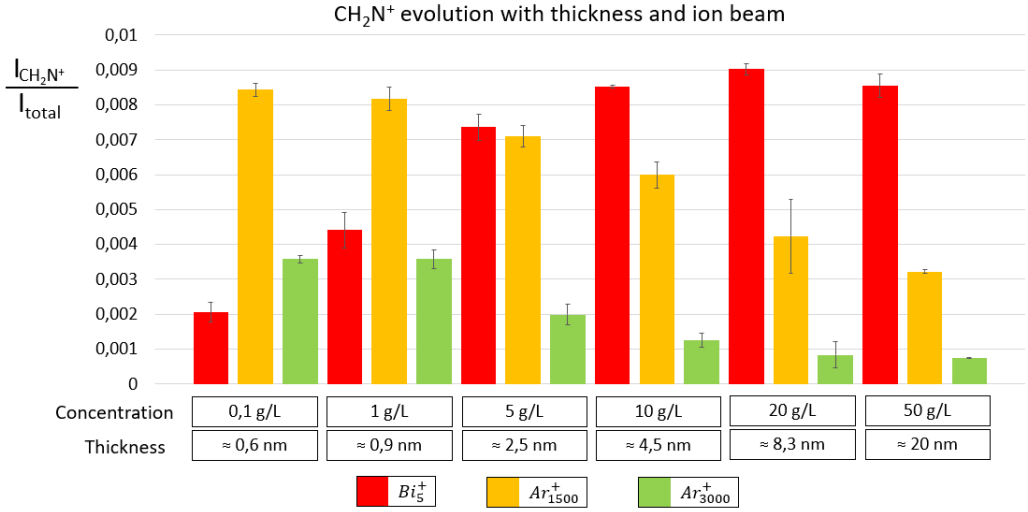

Figure 3.5: Histogram showing the CH_2N^+ signal evolution with the vancomycin layer thickness and with different ion beams. The 0.1 to 50 g/L sample solutions were spin-coated and analyzed under Bi_5^+, Ar_{1500}^+ and Ar_{3000}^+ ion beams.

The downwards yellow and green trends are consistent with a study led by Cristaudo et al. [70]. Indeed, they demonstrated that Ar cluster beams showed systematically ion signal enhancement of characteristic analyte fragments when approaching the interface with the silicon substrate. They showed for the first time a correlation between the energy per atom E/n and the ion signal enhancement near the hard silicon substrate. This correlation was explained by variation of sputtering and fragmentation at the organic-inorganic interface as well as ionization effects. According to their measurements, the increasing sputtering yield in the near-substrate regime play a major role in the signal enhancement. Moreover, they also demonstrated that the closer the impacts are to the hard substrate, the more fragments are produced. This amount of generated fragments decreased with decreasing E/n. A confinement of the Ar cluster

energy happens in the surface region and results in an increase of fragmentation and hence of the sputtering yield of small fragments. When the layer becomes thicker, this energy nanoconfinement effect is attenuated then disappears as the organic layer completely shadows the hard substrate. This leads to a decrease in fragmentation and in fragments sputter yield. Since Ar^+_{1500} clusters have a higher E/n compared to Ar^+_{3000} clusters, they induce more fragmentation leading in a higher fragment signal. For Bi^+_5 clusters, the increase in the red trend with thicker layers is in fact due to the increasing quantity of material deposited on the silicon wafers. The sputtering yield of this CH_2N^+ fragment mirrors the total sputter yield of the sample. With thin layers, the Bi clusters penetrate almost directly in the substrate leading to few fragments to be sputtered. When the layer becomes thicker, more collisions occur in the sample layer resulting in much more fragments to be sputtered. This is a consequence of the much higher E/n of Bi clusters. One can also see that a maximum is obtained for a thickness of ±8 nm which corresponds roughly to the impact crater depth in the organic sample (see Figure 1.11). At this approximate depth, the substrate helps to confine the energy slightly more than for larger thicknesses. A small decrease and then a plateau in the red trend are therefore expected for even thicker sample layers. For the thinner layers, the Bi cluster have enough energy to penetrate into the substrate resulting in a lesser amount of sputtered species.

Second, the $C_3H_8N^+$ ions seem to be sputtered by all primary sources with (Figure 3.6) a maximum in intermediate layer thicknesses for Ar clusters and with larger ones using Bi-LMIG.

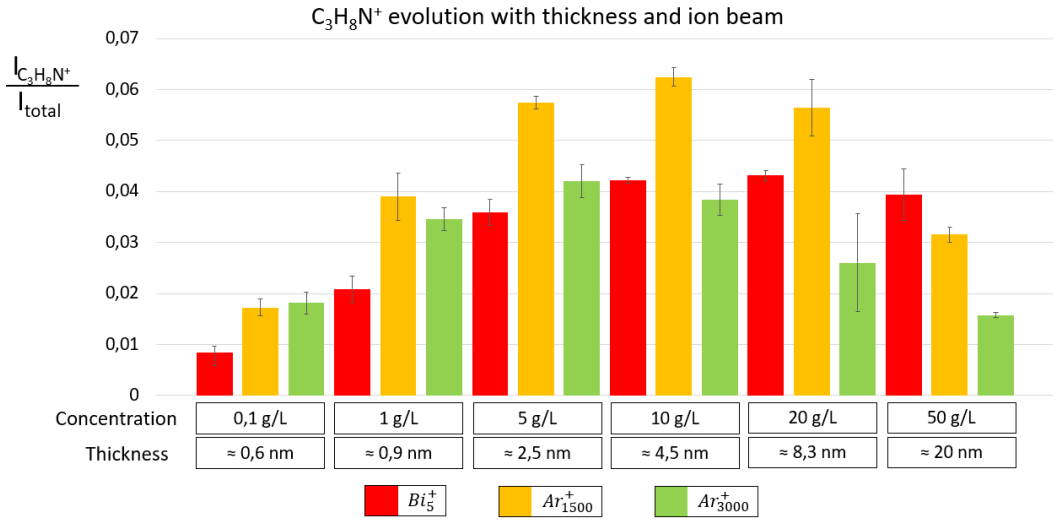

Figure 3.6: Histogram showing the $C_3H_8N^+$ signal evolution with the vancomycin layer thickness and with different ion beams. The 0.1 to 50 g/L sample solutions were spin-coated and analyzed under Bi^+_5, Ar^+_{1500} and Ar^+_{3000} ion beams.

For Bi clusters, the same reasoning than for the CH_2N^+ sputter yield can be applied. For Ar clusters, the shift in maximum sputtering yield towards thicker layers

may be the result of larger fragments being involved. Indeed, the energy required to produce few large fragments is lower than that needed to generate more smaller ones, as fewer covalent bonds have to be broken. Hence, since the density of energy is more confined in thin layers because of the closeness with the hard substrate, it will induce more breaking of covalent bonds and thus more small fragments to be sputtered. With thicker layers, the density of energy is lowered because the substrate is deeper inducing less fragmentation in the vancomycin molecules and hence larger fragments to be favored.

For the three next histograms, before explaining the trends, the blue boxes must be taken into consideration. For these sample, the results have to be taken carefully because of either intensity peaks very close to the background noise or very inconsistent. For the thin $\sim$0.6 nm layer, this could be explained by uneven surface coverage (not optimal for ellipsometry) leading in less probability to sputter fragments and molecules and hence in lower signal. The thicker layers had a much more crystalline and inhomogeneous appearance with large clumps that may lead to resolution (and hence interpretation) issues. Indeed, if the sputtered molecules of the identical mass do not start their trajectory in the analyzer at the same height, they will not arrive at the detector at the same time. The computer will then interpret different masses and the resolution will be affected. Moreover, if molecules are strongly agglomerated in crystal clumps, their probability of sputtering can decrease. Finally, as the concentration increases, the intensity of contamination peaks increased as well leading in intensity ratios that could have been wrong. Therefore, these three elements could have participated in decreasing the sputtering yield of these large ions.

Nevertheless, Figure 3.7 shows trends in the line with previous figures.

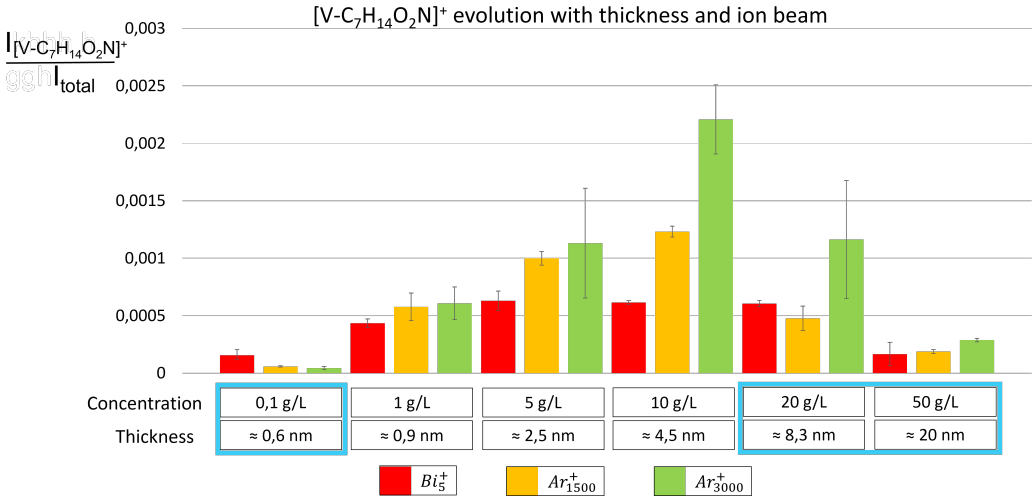

Figure 3.7: Histogram showing the $[V-C_7H_{14}O_2N^+]$ signal evolution with the vancomycin layer thickness and with different ion beams. The 0.1 to 50 g/L sample solutions were spin-coated and analyzed under Bi_5^+, Ar_{1500}^+ and Ar_{3000}^+ ion beams. The samples bordered in blue have to be taken carefully.

$C_{59}H_{61}Cl_2N_8O_{22}{}^+$, is the largest vancomycin fragment observed in positive mode. Breaking of only one covalent bond is required for its formation. Hence, exactly the same reasoning as for the previous figure can be made for all trends in Figure 3.7. However, since it is a very large fragment, the probability to generate it by breaking only one bond is relatively low and explains why the intensity ratios are lowered by a factor of 25-30. Lastly, the higher sputtering yield observed for Ar_{3000}^+ clusters in comparison with the Ar_{1500}^+ ones must be the result of a lower E/n for the larger clusters, leading in reduced fragmentation and more $[V-C_7H_{14}O_2N]^+$ ions being sputtered.

Finally, Figures 3.8 and 6.7 show the evolution in the $[V+H]^+$ and $[V+Na]^+$ pseudomolecular ions sputtering respectively. $[V+Na]^+$ sputtering, having the same kind of trends than above, is shown in the annexes section. The $[V+H]^+$ sputtering follow identical trends for both Ar-GCIBs, but a totally opposite one when using Bi clusters. Indeed, is seems that Bi clusters tend to sputter the pseudomolecular ion with a maximum for thin layers although it was expected to appear for thicker ones.

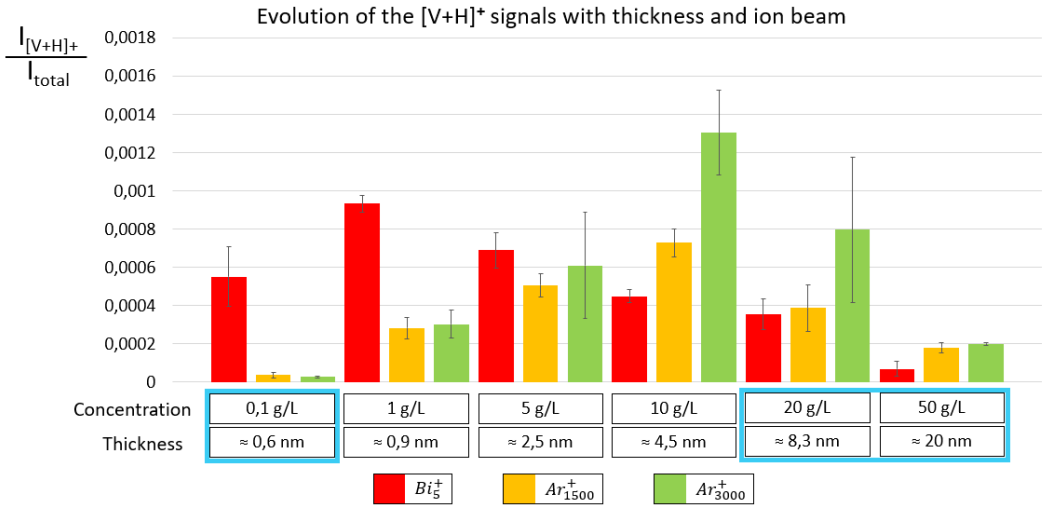

Figure 3.8: Histogram showing the $[V+H]^+$ signals evolution with the vancomycin layer thickness and with different ion beams. The 0.1 to 50 g/L sample solutions were spin-coated and analyzed under Bi_5^+, Ar_{1500}^+ and Ar_{3000}^+ ion beams. The samples bordered in blue have to be taken carefully.

One explanation to this unexpected observation could arise from a different effect and/or mechanism of ionization for this species. Indeed, all studied vancomycin fragments, being charged upon covalent bond rupture, do not need to receive a charged species to be extracted and thus analyzed. The vancomycin molecules, on the other hand, must be given one to do so. The $[V+Na]^+$ ions receive a sodium cation and are thus following its sputtering yield trends (Figure 6.8). Indeed, these ions being a contamination present in the bulk of the samples, their trends are upwards with the quantity of deposited material. On the other hand, Figure 3.9 shows the evolution of the H^+ sputtering with thickness and ion beams. This first confirms that, for Ar clusters, there is more fragmentation for thin layers than for thicker ones since the quantity of sputtered protons is lowered when the layers are larger. We can thus assume that for the Bi clusters, the sputtering of $[V+H]^+$ follows the one of H^+ which explains why the sputtering maximum is shifted towards thinner layers. However, this should be similar for Ar clusters but the yellow and green trends in Figure 3.8 keep their maximum at thicker layers. Our interpretation is that the sputtering under Bi-LMIG is more influenced by the ionization effects and/or mechanisms, while the sputtering under Ar-GCIB by the quantity of deposited material and fragmentation. Indeed, under Ar clusters, even if the vancomycin has to receive a proton to be analyzed and even if there is more H^+ sputtered with thin layers, the sputtering trends with thickness will rather follow the higher probability of sputtering the intact molecule at thicker layers.

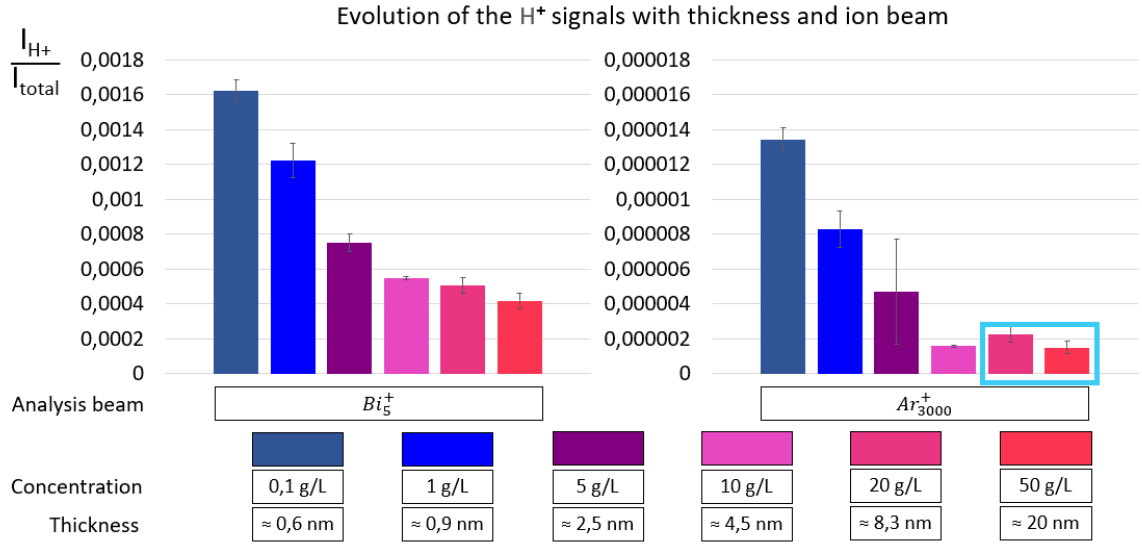

Figure 3.9: Histograms showing the proton signals evolution with the vancomycin layer thickness and with different ion beams. The 0.1 to 50 g/L sample solutions were spin-coated and analyzed under Bi_5^+, and Ar_{3000}^+ ion beams. The bars bordered in blue have to be taken carefully.

Now that a complete study of some characteristic fragments and the pseudomolecular ions has been conducted, the desorption of non-covalent complexes can start to be investigated !

3.1.3 Complexes analyses

3.1.3.1 First trials

After preparing and depositing the different equimolar complex solutions (66.67 µmol/L into mQ water and NH_4Ac buffer) on the cleaned silicon wafers, the first analyses, under Bi_5^+, Ar_{3000}^+ and Ar_{5000}^+ primary beams, could be achieved in both polarities. When bound together, V+AA and V+KAA have monoisotopic mass of 1608.5 and 1778.6 Da respectively and should therefore be visible with a delta of ±1 Da compared to these masses in the spectra. Unfortunately, none of these two complexes could be detected under any of the tested conditions. As it did not work out with small Bi_5^+ cluster ion beam, we tested the large argon ones. Indeed, their energy per atom (E/n) is lowered by three orders of magnitude as they are composed of thousand of atoms, and hence induce less extensive fragmentation. Figure 3.10 shows the first V+AA and V+KAA spectra in positive mode. The spectra of the other tested conditions are not shown.

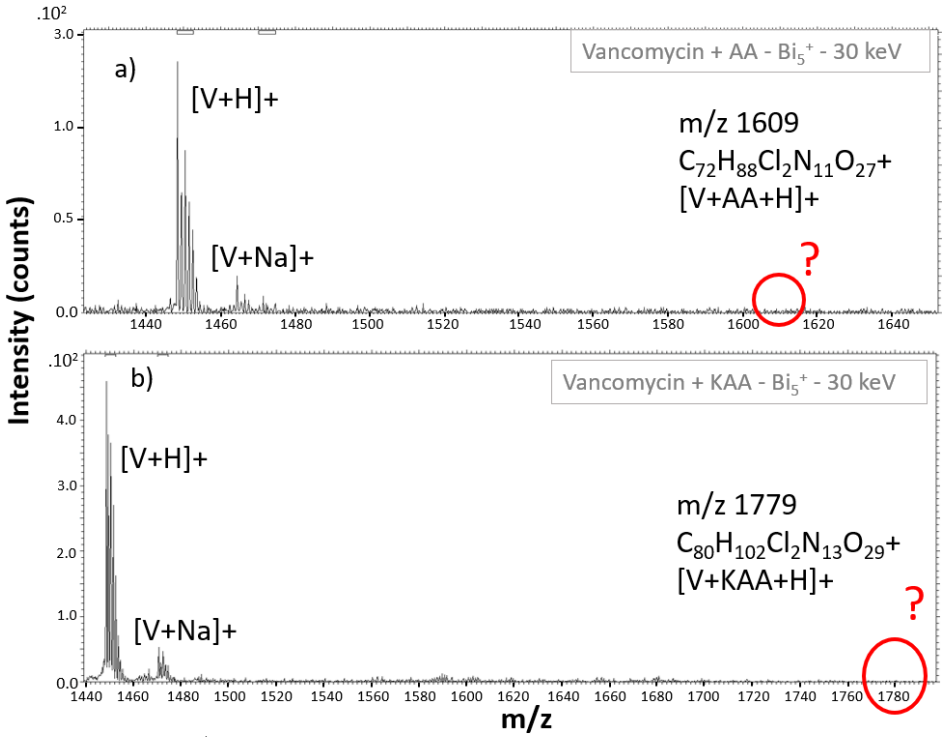

Figure 3.10: 30 keV Bi_5^+ spectra of V+AA (a) and V+KAA (b) not showing any complex peak.

The absence of detection of these complexes could be explained by several factors:

- Problems with their formation in solution could have happened;
- Their concentration in solution may have been to low to allow their sputtering in sufficient quantity to discern them in the spectra.
- The primary beams may have caused dissociation upon impact;

- Even if present in sufficient quantities in the prepared solutions and desorbed intact, they could have dissociated in the gas phase;
- The masses of the two components are very different, favoring the release of the smaller one under centrifugal effect;
- Maybe issues in the ionization could have occurred.

Something interesting on these mass spectra is that the $[V+Na]^+$ peaks are much less abundant, in comparison with the $[V+H]^+$ ones, than in the reference mass spectra. These samples were undoubtedly less sodium-contaminated. This could be explained by slight differences in sample preparation. The difference between the Na-peaks in a vancomycin reference spectrum and in a V+KAA spectrum is depicted in Appendix (Figure 6.9).

Since no results were conclusive, it was natural to wonder whether complexes were actually formed in the prepared solutions. In order to be completely sure that the complexes were present in the solutions, electrospray ionization mass spectrometry was performed.

3.1.3.2 ESI analyses

For ESI analyses to confirm the presence of the complexes, solutions of V+AA and V+KAA (see section 2.2) were prepared in a 70:30 (v:v) water-methanol solvent. Methanol, being more volatile than water, allows a better evaporation of the solvent and therefore better ionization of the molecules and a better signal [69]. Fortunately, these analyses allowed to confirm their presence in solution. Figure 3.11 shows the ESI spectra of V+AA and V+KAA solutions.

Since the x-axis is the mass to charge ratio and the ions are doubly charged, the peaks emerge at the half of their respective mass. Actually, the complexes lose three hydrogen atoms, which explains why the peaks appear at a slightly lower mass. The very small mass differences between these peaks and their theoretical mass (2.79 and 2.18 ppm respectively) proved that their attribution could only be to these complexes.

At some point during the year, contamination issues occurred. Indeed, spectra of the V+KAA solutions prepared with ratio ranging from 1:1 to 1:10 (see section 2.2) were full of unidentified intense peaks. We thus thought that ESI could bring us some supplementary information about the quality of the samples. In that line, others ESI analyses were made in order to asses which purchased powders was contaminated. Figure 6.10 shows the ESI mass spectra of the 1:1 to 1:8 (V:KAA) solutions. It can be seen from this figure that as the proportion of KAA increases, the ratio of the intensity of the complex peaks to those of vancomycin alone increases, suggesting that

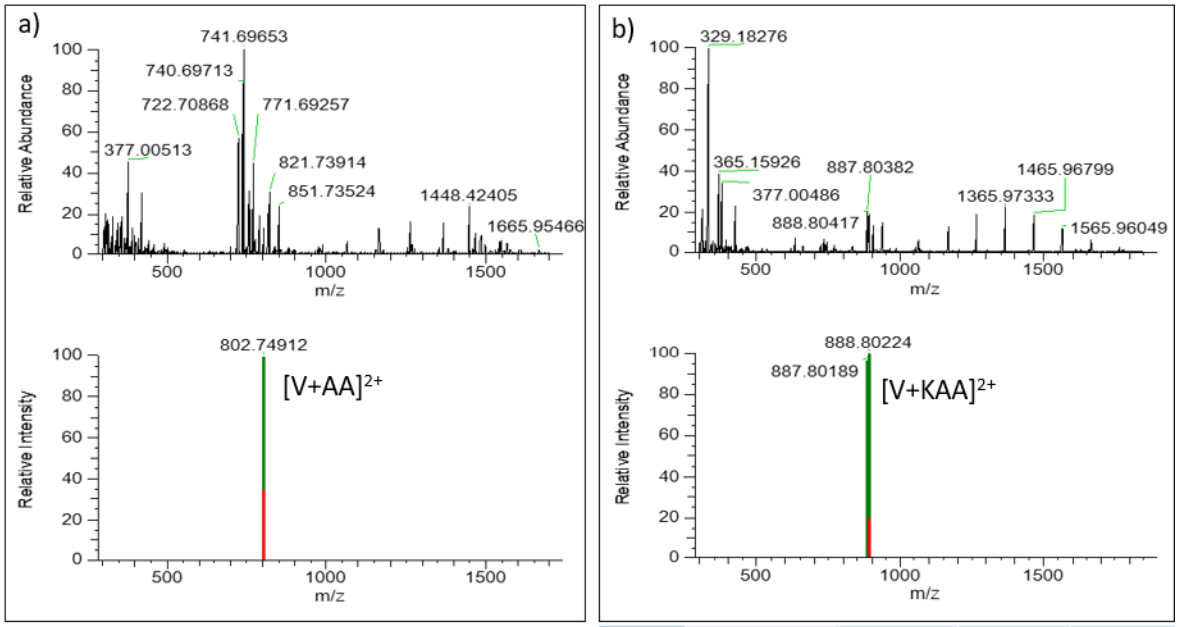

Peak Mass	Display Formula	MS Cov. [%]	Delta [ppm]	Theo. mass
802.75137	$C_{72}H_{85}O_{27}N_{11}{}^{35}Cl_2$	91.69	2.79	802.74912

Peak Mass	Display Formula	MS Cov. [%]	Delta [ppm]	Theo. mass
887.80382	$C_{80}H_{99}O_{29}N_{13}{}^{35}Cl_2$	99.88	2.18	887.80189

Figure 3.11: ESI spectra of (a) V+AA and (b) V+KAA solutions. The tables below shows, among other data, the mass delta of the peak compared to the theoretical mass of the molecules.

more complex has been formed. This seems quite logical and follows Le Chatelier's theory. Moreover, as the proportion of KAA increases, the intensity of many peaks increases too. It turned out that the KAA powder (as well as the vancomycin powder, but to a lesser extent) was presumably contaminated. This may be due to the freezing and thawing of the powder which may have damaged the sample or caused molecular rearrangements.

3.1.3.3 Detection of [V+KAA]

Since it was clear that the complexes were formed in aqueous solutions, it was decided to pursue the SIMS investigations on these two systems, and try to find experimental conditions that allow the desorption of these non-covalent complexes. The first newly tested conditions were to simply increase the concentration by a factor of 16.67 (1 mM) to deposit more material on the substrate. These solutions were drop-cast on silicon and PET in order to have different substrate hardnesses and thicker layers than in previous experiments. They were finally analyzed under Bi_5^+ and $Ar^+_{1500-3000}$ ion beams. After an hour of analysis under Ar^+_{3000} the first V+KAA complexes could be detected. After that V+KAA was detected many other times but it was not the case for V+AA. The absence of V+AA complexes detection might be due to the use of D-Ala-D-Ala ligands instead of acetylated-D-Ala-D-Ala (Ac-AA). Indeed, the acetyl moiety allows to form an additional hydrogen bond between the ligand and the vancomycin

molecule. Figure 1.14a shows the five hydrogen bonds (in green) between V and Ac-AA, but if the leftmost group $-C(=O)CH_3$ of the latter molecule is removed, only four remain. This observation can lead to these conclusions:

- There may be a "mass-missmatch" effect between the V and AA molecules leading to the ejection of the smaller one by centrifugal effect. This hypothesis will be explained in more detail in the section 3.1.3.4.
- The difference of one hydrogen bond between the two complexes could already represent a limitation for the desorption of non-covalent systems by ToF-SIMS, at least for the tested conditions. The ejection process could be energetic and violent enough to break the weak H-bond interactions and hence the three-dimensional structure of the complex.

The first success was by analyzing dried droplets (DD) of equimolar aqueous solutions of V+KAA (1 mM) with the Ar^+_{3000} ion beam. A small peak (Figure 6.11) could be seen emerging from the background noise but its intensity was not high enough to draw any initial conclusion. Later, still with DD and Ar^+_{1500} and Ar^+_{3000} ion beams, but this time increasing the proportion of KAA compared to vancomycin, slightly more intense peaks were visible. Figure 3.12 shows the more intense complex peaks obtained with Ar^+_{1500} primary ions but with contamination. On this mass spectrum, the pseudomolecular group of peaks is visible at their respective m/z but other peaks emerged at a mass delta of 6 Da (colored in red and referred to as $[V(+Na)+X]^+$ in the figure). In the mass range of the V+KAA complex four peaks were out of the background noise. The pseudomolecular ion isotopic distribution of the V+KAA complex was quite visible at m/z 1780. Once again, 6 Da further, a group of peaks emerged but this time 2-3 times more intense and is referred as to V+KAA+X. 38 Da further (m/z 1818), another peak is visible (colored in blue and referred to as $[V+KAA+Y]^+$, in the figure). And finally, still 6 Da further (m/z 1824 and colored in purple) another one thus reflecting the $[V+KAA+Y+X]^+$ isotopic distribution have emerged. These X-additional peaks could be the result of replacement of the hydrogen atom by a lithium and by potassium but it seemed unlikely since no lithium characteristic peak was present on the spectrum. For the Y ones, it could be a potassium atom that was added to the complex but the potassium peak in the mass spectrum is really not intense. Both of their intensities are visible in Figure 6.12. If it is impossible to these X and Y adducts to be Li^+ and K^+ respectively, it could probably correspond to some rearrangements between fragments of the complexes.

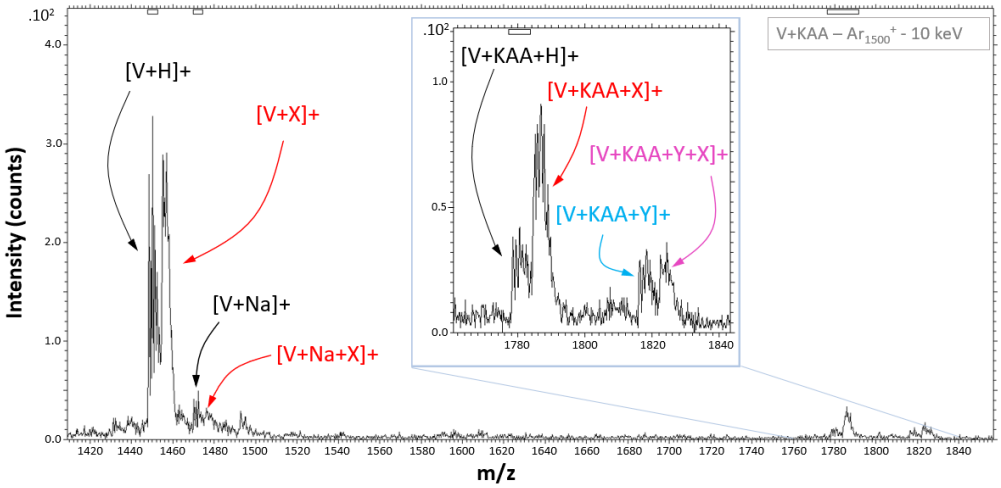

Figure 3.12: Positive mass spectrum of aqueous solution of V+KAA (in 1:2 ratio) droplets dried on silicon wafers showing some particular isotopic distributions ("X" and "Y" corresponding to unknown adducts). Analysis beam: 10 keV Ar^+_{1500}.

Figure 3.13 shows a mass spectrum of the exact same sample than in Figure 3.12 but analyzed with Ar^+_{3000} instead of Ar^+_{1500}. The isotopic distribution at m/z 1818 corresponding to $[V+KAA+Y]^+$ is still present while the ones corresponding to the X-adduct are not. This could thus confirm that X belongs to contamination.

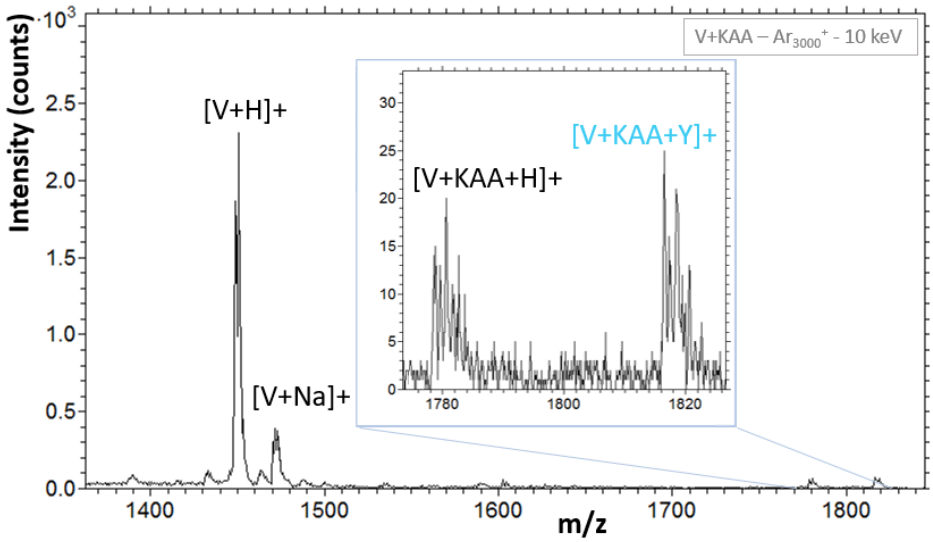

Figure 3.13: Positive mass spectrum showing the V+KAA complex peaks and another isotopic distribution corresponding to $[V+KAA+Y]^+$. Analysis beam : 10 keV Ar^+_{3000}.

Now that the V+KAA complexes could be detected, some trends could be shown. In order to always work with the same method, the sputtering yields of the complexes alone (without X and Y) are compared to the sum of those of the pseudomolecular ion peaks ($[V+H]^+$ and $[V+Na]^+$).

Firstly, Figure 3.14 shows a histogram of the sputtering yields of $[V+KAA]^+$ complex ions versus the sum of the pseudomolecular ion yields. It is apparent that the proportion of complex increases by a factor of 3.3 with a doubled ratio of KAA. As with ESI, this is explained by the higher complex formation by Le Chatelier's law. However, one can also see that when larger clusters are used the yield of V+KAA ions decreases. This is quite surprising since, in theory, larger cluster (for the same kinetic energy) should have decrease the number of fragmentation leading in higher complex yields.

Two other elements regarding the analysis of these samples remain to be discussed. In Figure 3.14, only results for dried droplets of samples analyzed by Ar-GCIB are shown. Indeed, when they were spin-coated (SC) only two spectra showed the complex peaks but the signal/noise ratio was too low to be presented and discussed. Moreover, when these DD samples were analyzed by Bi-LMIG, absolutely not a single complex peak was seen out of the noise. This can be explained by the large thickness of sample deposited on silicon wafers and the small size of the Bi clusters. Indeed, Cristaudo et al. [71], showed an enhancement of the sputtering yield for ultrathin layers of polymer on hard substrate (silicon wafers). This could thus likely be applicable to this situation. In addition, the small clusters, containing less atoms, have thus a higher energy per atom (E/n = 6 keV/Bi atom compared to a few eV/Ar atom) increasing the fragmentation probability [40]. The combination of these two effects may therefore be responsible for the complexes not being able to be desorbed intact under these conditions.

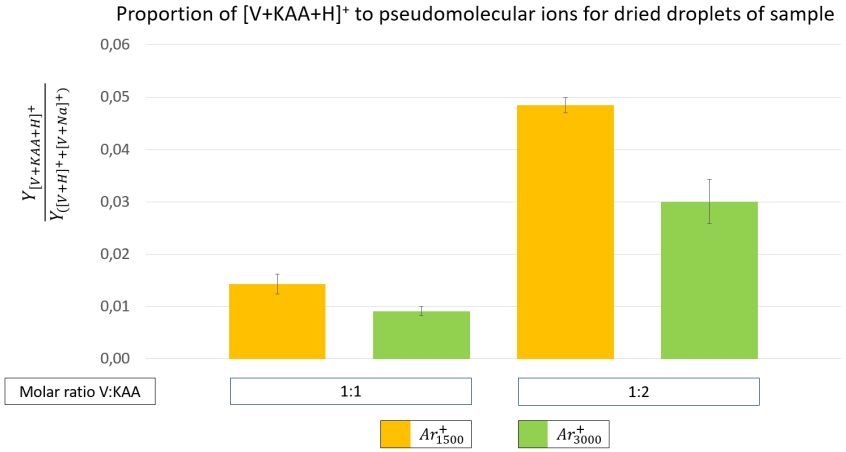

Figure 3.14: Histogram showing trends of $[V+KAA+H]^+$ peaks over pseudomolecular ions peaks for dried droplets of sample dissolved in water. The colors indicates the analysis ion beam.

Secondly, we finally succeeded to detect the V+KAA complexes with thin spin-coated vancomycin layers and even with Bi cluster ion beams. Since the previous aqueous sample did not give results when spin-coated, we prepared samples in a 70:30 (v:v) water:methanol solvent in order to mimic the conditions that seemed favorable in ESI. The obtained results are indeed somewhat more promising than without methanol

(for these SC samples) and are given as a histogram in Figure 3.15. Although unlikely due to their high volatility, some methanol molecules may have been trapped in the sample during the drying process, resulting in a yield enhancement by proton transfer.

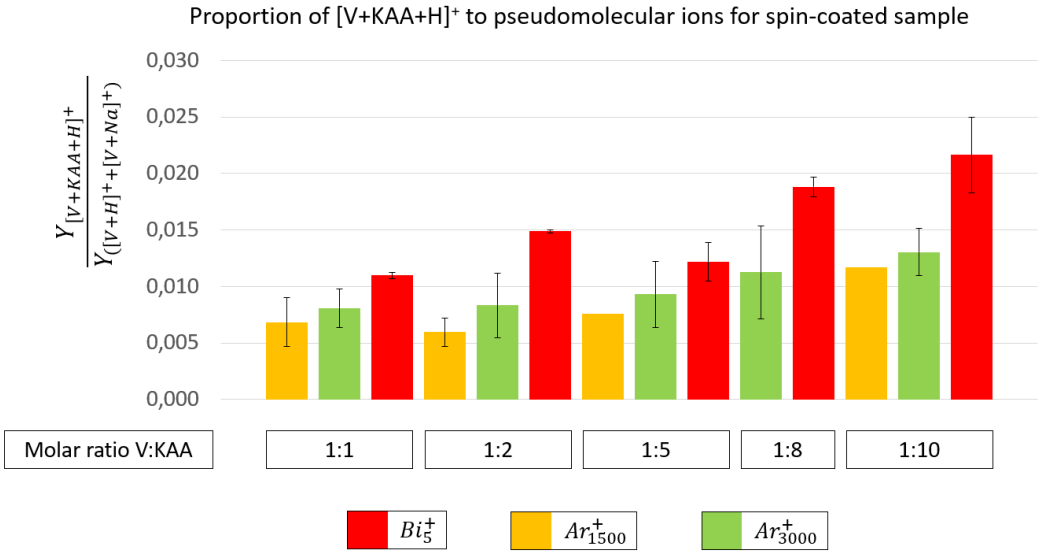

Figure 3.15: Histogram showing tendencies of $[V+KAA+H]^+$ peaks over pseudomolecular ions peaks for spin-coated sample in a 30% methanol solvent.

As for the previous results, the proportion of the complex peaks tends to increase with the KAA ratio. It also has an increasing trend when the size of the Ar cluster increases. This is explained by the decreasing E/n leading in less fragmentation. However, when the analysis is carried out by small Bi_5^+ cluster ion beams, the sputtering yield increases even more. This is quite contradictory with the previous conclusion but could be explained by the fact that the emission of species does not follow the same effects when the size (or nature) of the primary beam changes. As for the sputtering of the pseudomolecular ions (see section 3.1.2), under Bi cluster ion beams and for thin layers, the emission of $[V+KAA+H]^+$ seems to follow the one of H^+. Under Ar-GCIB, the sputtering of this complex ion is more dependent to the layer thickness and fragmentation. This can thus explain the relatively higher sputtering yields in Figure 3.14 compared to those in Figure 3.15. It might have been interesting to compare the V+KAA signals under Bi_5^+ ion beams for the SC and DD samples but, as explained above, no results could be obtained from the latter.

Even if detected several times, the V+KAA complex was in general very hard to detect for the majority of the experiments. Indeed, the project of analyzing intact H-bound non-covalent complexes was quite ambitious since these interactions are among the weakest. Moreover these results were frequently not reproducible. This could be explained by (i) contamination, (ii) slight variability in the ion doses causing differences in the sputtering yields, (iii) uneven thicknesses causing different flight times and leading in low mass resolutions, (iv) issues occurring in the ionization processes,

(v) centrifugal effects causing the ejection of the lighter partner, etc. Because of this non-reproducibility and since vancomycin dimer peaks were almost always present in the spectra, the next section will investigate the desorption of these other non-covalent complexes.

3.1.3.4 Vancomycin dimers

As it was written in the previous section, vancomycin dimers were often detected using time-of-flight secondary ion mass spectrometry. Indeed, a group of peaks corresponding to two vancomycin molecules was visible in the mass spectra of the vancomycin reference and complex samples. Since these species are bound by weak interactions, they constitute non-covalent complexes and deserve a closer look.

Especially from NMR studies, it is now well established that glycopeptide antibiotics such as vancomycin tend to form a "back-to-back" dimer due to four hydrogen bonds between their peptide backbone in an anti-parallel configuration. This dimerisation also enhances ligand binding by the antibiotics [59]. According to Schäfer et al. [63], vancomycin and its analogues are even predominantly dimeric in solution. The vancomycin molecule forms thus non-covalent complexes with its peers as well as with dipeptide ligands. Since the dimer peaks were even more frequently present than the V+(K)AA ones in the mass spectra, we decided to study them as well. This suggests that it could be possible to detect dimers bound to their ligands as it was the case for ESI analyses (Figure 6.13). In these analyses [72], they even managed to analyze quadrimers of vancomycin each bound to a ligand.

Although these multimers could not be detected in SIMS, some particular peaks have emerged at higher m/z than those of the dimer in some spectra. Indeed, in Figure 3.16, two groups of peaks, in addition to that of the dimer alone, are visible. Both mass differences correspond to 28 Da suggesting that the adduct is the same in both cases. Since the resolution is quite low, we cannot ensure a correct attribution to these mass differences and the adduct is thus referred to as X in the figure. Our interpretation is that X could be a CH_2CH_2 or a CO (or even other fragments) that binds to each vancomycin monomer and probably in the vancomycin binding pocket where there are most opportunities for interactions. But it is more likely to be the latter because CO is smaller. Indeed, it should thus be much more protected in the binding pocket and, because of its oxygen atom, it can participate to hydrogen bonding. Nevertheless, this remains speculation.

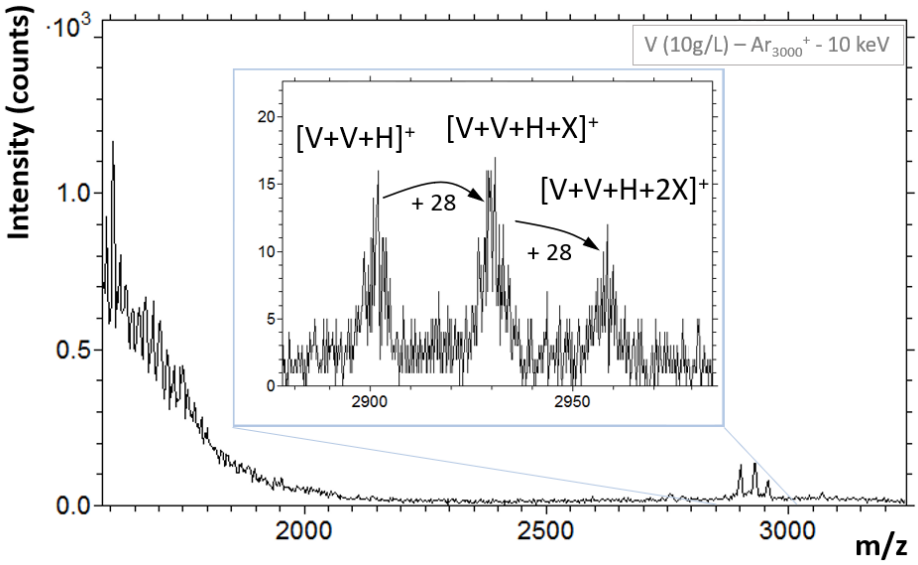

Figure 3.16: Spectrum showing 3 isotopic distributions corresponding to the dimer (left), dimer+X (middle) and dimer+2X peaks (right).

These two additional groups of peaks were visible when vancomycin reference samples of 1-5-10 g/L were analyzed by Ar clusters. The peaks were actually more intense using Ar^+_{3000} than Ar^+_{1500} cluster beams (visible in colors in Figure 6.14a) which is most probably reflecting the decrease in fragmentation due to a lower energy per atom ratio in large clusters. Indeed, when the same samples were analyzed with Bi clusters, none of the two additional distributions were seen (Figure 6.14b). This can be explained by the same reasoning, as it nicely follows the expected trend of increasing fragmentation following the E/n ratio. The Bi^+_5 clusters, having an E/n much higher than the Ar clusters, induce much more fragmentation and prevent the detection of the V+V+X and V+V+2X non-covalent complexes. Since these peaks could not be seen for every conditions, the comparative study that follows will only take into account the intensities of the $[V+V+H]^+$ peaks. They will be compared to the pseudomolecular ion peak intensities or to the total intensities of the mass spectra.

First, Figure 3.17 shows the evolution of the vancomycin dimer peak relative to the pseudomolecular ion peaks with the concentration of the spin-coated solution (and therefore sample thickness). An increasing trend can clearly be observed. Two hypotheses can be proposed to explain this, and both rely on the sample concentration/thickness. Firstly, when the vancomycin concentration increases, the complex formation is enhanced in solution due to Le Chatelier's law. Hence, higher amount of complexes are present in the solid phase on the substrates. Secondly, the very thin layers obtained by the lower concentration solutions suggest uneven distributions of the surface coverage. As the concentration increases, the percentage of surface coverage rises and so does the probability of two vancomycin monomers to be side by side and sputtered together as dimers.

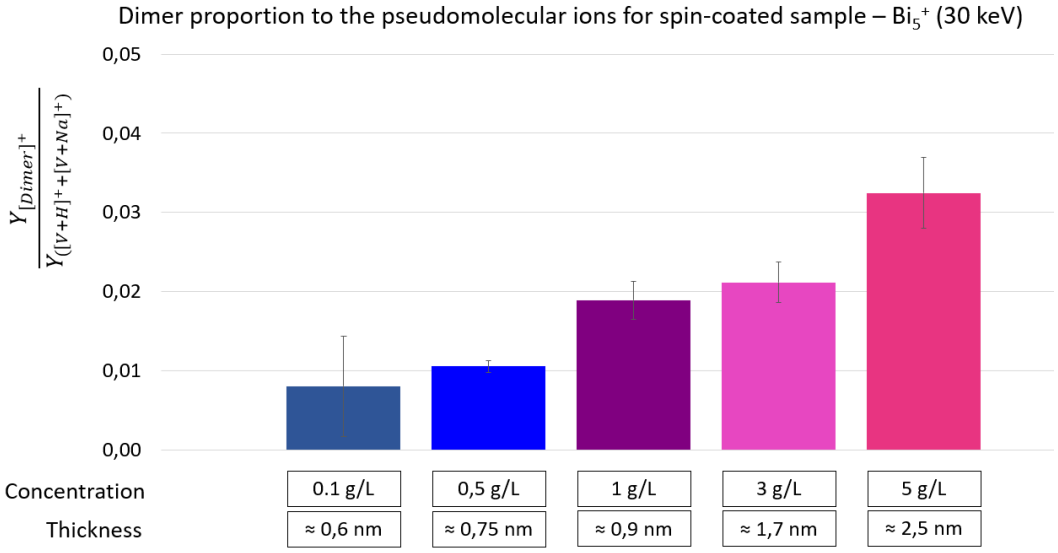

Figure 3.17: Histogram showing the dimer proportion increase when the vancomycin concentration rises. The 0.1 to 5 g/L sample solutions were spin-coated and analyzed under Bi_5^+ cluster ion beams.

Second, the histogram presented in Figure 3.18 shows the evolution of the dimer peak intensity over the total spectral intensities for different spin-coated solutions and for different analysis beams. As explained in section 3.1.2, the results obtained for samples in blue boxes must be taken carefully because of uneven surface coverage and inconsistent SIMS measurements. Nevertheless, the data show that vancomycin dimers are emitted from the surface by all primary ions and that the dynamics of emission as a function of the layer thickness is different for Bi_5^+ clusters (6 keV/atom) than for $Ar_{1500-3000}^+$ clusters (a few eV/atom). Indeed two trends can be observed, the red one for the Bi clusters and the yellow and green ones for the latter. Both trends are rising and then decreasing with maximum at different thicknesses. The red trend seemed to have a maximum for thinner layers while the two others for thicker ones. Of course, care must be taken as the extremes (lowest and largest concentrations) were not as reproducible as the others.

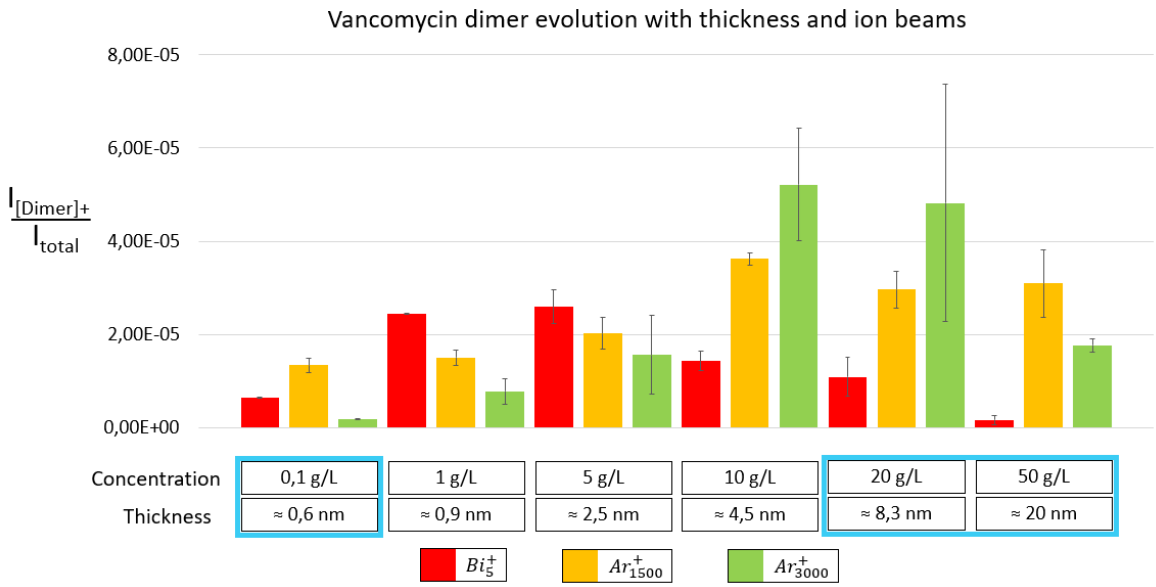

Figure 3.18: Histogram showing the dimer signal evolution with the vancomycin layer thickness and with different ion beams. The 0.1 to 50 g/L sample solutions were spin-coated and analyzed under Bi_5^+, Ar_{1500}^+ and Ar_{3000}^+ ion beams.

The evolution of the $[V+H]^+$ signal over the total spectral signal presented in Figure 3.8 can help us to explain these results on dimers. Firstly, it can be seen that both signal dependencies to the thickness are similar. As for $[V+H]^+$ emissions, these results can be explained by different influences between the sputtering under Bi-LMIG and Ar-GCIB. For the red trend, our interpretation is that the dimer emission, as well as the monomer one, mirrors the sputtering of protons higher for thin layers. The sputtering under Bi clusters is thus more influenced by ionization effects and/or mechanisms while under Ar-GCIB by the quantity of deposited material and the size of the ejected species. Indeed, under Ar clusters, even if the dimer has to receive a proton to be analyzed and even if there is more H^+ sputtered with thin layers (see Figure 3.9), the upwards emission trends with thickness rather follow the higher probability of sputtering the intact dimer at thicker layers.

A final point of interest is the ease with which vancomycin dimers are detected when they are bound by 4 hydrogen bonds, while the V+AA complexes have never been observed in the mass spectra. This could be explained by "mass-missmatch" effect between the two molecules. Indeed, we hypothesise that when two associated molecules in UHV are spinning on themselves, the lighter one is more likely to be ejected from the complex if the difference between the masses of the two molecules is important. If the masses are similar, such as in vancomycin dimers, this probability decreases. Of course, this could also have been explained by more electrostatic and van der Waals interactions between the two vancomycin molecules just resulting from the length of the peptide backbone. Indeed, the small D-Ala-D-Ala dipeptide, although in

the vancomycin binding pocket, thus would have less of these additional interactions leading in a non-covalent complex which is, in the end, not as tightly bound as the dimer.

Now that V+KAA and vancomycin dimer complexes could be detected intact, proving their desorption upon impact without breaking weak interactions, the transfer of these species can be investigated.

3.1.4 Transfers

Since (i) V+KAA complexes were often difficult to detect, (ii) most results were inconsistent and (iii) the KAA sample powder was contaminated, most of the work was devoted to studying the desorption of vancomycin dimers. We therefore chose to study the transfer only for the latter, which showed favorable static SIMS analysis results.

For the transfer experiments, three 10 µL drops of 20 g/L vancomycin reference solution were dried one after the other on smaller but thicker wafers (the targets). After that, transfers were carried out for 15 hours and 3 hours under Ar^+_{5000} and Ar^+_{3000} cluster bombardment respectively. Finally, the collectors were analyzed by the three ion beams and 2D images were obtained by scanning the whole surfaces under 30 keV Bi^+_5 ion beams.

Interesting results were obtained for particular fragments and vancomycin pseudo-molecular ions. The mappings in positive mode are thus based on the ions presented with their respective monoisotopic mass as described in Table 3.2.

Table 3.2: Positive ions chosen for 2D imaging.

Ion	**m/z**	**Related to**	**Ion**	**m/z**	**Related to**
Si_+	28	Substrate	$C_3H_8ON^+$	74	Vancomycin
$SiOH_+$	45		$C_6H_{14}N^+$	100	
CH_2N^+	28	Vancomycin	$C_7H_{14}O_2N^+$	144	
CH_4N^+	30		$[V-C_7H_{14}O_2N]^+$	1303	
$C_2H_4N^+$	42		$[V+H]^+$	1448	
$C_3H_6N^+$	56		$[V+Na]^+$	1470	
$C_3H_8N^+$	58				

Figure 3.19 shows the collectors 2D images for the sum of the Si^+ and $SiOH^+$ peaks and the sum of all characteristic vancomycin ion peaks.

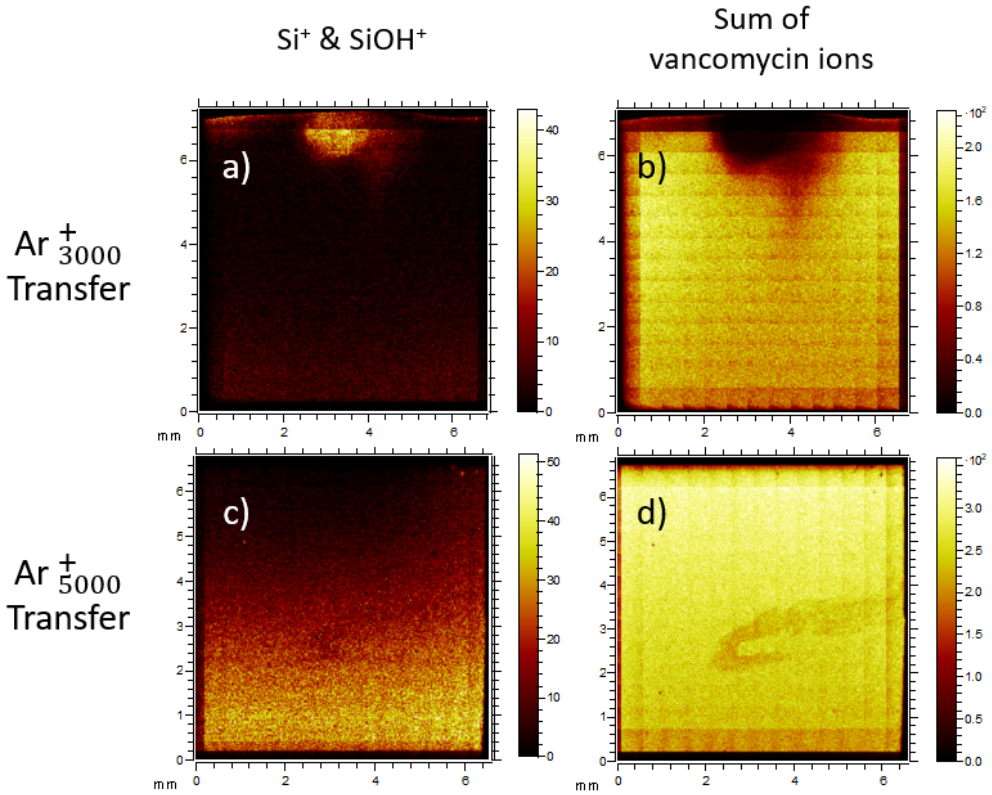

Figure 3.19: Chemical signal intensity images after Ar^+_{3000} (a & b) and Ar^+_{5000} (c & d) transfers. a) and c) displays the sum of the Si^+ and $SiOH^+$ signals while b) and d) the sum of all characteristic vancomycin ions signals.

These 2D mappings confirm that material was transferred from the targets onto the collectors. Indeed, the Si^+ and $SiOH^+$ signals, originating from the silicon substrate, are strongly attenuated in the upper regions of the collector where the characteristic vancomycin ions peaks show maximum intensity. The semi circular shape present on all mappings, can only be explained by the material deposition from the target. This pattern of deposition is often encircling a spot in the top center of the collectors, such as for this Ar^+_{3000} transfer for instance. This spot is due to a part of the primary Ar cluster ion beam impinging the collector surface during transfer. Therefore, the molecules and fragments transferred on this spot are sputtered upon impact of the Ar-GCIB leaving the silicon wafer bare. This explains the clear spot in Figure 3.19a and the dark one in Figure 3.19b. One can also observe a downwards decrease in the intensity of vancomycin ions peaks and an increase in the one of the characteristic substrate ions which suggests a gradient of deposited amount from the top centers of the collectors and in all directions.

If we look closer to three of the characteristic vancomycin ions, similar results were obtained and are shown in Figure 3.20. These 2D mappings show two characteristic

fragment ions of vancomycin, *i.e.* $C_6H_{14}N^+$ (a & b) and $[V-C_7H_{14}O_2N]^+$ (d & e) and the sum of the two pseudomolecular ions (c and f). The spots that were in Figure 3.19a-b are also found in Figure 3.20a and can be guessed in Figures 3.20b-c.

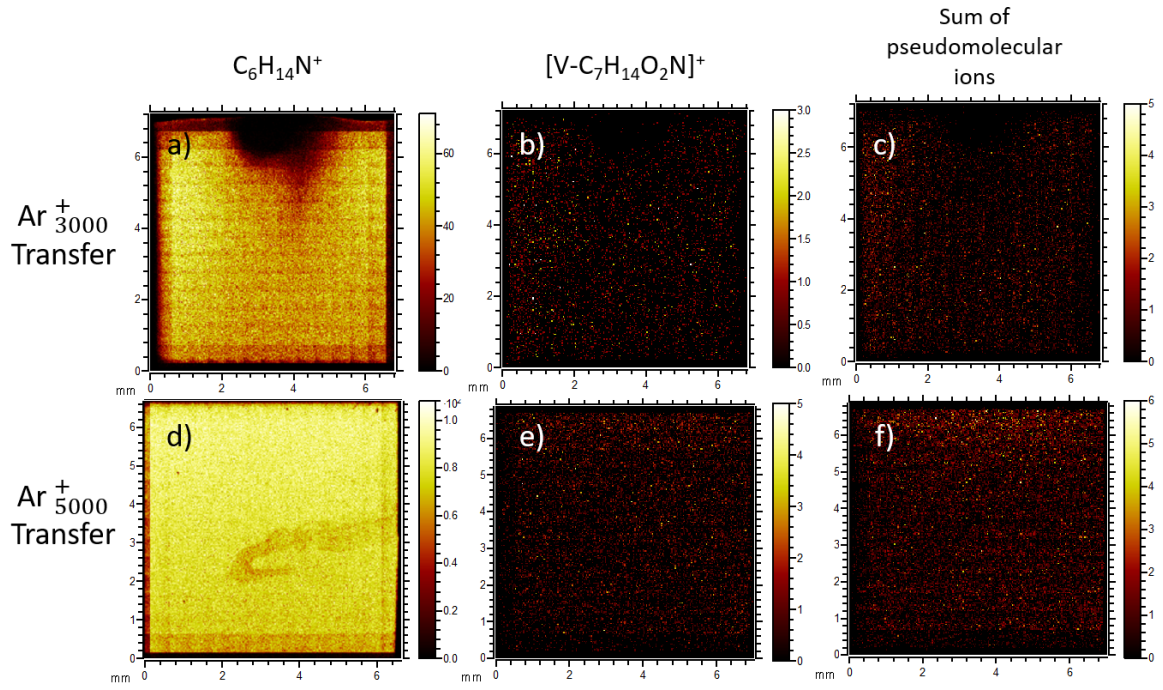

Figure 3.20: Chemical intensity images after Ar^+_{3000} (a, b & c) and Ar^+_{5000} (d, e & f) transfers. a) and d) displays the $C_6H_{14}N^+$ signal, b) and e) the $[V-C_7H_{14}O_2N]^+$ signal and c) and f) the sum of $[V+H]^+$ and $[V+Na]^+$ signals.

On the a) and d) mappings, it can easily be seen that the $C_6H_{14}N^+$ ion has completely covered the collector surface. This is not surprising since the intensity of its peak in the analysis mass spectra is often even more important than that of the peaks under m/z 100, usually extremely intense. The mappings thus reflects the intensities of ions in the mass spectra. Indeed, for mappings b) and e), the collectors are barely covered with $[V-C_7H_{14}O_2N]^+$ ions. This suggests once again that, even if they were landed intact upon transfer, they have more probability to be fragmented since they were impacted by an additional ion beam (in comparison to reference analyses). The same reasoning can be made for the c) and f) mappings in which the sum of the pseudomolecular ions intensities are depicted. For all mappings, even if a bit more tricky for the b) and c), the maximum intensities are located in the upper zones of the collectors (except for the sputtered spot) which shows that the material is transferred close to the target. The total count of the transferred material is a bit higher for the collector of Ar^+_{5000} transfer; respectively $1.7\times10^6, 5.5\times10^3, 1.2\times10^4, 3.4\times10^6, 1.3\times10^4$ and 2.3×10^4 for a, b, c, d, e and f. Actually, the amount of transferred material is proportional to the number of primary ions, *i.e.* the transfer ion dose, impinging the

target. This ion dose is itself directly dependent on the transfer time and the cluster ion beam current during transfer. Due to slight differences between the initial and final GCIB currents, the transfers were performed under different ion doses which induces some variability in the transferred amount. Since the total transfer ion doses were of 4.63×10^{14} and 4.61×10^{14} ions for the bombardment under Ar^+_{5000} and Ar^+_{3000} clusters respectively, the previous argument is quite unlikely. This also could be explained by less fragmentation due to less energy per atom in the Ar^+_{5000} clusters. Finally, the sum of the $[V+H]^+$ and $[V+Na]^+$ ions intensity is mostly represented by the second one reflecting the large quantity of sodium ions covering the collectors surfaces. This can be seen on Figure 3.21 which is the pseudomolecular ions zone in the mass spectra reconstructed from the entire mapping data of the Ar^+_{3000} transfer. The mappings of Na^+ can be found in the supplementary information in Figure 6.15.

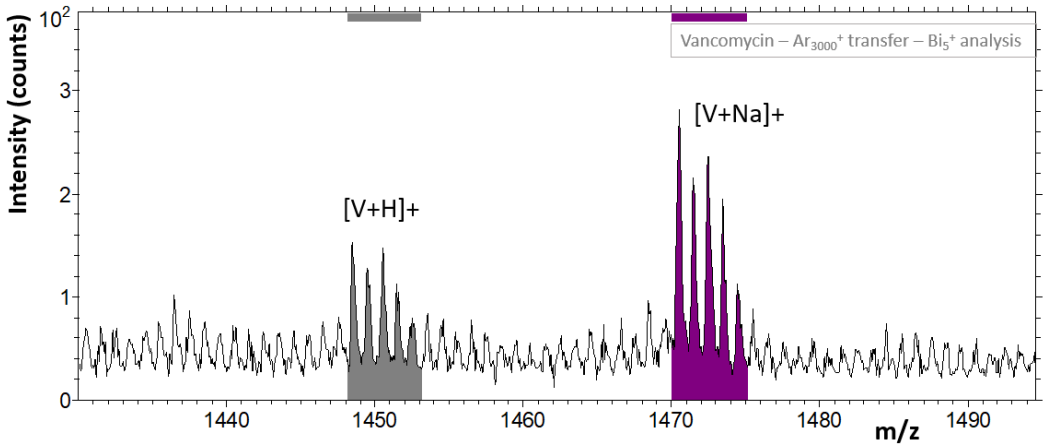

Figure 3.21: Spectrum of the vancomycin pseudomolecular ions $[V+H]^+$ and $[V+Na]^+$ reflecting the large amount of sodium ions on the collectors.

Overlay of the characteristic substrate ions (in red) and pseudomolecular ions of vancomycin (in green) show the distribution of these ions on the collectors (Figure 3.22). This shows once again that the sputtered material is mostly located on the top of these collectors (except for the bare substrate spot in a). There is however a difference in the sputter distance (shown by white curves) which is probably explained by higher E/n using Ar^+_{3000} cluster. Indeed, this energy is transferred to the species upon impacts ejecting them from the target. Differences in the impact energy could thus induce slight differences in the direction angles of the sputtered species. This distance difference is also affected the number of counts which varies between the experiments and by the exact impact point on the target.

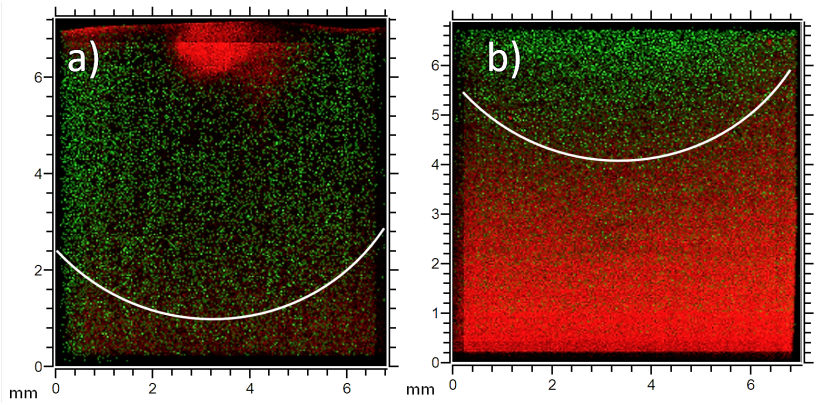

Figure 3.22: Overlay of the Ar^+_{3000} (a) and Ar^+_{5000} (b) transfers. The sum of Si^+ and $SiOH^+$ signals are in red while the sum of $[V+H]^+$ and $[V+Na]^+$ signals in green.

Finally, sputtering yield trends were plotted on the pseudomolecular, $C_6H_{14}N^+$ and $[V-C_7H_{14}O_2N]^+$ ions transferred from the targets onto collectors and can be seen in the following histograms respectively (Figures 3.23, 6.16 and 6.17).

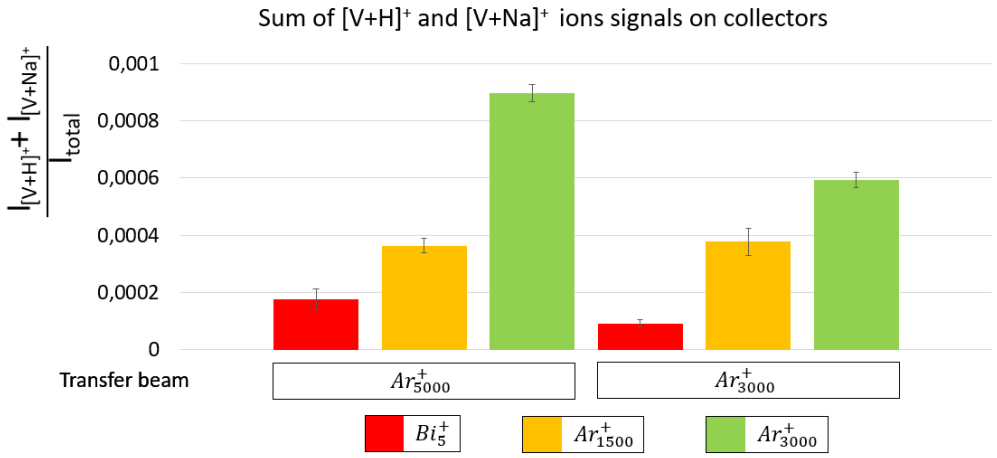

Figure 3.23: Histogram showing the $[V+H]^+$ and $[V+Na]^+$ pseudomolecular ions signals under the three usual analysis beams for both collectors of Ar^+_{3000} and Ar^+_{5000} transfers.

It can firstly be seen that Ar^+_{5000} transferred a larger amount of intact molecules on the collectors than Ar^+_{3000}, suggesting less fragmentation. This could also be due to slightly different ion doses during transfer. Of course, Ar^+_{5000} clusters, composed of more atoms, induce less fragmentation in the sample. Moreover, and for both collectors, the signal increases with the size of the clusters, confirming the decrease of fragmentation with the reduction of eV per atom. Exactly similar results are obtained for the $[C_6H_{14}N]^+$ and $[V-C_7H_{14}O_2N]^+$ fragment ions are are shown in the section 6.5.

Unfortunately, not a single dimer peak could be seen in the obtained mass spectra. The hypotheses to explain this observation are :

- Upon Ar cluster impacts, it is more than likely that a part of the dimers were

dissociated decreasing their proportion in comparison to the monomers. Thus, compared to the analyses, the transfers induce more fragmentation because of an additional cluster impact. Moreover, there is obviously less material deposited on the surface after transfer than with the two solution drying methods, especially for intact molecules and dimers. Indeed, the transferred material is composed of many sample fragments. All these combined factors seem to have for effect that, even if a small fraction of the initial dimers were landed intact, they cannot be detected after transfer.

- During landing, the part of dimers still intact after desorption, could have too much kinetic energy. This energy would then dissipate during the impact with the hard silicon collector by breaking, among perhaps other bonds, the non-covalent interactions linking the two vancomycin molecules. In the subsequent analysis, the dimers would therefore not be visible.

3.1.5 Summary on vancomycin systems

After discovering peaks that were not attributed by other studies in the past, investigations on particular fragments and vancomycin pseudomolecular ions was achieved. The evolution of these species versus the sample thicknesses and different ion beams were investigated. It was found that the sputtering of vancomycin fragments under Bi cluster ion beam followed the amount of deposited material with a maximum in larger thicknesses corresponding to the depth of penetration of these clusters. The sputtering under Ar-GCIB show a maximum in thin an thick layers for the smaller and the larger fragments respectively. This mirrors a confinement of the impact energy density caused by the hard silicon substrate. When the layers become thicker, the density of energy is lowered resulting in less covalent bond breaking in the vancomycin molecules. Thus, larger fragments are generated and sputtered. For the pseudomolecular ions, different influences between the sputtering under Bi-LMIG and Ar-GCIB are observed. Under Bi cluster, the $[V+H]^+$ and $[V+Na]^+$ emissions are more influenced by ionization mechanisms and seem to follow the emission of their respective cation adduct. The sputtering under Ar cluster, on the other hand, is more likely to follow the amount of deposited material and the size of the ejected species.

Then, the desorption of vancomycin+(Acetyl-L-Lys-)D-Ala-D-Ala non-covalent complexes was investigated under different analysis conditions. As they were firstly not visible in the spectra, ESI analyses were made to confirm their presence in the prepared complex solutions. Despite the certification of complexes presence by ESI, only the V+KAA complexes were able to be detected. The non-detection of V+AA complexes is possibly due to a difference of only one hydrogen bond (compared to V+KAA) allowing to determine a first limitation to the desorption of non-covalent complexes under the tested conditions. It could also be due to a "mass-missmatch" effect between

the molecules, ejecting the small AA by centrifugal effect in UHV. On the V+KAA complexes, some detection trends could be shown. It was found that the intensity of the complex relative to the sum of the intensities of the pseudomolecular ions increased with the ratio of the concentration of KAA to that of V. This is simply the result of Le Chatelier's law. In addition, a layer thickness effect between drop-cast and spin-coated solutions would explain why, for ultra-thin layers, Bi clusters would sputter more ions while for thicker ones, it would be Ar clusters.

Since vancomycin dimers, bound by hydrogen bonds, are also non-covalent complexes, a study of their desorption was also carried out under different conditions. It was also demonstrated that dimers were emitted by all primary sources. We found that the dimer proportion to the pseudomolecular ions was increasing with the thickness layer. This was explained by (i) Le Chatelier's law and (ii) uneven surface coverage distributions for thinner and thinner layers leading to a lower probability of sputtering dimers. Moreover, the intensities of dimer peaks over the total spectrum intensities showed different sputtering trends depending on the used ion beam. These trends were actually very similar to those of $[V+H]^+$ emission. This suggests that under Bi clusters, the dimer emission follows the emission of H^+ and that under Ar-GCIB, the sputtering is more influenced by the amount of deposited material and the size of the sputtered species.

Finally, some transfer experiments were carried out. Unfortunately, not a single complex could be subsequently detected on the collectors. This can be due to either dissociation at the landing impact, or to small dimer deposited quantities leading to less probability of sputtering, or even to a fragmentation induced by the additional ion beam impact upon analysis (subsequent to transfer). Nevertheless, some results could be obtained on particular fragments and on the intact pseudomolecular ions that were well found on the collectors. A final trend on the pseudomolecular ions intensities over the total spectra intensities showed that larger are the clusters, less they induce fragments, more they sputter, and this for both the transfer and analysis ion beams.

3.2 M(tfac)$_n$

In order to pursue the investigations on non-covalent complexes desorption and soft-landing, compounds based on metal-ligand (M-L) interactions, known to be more robust compared to the previous ones, are studied in this section. The metal trifluoroacetylacetonate complexes (referred to as M(tfac)$_n$), synthesized by chemistry students, were kindly provided by Pr. Sophie Hermans (SST/IMCN/MOST). First some reference analyses were achieved to (i) make sure these complexes could be analyzed (and so desorbed intact) by ToF-SIMS and (ii) to identify their mass spectral signature. These will then be transferred from a target onto a collector in the ToF-SIMS instrument following the same procedure as previously described.

3.2.1 References

With the intention of obtaining 20 g/L solutions, approximately 4 mg of the M(tfac)$_n$ powders were diluted into 200 µL of dichloromethane. However, for the samples that could not be totally dissolved in the solvent, only supernatants were collected. After their spin-coating on silicon wafers, the first analyses were carried out under 30 keV Bi_5^+ clusters in both positive and negative modes. As for the previous section, only some spectra will be shown. The other interesting ones are presented in the annexes section.

Four metal complexes were chosen for this study and are listed in Table 2.1 (see section 2) with their respective masses. To get a better view, the Table 3.3 shows the monoisotopic masses of each metal bound to one, two or three ligands respectively.

Table 3.3: Monoisotopic masses of the different metals bound to one, two or three ligands respectively.

	Cr	Ni	Co	Cu
1 tfac	204.96	210.95	211.94	215.95
2 tfac	357.97	363.97	364.96	368.96
3 tfac	510.99	516.98	517.98	521.98

Since Cu, Ni and Cr atoms have several stable isotopes, the distribution of the peaks of these complexes should follow that distribution as well as that of the carbon isotopes in lesser proportion. As cobalt only has one stable isotope, hence the Co complexes will only follow the carbon isotopic distribution. Figure 3.24 shows the four theoretical isotopic signatures of M(tfac)$_2$. Of course, every ion composed of one of these metals, should have the same isotopic distribution, even if the relative abundances could not

be exactly the same. Indeed, different amount of carbon atoms (and others in lesser extent) in the species will induce slight differences in the abundance of the isotopic distribution peaks.

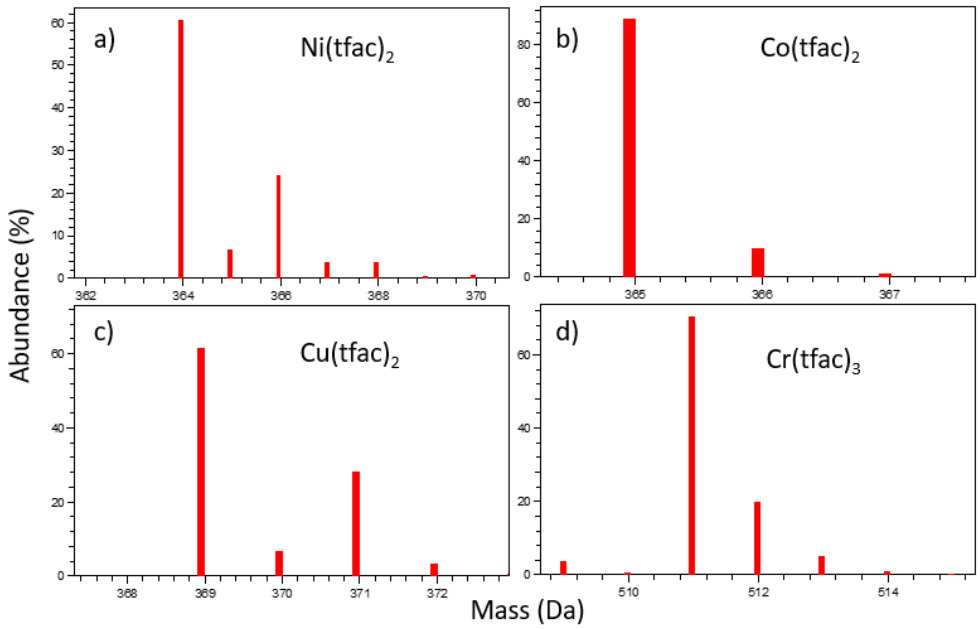

Figure 3.24: Theoretical isotopic distributions of $Ni(tfac)_2$, $Co(tfac)_2$, $Cu(tfac)_2$ and $Cr(tfac)_3$. Plotted from the IONTOF data processing program.

Before going any further, one must know that the mass spectra were in general very "dirty". Indeed, surely because of contamination and much fragmentation upon primary ion impacts, a lot of intense peaks were present. Figure 6.18 shows a complete mass spectrum of $Cr(tfac)_3$ which represents quite well all sets of mass spectra. Moreover, for $Ni(tfac)_2$, $Cu(tfac)_2$ and $Co(tfac)_2$, the ion peaks of the metal bound to one, two or three ligands were detected but with unexpected mass differences in comparison with their theoretical isotopic distributions. Indeed, for the positive mass spectra, these ions emerged with +3 Da differences. For negative mass spectra, the mass differences were varying between -2 and +3 Da. Some examples are shown in the supplementary information in Figure 6.20. Mass differences of ±1 Da, usually observed in SIMS spectra, correspond to proton adducts or removal, but it seems totally unlikely that two or three protons could have been adducted to or removed from the complexes. We were thus at the moment unable to identify the correct species corresponding to these peaks. For this reason, only the $Cr(tfac)_2$ sample, which allowed to analyze the different peaks at the right masses, will be discussed in this section.

First of all, the Figure 3.25 shows characteristic ions of the trifluoroacetylacetonate (tfac) ligand in a negative mass spectra of $Cr(tfac)_3$ obtained under 30 keV Bi_5^+ cluster ion beam. The peaks of F^-, CF_3^-, $[tfac\text{-}CH_3]^-$ ($C_4HO_2F_3^-$) and $tfac^-$ ($C_5H_4O_2F_3^-$) are visible at m/z 19, 69, 138 and 153 respectively. As the tfac ligand is negatively

charged, it could easily only be seen in the negative mode. The chromium atom was also easily seen in positive mode (Figure 6.19).

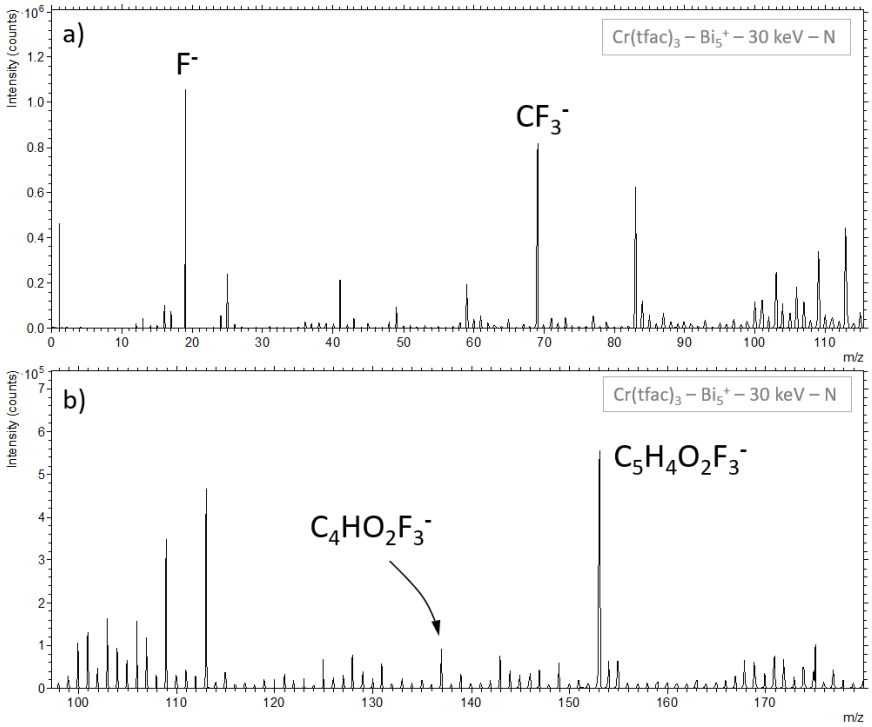

Figure 3.25: Negative mass spectrum of $Cr(tfac)_3$ from m/z 0 to 110 (a) and from m/z 100 to 180 (b) showing peaks of F^-, CF_3^-, $[tfac\text{-}CH_3]^-$ and $tfac^-$ at m/z 19, 69, 138 and 153 respectively. Obtained under 30 keV Bi_5^+ cluster ion beam.

Regarding the metal complexes, chromium bound to one and two ligands were easily seen in positive and negative modes while $Cr(tfac)_3$ was only visible in negative mode. Figure 3.26 shows the partial positive (a) and negative (b) mass spectra of $Cr(tfac)_2$ and $Cr(tfac)_3$ respectively. Figure 6.21 shows a partial positive mass spectrum of $Cr(tfac)_1$. All these mass spectra were obtained under 30 keV Bi_5^+ cluster ion beam. The rest of the mass spectra are not shown.

Firstly, these groups of peaks correspond to the isotopic signature of $Cr(tfac)_3$ shown in Figure 3.3d confirming the presence of a chromium atom in the ionic species. Secondly for $Cr(tfac)_1$ and $Cr(tfac)_2$ the monoisotopic peaks emerged at the exact m/z of 205 and 358 respectively while the one of $Cr(tfac)_3$ at a difference of -1 Da in comparison with is monoisotopic mass. This confirms that the complexes, composed of one, two and three ligands, can be successfully analyzed. The latter observation also suggests that, on the one hand, the native complexes, which are neutral species, must loose a proton in order to be charged and detected. On the other hand, fragments, which have lost negative ligand(s), are already charged and therefore do not require an adduct to be detected. The fact that $Cr(tfac)_3$ could not be detected in positive mode

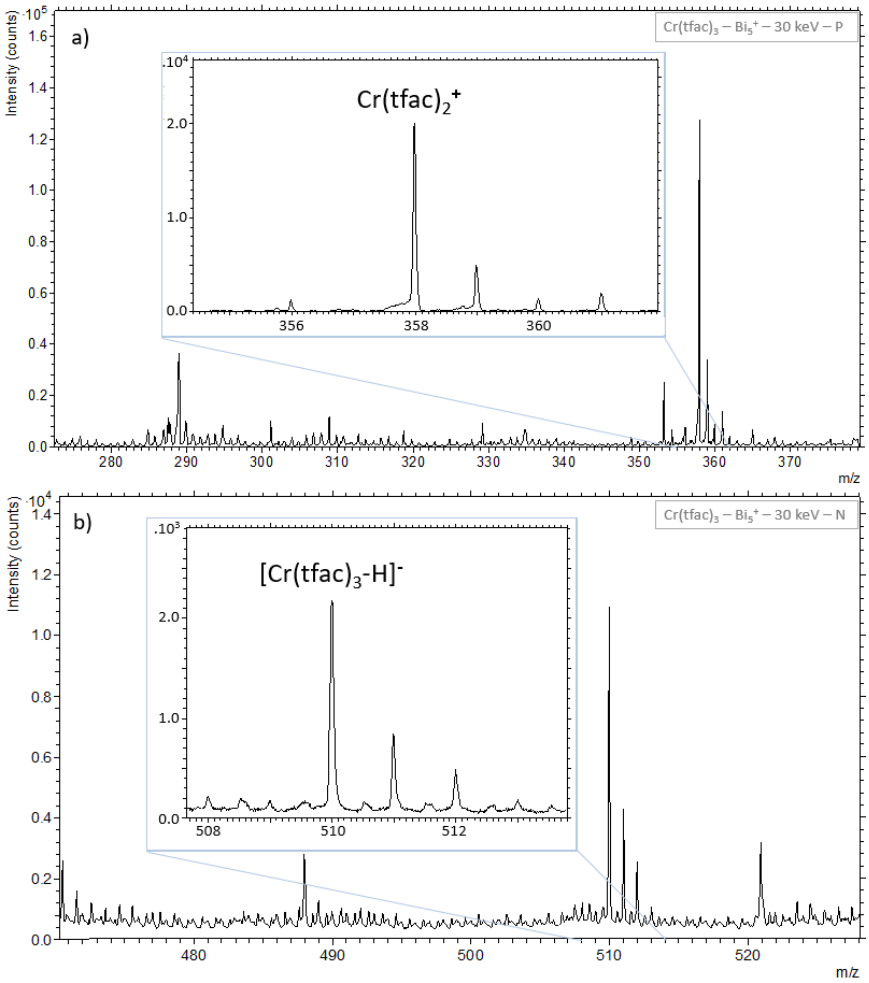

Figure 3.26: Positive (a) and negative (b) mass spectra of the $Cr(tfac)_3$ sample showing the groups of peaks of $Cr(tfac)_2^+$ and $[Cr(tfac)_3\text{-}H]^-$ respectively (monoisotopic peak at m/z 358 and 510). Obtained under 30 keV Bi_5^+ cluster ion beam.

is likely due to ionization mechanisms not allowing this species to be positively charged under these conditions. Finally, even if some of them have lost one or two tfac ligands, they still constitute non-covalent complexes since at least one tfac still remains bound to the metal with one or two M-L interactions. All these complex ions being detected confirm that the 6 keV energy per atom of the Bi_5^+ clusters allows the intact desorption of such species without breaking M-L coordination bonds.

In these spectra, as written above, many other intense groups of peaks were present. Four of them, having the isotopic signature of chromium, could be attributed to combinations of complexes with fragments. However, for the vast majority, it was yet not possible to assign them with a precise attribution. These ions are listed in Table 6.1 and will therefore not be part of discussion. In addition, some other ones had the distribution of two chromium atoms bound to organic compounds, suggesting that several complexes were detected together. Figure 6.22 shows ions with a monoisotopic peak at m/z 639 and the calculated isotopic distribution of $Cr_2(C_5H_4O_2F_3)_4$ (arbitrary chosen)

confirming that the species is surely composed of two fragmented complexes ions and probably other fragments. These peaks will not be discussed in this master thesis but may be of interest for future research on the *in situ* association of metal complexes in ToF-SIMS.

In order to compare the sputtering yields for different analysis conditions, other silicon wafers were spin-coated with the same $Cr(tfac)_3$ stock solution than previously and analyzed under 10 keV Ar^+_{1500} and Ar^+_{3000} cluster ion beams. With these conditions, the characteristic fragments were also seen in their respective mode of predilection, *i.e.* negative for $tfac^-$ characteristic ions and positive for Cr^+. The $Cr(tfac)^+_1$ peaks were visible in both positive and negative mode under both Ar cluster ion beams. The $Cr(tfac)^+_2$ ones emerged at the right m/z in positive mode, but were shifted by 2 Da towards lighter masses in the negative spectra. Finally, the $Cr(tfac)_3$ peaks were not visible in positive mode but in the negative spectra it seemed that small bumps were emerging. However these little peaks were too close to the background noise to be interpreted and discussed. Figure 6.23 shows the four partial positive (a & b) and negative (c & d) mass spectra of the species containing one (a & d) and two ligands ((b). The peak of the species presenting a 2 Da shift is shown in Figure 6.23d. For all measurements, the spectra calibration was relatively good and could not explain a shift in the detection of the latter species. As for the nickel, copper and cobalt trifluoroacetylacetonates, no good explanation for these unexpected observations were found yet. However, it is likely that different ionization effects/mechanisms when using Ar clusters instead of Bi clusters could have play a major role for the undetected $[Cr(tfac)_3\text{-}H]^-$ species. Moreover, some thickness effects that were not investigated could also have some role to play in this non-detection. For these speculative reasons, these species will not be represented in the following trends and will not be discussed. Thus the Bi^+_5 clusters beams seem to be the most appropriate analysis beam to use for the detection of these species.

A summary of the analysis conditions that allowed us to detect the different complex species can be found in Table 3.4.

Table 3.4: Summary of detection results according to the analysis conditions.

Mode	**Positive mode**			**Negative mode**		
Analysis beam	**Bi^+_5**	**Ar^+_{1500}**	**Ar^+_{3000}**	**Bi^+_5**	**Ar^+_{1500}**	**Ar^+_{3000}**
$Cr(tfac)_1$						
$Cr(tfac)_2$						
$Cr(tfac)_3$						

Legend				
	Success		Failure	
	Close to the noise		Mass shift	

Figure 3.27 shows the sputtering yield of the different species normalized to the total spectral sputtering yield. The bars on the left of the histogram correspond to the negative mode while those on the right to the positive mode. In negative mode, the only trend that can be observed is for $Cr(tfac)_1^-$ and shows an increase of the sputtering yield when using larger cluster ion beams. In positive mode, the same trend is observable for $Cr(tfac)_2^+$ and the exact opposite for the species containing one tfac ligand.

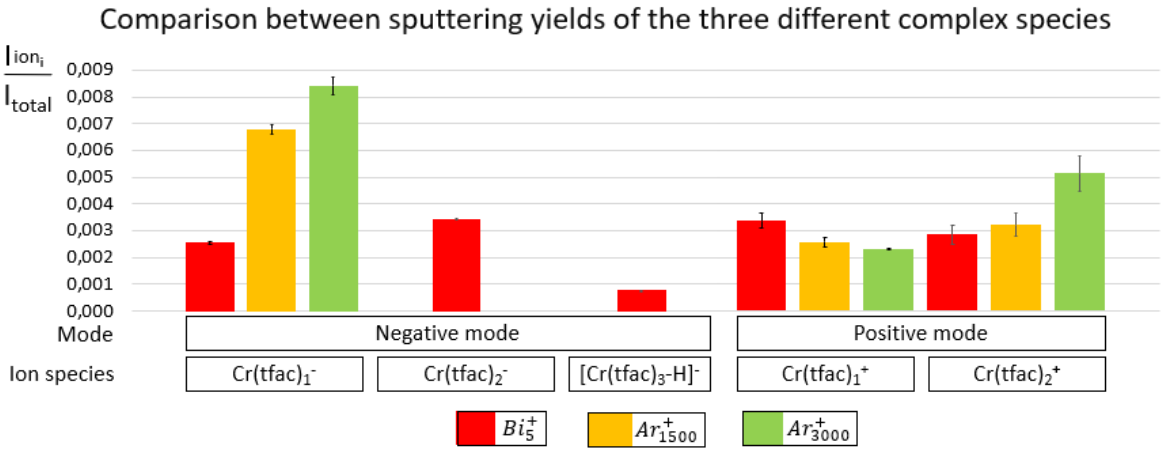

Figure 3.27: Comparison between the sputtering yields (normalized to the total sputtering yield) of the three complex forms in positive and negative modes and under three analysis beams.

In positive mode, this behavior could be explained by the decrease of energy per atom when using larger clusters. Since more $Cr(tfac)_2$ are sputtered when using larger clusters which induce less fragmentation, an opposite trend for $Cr(tfac)_1$ is expected. Indeed, the latter are more sputtered by smaller clusters inducing more fragmentation. When regarding the results induced by different cluster beams, the same reasoning can be applied. Indeed, the $Cr(tfac)_3$ may be not observable because of ionization mechanisms issues but it seems that, for the yellow and green trends, more complexes are sputtered with two ligands than with only one. This can once again be explained by the fragmentation extent. Since a low E/n induces less fragmentation, more larger fragments are observed than small ones. In the same vein, the Bi cluster ion beam tend to fragment more the complexes leading in a larger proportion of chromium atoms bound to only one ligand.

In negative mode, the only comparative explanations that could be made concern the red trend and the different analysis beams for $Cr(tfac)_1$. Indeed, the increase of the sputtering yield observed for this species could be explained by the decrease in the E/n when using larger clusters. The Ar_{3000}^+ clusters, tend to dissociate the last ligand and the metal atom in a lesser degree than the Ar_{1500}^+ or the Bi_5^+ clusters. The difference observed, in comparison with the positive mode could come from different

ionization mechanisms. Finally, the absence of trend (in red) when using Bi clusters in negative mode could come from, once again, ionization mechanisms differences between the different species but we do not prefer to go further into doubtful explanations.

Now that the relative soft desorption of these three chromium trifluoroacetylacetonate forms, has been demonstrated under different analysis conditions, their transfer under large Ar cluster ion beams can be investigated.

3.2.2 $Cr(tfac)_3$ transfers

For the same reasons explained in the previous section, *i.e.* the unattributed complex peaks emerging at unexpected mass to charge ratios in both positive and negative modes, this section will also be entirely dedicated to the transfer of the $Cr(tfac)_{1-2-3}$ complexes.

For the transfer experiments, twenty µL drops of the ±20 g/L $Cr(tfac)_3$ reference solution were deposited and dried one after the other on silicon targets. After that, transfer were carried out for 15 hours and 3 hours under Ar^+_{5000} and Ar^+_{3000} cluster bombardment respectively. Finally, the collectors were analyzed by the three ion beams and 2D images were obtained by scanning the whole surfaces using 30 Bi^+_5 beam.

The results obtained in positive mode showed that the $Cr(tfac)^+_1$ and $Cr(tfac)^+_2$ ions could be easily detected on the collectors. However, as for the analysis experiments, the positively charged $Cr(tfac)_3$ complexes could not be seen. In negative mode, the only detected complexes were the chromium bound with two tfac ligands. Unfortunately, their peak intensities were either too weak when Bi cluster beams were used, or, as previously for Ar clusters, shifted by 2 amu towards lighter masses. Figure 3.28 shows the mass spectrum of a collector obtained after transfer under Ar^+_{5000}. It can be seen that the peaks of $Cr(tfac)^+_1$ and $Cr(tfac)^+_2$ emerge at the same mass than in the reference mass spectra (see Figures 6.21 and 3.26a) and with the correct distribution (see Figure 3.24). This thus confirms that these peaks are attributed to the right ions. Some mass spectra obtained by analyzing collectors under Ar^+_{3000} and Ar^+_{1500} cluster beams after transfer under Ar^+_{3000} and Ar^+_{5000} GCIBs respectively can be seen in the supplementary information (Figures 6.24). 2D SIMS mappings of both collectors can also be seen in the annexes sections (Figures 6.25 and 6.26). These mappings will not be discussed as they show the same kind of results than the SIMS images obtained after the vancomycin transfers (see section 3.1.4).

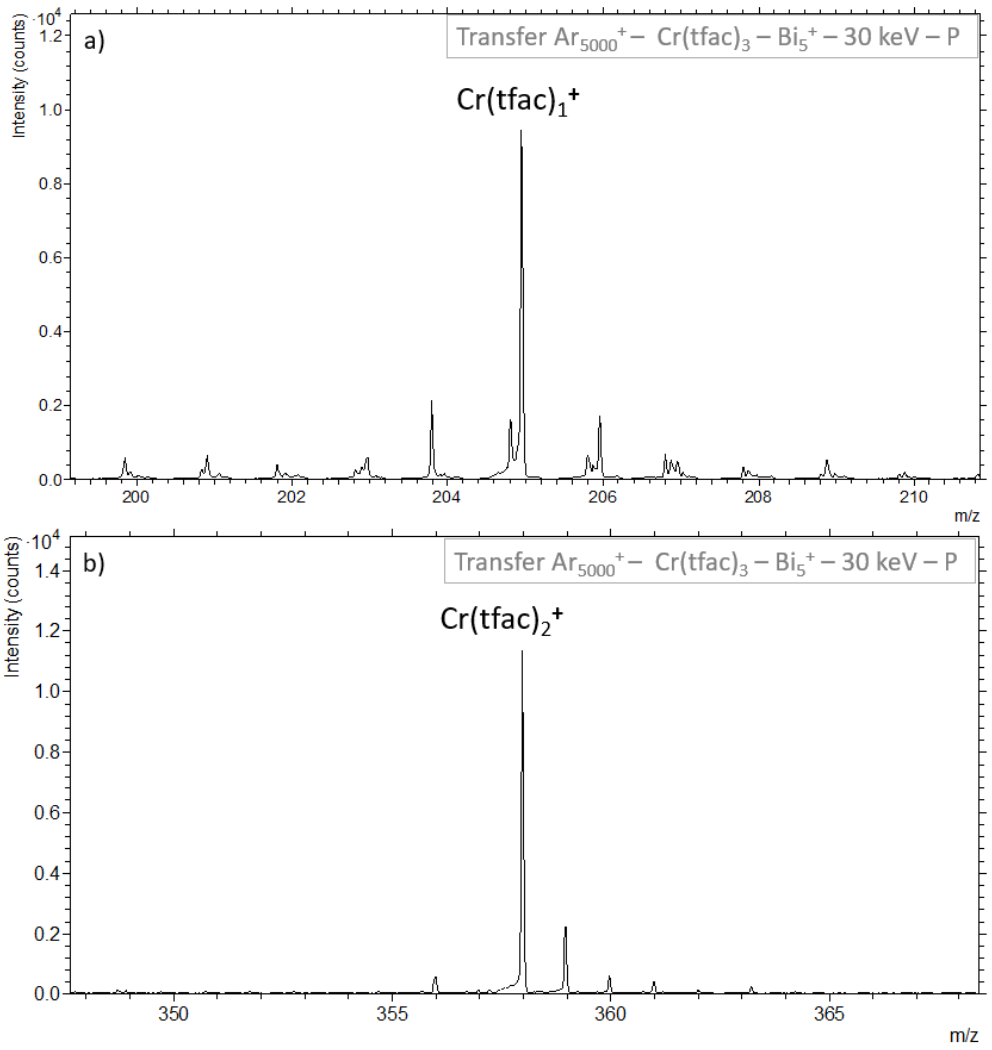

Figure 3.28: Positive mass spectra of the collectors after transfer under 10 keV Ar^+_{5000} of the $Cr(tfac)_3$ sample showing isotopic peaks of (a) $Cr(tfac)^+_1$ and (b) $Cr(tfac)^+_2$ (monoisotopic peak at m/z 205 and 358). Obtained under 30 keV Bi^+_5 cluster ion beam.

Table 3.5 shows a summary of the experiments results.

Table 3.5: Summary of transfer results according to the transfer and analysis conditions.

		Positive mode			Negative mode		
Transfer beams	**Complex**	$\mathbf{Bi^+_5}$	$\mathbf{Ar^+_{1500}}$	$\mathbf{Ar^+_{3000}}$	$\mathbf{Bi^+_5}$	$\mathbf{Ar^+_{1500}}$	$\mathbf{Ar^+_{3000}}$
$\mathbf{Ar^+_{3000}}$	$\mathbf{Cr(tfac)_1}$						
	$\mathbf{Cr(tfac)_2}$						
	$\mathbf{Cr(tfac)_3}$						
$\mathbf{Ar^+_{5000}}$	$\mathbf{Cr(tfac)_1}$						
	$\mathbf{Cr(tfac)_2}$						
	$\mathbf{Cr(tfac)_3}$						

Legend				
	Success		Failure	
	Close to the noise		Mass shift	

The patterns of colors in Table 3.5 being identical for both transfers could confirm the hypotheses made previously on different ionization mechanisms. However, with these results, interpretations can be only made on positive spectra and for the species containing one or two tfac ligands. Figure 3.29 shows a comparison between the selected ion intensities, normalized to the total intensity of the mass spectra, of the reference and the transfers for both detected ions and with different analysis conditions. It can firstly be seen that for both ions, the ion intensity seems to be higher after transfer than for the reference samples, especially after transfer under Ar^+_{5000} cluster ion beam. In addition, regarding to the particular samples, increasing trends are visible when using larger clusters except for the leftmost one. Finally, $Cr(tfac)^+_1$ intensities are higher than those of $Cr(tfac)^+_2$ for almost all sample and and analysis beams.

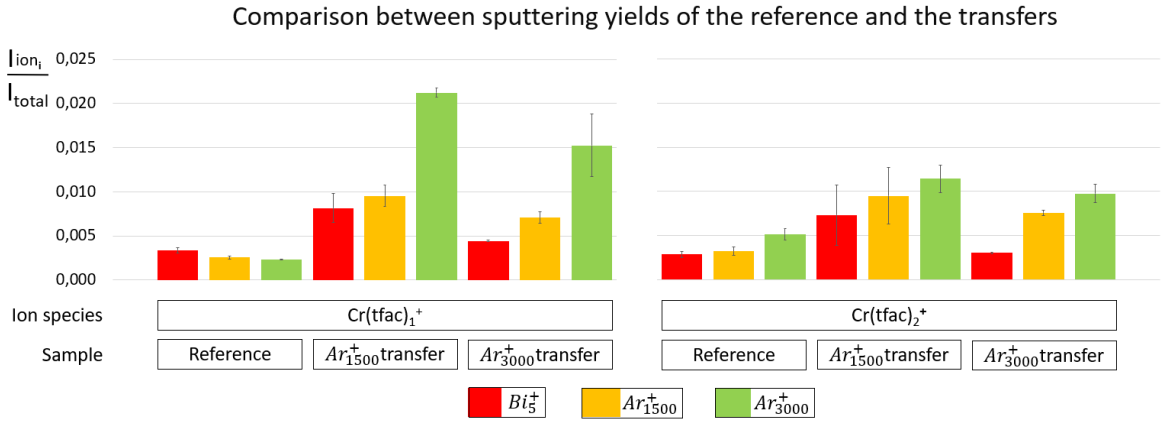

Figure 3.29: Comparison between the intensities (normalized to the total intensity) of two complex forms sputtered on collectors after Ar^+_{3000} and Ar^+_{5000} cluster ion beams in positive mode and under three analysis beams.

For both ions, the increasing trends when using larger cluster for both analyses the transfers are once more explained by the decreasing E/n. Indeed, larger clusters induce less fragmentation leading in more intact ions to be sputtered. For the transfer samples, the higher intensity for the complexes being emitted with one tfac ligand could be explained by the additional ion impact. This supplementary impact could thus induce a higher fragmentation probability leaving more complexes with only one fragment instead of two. However, this explanation would induce downwards trends for the $Cr(tfac)^+_2$ when using larger clusters, as it was seen for the reference sample but in the opposite direction (see section 3.2.1). The comparison between both references has already been discussed in the previous section. Finally, conclusions could not be drawn on the increasing intensities after the transfers compared to the references. These observations could come from differences in the deposited amount of complexes. After transfer, there is more than likely less material on the silicon surfaces than after spin-coating. With this very low quantity of deposited material, ionization mechanisms

could be changed leaving an enhanced probability of ionization. This probability may have increased due to the proximity to the substrate with which more interactions may occur. For instance, due to the metallic state of the silicon substrate, an electron could have been easier taken from the complex species leaving them positively charged.

3.2.3 Summary on M(tfac)$_n$ complexes

After realizing that the Ni(tfac)$_2$, Co(tfac)$_2$ and Cu(tfac)$_2$ samples could not be used as references because of unattributed mass shifts in their spectra, only the Cr(tfac)$_3$ one was investigated. Indeed, this sample allowed, firstly, the recognition of particular fragments in positive and negative mass spectra. Secondly, the "soft" desorption of Cr(tfac)$_3$ to form three types of complex ions, *i.e.* Cr(tfac)$_1^{\pm}$, the Cr(tfac)$_2^{\pm}$ and [Cr(tfac)$_3$-H]$^-$, was demonstrated under energetic Bi cluster ion beams. In addition, some other intense peaks, more than likely belonging to contamination, fragments and association of fragments, were visible in the mass spectra. Some of them, presenting identical isotopic signatures than the complexes, could be attributed. The same samples were then analyzed under Ar-GCIB and similar results were obtained except for the negative mode. Indeed, Cr(tfac)$_2$ complexes were shifted by an unexpected and yet unexplained mass of 2 Da when negatively charged. Finally, some trends were given and discussed. These allowed to demonstrate in positive mode that the ion yields were enhanced for Cr(tfac)$_2^+$ and decreased for Cr(tfac)$_1^+$ when using larger clusters as primary beams. In negative mode, the trends were more difficult to interpret and may be induced by different ionization mechanisms in comparison with the results obtained in positive mode.

After that the references were analyzed, the transfer of Cr(tfac)$_3$ complexes was investigated under Ar$_{3000}^+$ and Ar$_{5000}^+$ cluster ion beams. The results were only successful in positive mode, in line with the differences in the ionization processes previously hypothesized for the negatively charged sputtered ions. The negative species were thus not further discussed. Some spectra were then given to confirm the accuracy of the peak attribution. Finally, some trends on ion yields of both transferred intact complex fragments, *i.e.* Cr(tfac)$_1^+$ and Cr(tfac)$_2^+$, were given and discussed. The interpretations were the following ones :

1. For both ions, more complexes were sputtered using larger clusters confirming the lower fragmentation induced by the decreasing energy per atom ratio.

2. Higher ion yields for the complex containing one ligand than for the other one, was explained by the additional cluster impact. This impact would promote supplementary fragmentations leaving more species with only one tfac ligand.

3. After transfer, a lower amount of material is deposited on the surface in comparison with the spin-coating deposition method. The differences in thickness seem to

induce an enhanced ionization probability leading to a higher complex sputtering yield for the collectors than for the references.

4 Conclusion

The goal of this master thesis was to investigate the feasibility of intact non-covalent complexes desorption from a surface and their subsequent soft-landing on another one using time-of-flight ion mass spectrometry. Two systems, *i.e.* the vancomycin-ligand systems and metal trifluoroacetylacetones coordination complexes, linked by weak and strong non-covalent interactions respectively, were studied in this work.
For each system, the first step was to analyze the reference samples in different conditions in order to (i) make sure these complexes could be detected intact and (ii) identify their mass spectral signatures. After that transfer experiments were carried out and the collectors were analyzed using ToF-SIMS.

Vancomycin systems For reference samples it was found that the fragments sputtering followed different effects between Bi-LMIG and Ar-GCIB. Indeed, under Bi clusters bombardments, it depended on the amount of deposited material and had its maximum with thicker layers. Under Ar clusters bombardment, the fragments sputtering was more dependent on the energy per atom ratio and to fragmentation mechanisms. The emission of pseudomolecular vancomycin ions shows a maximum with thin layers for analyses under Bi clusters and with thick layers under Ar ones. It was shown that it rather depended on the ionization mechanisms under Bi cluster ion beams and seemed to follow the emission of their respective cation adduct. Under Ar-GCIB, on the other hand, the sputtering of such species depended more on the layer thickness and the fragmentation. For vancomycin non-covalent complexes, V+KAA complexes and vancomycin dimers could be desorbed intact under different analysis conditions. Unfortunately, V+AA was never detected probably because of fewer interactions or ejection upon centrifugal effects. The sputtering of V+KAA complexes was found to be dependent on layer thickness effects. Bi clusters ion beams tend to sputter more this species when bombarding thin layers while Ar-GCIB when thicker ones are involved. It was also found that the vancomycin dimers sputtering followed the one of $[V+H]^+$ complexes for both Bi and Ar clusters. Finally, the transfer experiments were inconclusive for both analyzed non-covalent complexes. This is probably due to a lower amount of material deposited on collectors and additional cluster impacts inducing a higher fragmentation probability. These complexes could also have been dissociated upon landing but in seemed less likely. Nevertheless, fragments and intact pseudomolecular ions could be transferred. It was confirmed that larger are the clusters, less they induce

fragmentation and higher the ion yields of large fragments and pseudomolecular ions are.

M(tfac)$_n$ complexes For the metal-ligand complexes, it was found that all Cr(tfac)$_n$ complexes could be analyzed under almost all conditions and that some of them could be detected on collectors after transfer. For Ni(tfac)$_2$, Co(tfac)$_2$ and Cu(tfac)$_2$ samples it was realized that they could not be used as references and for transfer. Indeed, these complexes emerged with unexpected mass shifts in their spectra. With the analysis experiments, the results showed that energetic Bi cluster ion beams could desorb fragments of Cr(tfac)$_3$, *i.e.* Cr(tfac)$_{1-2}$ in both positive and negative modes, and the [Cr(tfac)$_3$-H]$^-$ pseudomolecular ion in negative mode. Under Ar clusters, only the positive mode showed conclusive results. This can probably be explained by differences in the ionization mechanisms. Some positive mode trends demonstrated that the ion yields were enhanced for Cr(tfac)$_2^+$ and decreased for Cr(tfac)$_1^+$ when using larger clusters as primary beams inducing less fragmentation. After the transfer experiments, only Cr(tfac)$_{1-2}$ were successfully detected on the collectors and only in positive mode. The ion yields of these ions was found to be dependent to the E/n of the cluster. With larger cluster, less fragmentation is induced and thus higher fragments emission yields are observed. Higher ion yields for the Cr(tfac)$_1^+$ was explained by an additional impact inducing more fragmentation. Finally, layer thickness effects might explain why the ion yields for these species was higher than for references.

The final conclusion is that both weak and robust non-covalent complexes could be detected with time-of-flight secondary ion mass spectrometry confirming that sufficiently soft conditions can be achieved. For transfer only the more robust systems could be detected intact on the collectors. This suggests that two cluster ion beam impacts could be not favorable for weak interactions between two molecules to remain unbroken.

5 Perspectives

Some interesting perspectives can arise from the conclusions of this master thesis and are presented in this section. Some of those concern experiments that could have been done during the year and some others concern more future applications emerging from this work.

For both systems, other sources of primary ions might be interesting to investigate, either totally different from those used or different atom distributions for argon clusters. For instance, it has been shown that gas clusters made of H_2O cause different ionization mechanisms, significantly enhancing the yield of $[M+H]^+$ in comparison with Ar cluster of the same size or energy per atom. Molecular dynamics simulations showed sputtering enhancement of dimer emission with Ar_{500}^+ compared to smaller or larger Ar clusters for the same cluster energy (see Figure 6.27).

Vancomycin systems A first intriguing point would be to investigate the differences that could emerge from the additional hydrogen bond between vancomycin and the Acetyl-D-Ala-D-Ala ligand in comparison with the D-Ala-D-Ala one. Supplementary experiments could be carried out on vancomycin layer thicknesses. Indeed, more ellipsometric measurements could be achieved on thinner and thicker sample layer to have a better approximation of the thickness. Moreover, additional analyses on these layers could provide a better understanding of the ionization mechanisms and layer thickness effects on the vancomycin ion yields, *i.e.* fragments, pseudomolecular ions and dimers. Obviously, intense peaks that have not been attributed could be more investigated in order to know if they belong to contamination or vancomycin. For the transfer experiments, other methods could have been performed to verify the non-covalent complexes presence on collectors. For instance, the sputtered material could have been re-dissolved and analyzed under ESI-MS which is a softer analysis technique than ToF-SIMS. Other experiments could be investigated on the analysis and transfer of vancomycin-ligand systems frozen in a H_2O matrix to study the influence of water on the complex desorption and soft-landing. Finally, as the transfer has worked with intact vancomycin molecules, a future application could be the surface biofunctionalization of materials in order to provide them antibiotic functions, especially against *staphylococcus aureus*.

M(tfac)$_n$ complexes First of all, the observed shifts could be more investigated to determine their causes. All complexes could be freshly synthesized in order to firstly see if these shifts are still present and secondly if the peak forest belonged to contamination or fragmentation/association of complexes. Different layer thicknesses could have been prepared to investigate their effects on ionization probability and sputtering. Since isotopic signatures of species containing more than one chromium atom were observed, *in situ* complex association could be investigated in SIMS. Similar to the vancomycin transfers, other confirmation methods of complex deposition on collectors could have been tried. For example, since these complexes are colored, these could have been re-dissolved and their absorbance measured with spectrophotometry. Note that the amount of deposited complexes could possibly not reach the detection limit so longer transfers would be required. As the intact complexes were not detected on collectors, softer transfer conditions, such as 5 keV Ar^+_{5000} could be tested. Finally, even if not well understood yet, the metal presence is shown to enhance ionization probability and thus the ion yield of departing species in SIMS. As some Cr(tfac)$_3$ complex fragments were successfully transferred, their transfer could be investigated on the signal enhancement of other species.

A last thing to add could be the investigation on other non-covalent systems either linked by similar or different types of interactions. Indeed, with hydrogen bonds and metal-ligand coordination, only some extremes of the binding energy orders of magnitude were investigated. Other systems composed of similar interactions could be studied to confirm observations and conclusions. Some others, linked by aromatic or $\pi-\pi$ interactions could be studied to develop knowledge and understanding of the desorption and the soft-landing of non-covalent complexes using time-of-flight secondary mass spectrometry.

Bibliography

[1] H.-J. Butt, K. Graf, M. Kappl, *Physics and Chemistry of Interfaces.* John Wiley & Sons, Chapter 1, 2013.

[2] H. Lüth, *Surfaces and Interfaces of Solid Materials.* Springer Science & Business Media, Chapter 1, 2013.

[3] F. MacRitchie, *Chemistry at Interfaces.* Elsevier, Chapter 1, 2012.

[4] A. W. Adamson, A. P. Gast, *Physical Chemistry of Surfaces*, 6th Edition, Jhon Whiley & Sons, Inc., Chapter 1, 1997.

[5] F.M. Fowkes, *ATTRACTIVE FORCES AT INTERFACES.* Ind. Eng. Chem. 56, 40–52, 1964.

[6] E.M.McCash, *Surface Chemistry.*, Oxford University Press, Oxford, New York, Chapter 1, 2001.

[7] F. Rouquerol, J. Rouquerol, K.S.W. Sing, G. Maurin, P. Llewellyn, 1 - Introduction, in: F. Rouquerol, J. Rouquerol, K.S.W. Sing, G. Maurin, P. Llewellyn (Eds.), *Adsorption by Powders and Porous Solids (Second Edition).* Academic Press, Oxford, Chapter 1, 2014.

[8] Wikipedia, *Surface science*, accessed 21/04/2021 on: `https://en.wikipedia.org/wiki/Surface_science`

[9] *The Williams Dictionary of Biomaterials*, Liverpool University Press, 1999.

[10] R. Dong, P.X. Ma, B. Guo, *Conductive biomaterials for muscle tissue engineering*, Biomaterials 229, 119584, 2020.

[11] B. Prieto-Simón, C. Saint & N. Voelcker, *Electrochemical Biosensors Featuring Oriented Antibody Immobilization via Electrografted and Self-Assembled Hydrazide Chemistry*, Anal. Chem. 86, 1422–1429, 2014.

[12] M.P. Thompson, I. Peñafiel, S.C. Cosgrove & N.J. Turner, *Biocatalysis Using Immobilized Enzymes in Continuous Flow for the Synthesis of Fine Chemicals* Org. Process Res. Dev. 23, 9–18, 2019.

[13] H.S. Nalwa, *Handbook of Surfaces and Interfaces of Materials: Biomolecules, biointerfaces, and applications*, Academic Press, Chapter 1, 2001.

[14] T. Horbett, J.L. Brash & W. Norde, *Proteins at Interfaces III State of the Art*, Oxford University Press, Chapter 1, 2013.

[15] W. Norde, *My voyage of discovery to proteins in flatland... and beyond*, Colloids Surfaces B: Biointerface 61, 1-9, 2008.

[16] A. vander Straeten, A. Bratek-Skicki, L. Germain, C. D'Haese, P. Eloy, C-A. Fustin, & C. Dupont-Gillain, *Protein–Polyelectrolyte Complexes to Improve the Biological Activity of Proteins in Layer-by-Layer Assemblies*, Nanoscale 9, 17186–17192, 2017.

[17] I. Jacquemart, E. Pamuła, V. M. De Cupere, P. G. Rouxhet & C. Dupont-Gillain. *Nanostructured collagen layers obtained by adsorption and drying*, Journal of Colloid and Interface Science 278, 63–70, 2004.

[18] G. Verbeck, W. Hoffmann & B. Walton, *Soft-landing preparative mass spectrometry*, Analyst 137, 4393-4407, 2012.

[19] G.E Johnson, D. Gunaratne & J. Laskin, *Soft- and reactive landing of ions onto surfaces: Concepts and applications* Mass Spectrometry Reviews 35, 439–479, 2016.

[20] S. Rauschenbach, M. Ternes, L. Harnau & K. Kern, *Mass Spectrometry as a Preparative Tool for the Surface Science of Large Molecules*, Annual Review of Analytical Chemistry 9, 473–498, 2016.

[21] G. Siuzdak, B. Bothner, M. Yeager, C. Brugidou, C.M. Fauquet, K. Hoey & C.-M. Change, *Mass spectrometry and viral analysis*, Chemistry & Biology 3, 45–48, 1996.

[22] Z. Ouyang, Z. Takáts, T.A. Blake, B. Gologan, A.J. Guymon, J.M. Wiseman, J.C. Oliver, V.J. Davisson & R.G. Cooks, *Preparing Protein Microarrays by Soft-Landing of Mass-Selected Ions* Science 301, 1351–1354. 2003.

[23] P. Wang & J. Laskin, *Helical Peptide Arrays on Self-Assembled Monolayer Surfaces through Soft and Reactive Landing of Mass-Selected Ions*, Angewandte Chemie International Edition 47, 6678–6680, 2008.

[24] Z. Deng, N. Thontasen, N. Malinowski, G. Rinke, L. Harnau, S. Rauschenbach & K. Kern, *A Close Look at Proteins: Submolecular Resolution of Two- and Three-Dimensionally Folded Cytochrome c at Surfaces*, Nano Lett. 12, 2452–2458, 2012.

[25] J. Rajawat & G. Jhingan, *Chapter 1 - Mass spectroscopy* in: G. Misra (Ed.), *Data Processing Handbook for Complex Biological Data Sources* Academic Press, pp. 1–20. 2019.

[26] Wikipedia, *Electrospray ionization*, accessed 30/06/2021 on : https://en.wikipedia.org/wiki/Electrospray_ionization

[27] J.C. Vickerman & D. Briggs, *ToF-SIMS: material analysis by mass spectrometry 2nd edition*, IM publication LLP & SurfaceSpectra Limited, 2013.

[28] C. Cushman, J. Zakel, L.S. Fisher, J. Banerjee, B.M. Lunt, N.J. Smith & M.R Lindford, *Sample Charging in ToF-SIMS: How it Affects the Data that are Collected and How to Reduce it*, Vacuum Technology & Coating, 2018.

[29] S. Van Nuffel, *Three-dimensional time-of-flight secondary ion mass spectrometry imaging of primary neuronal cell cultures*, 2017.

[30] Mass spectrometry facility of Bristol university, *Time-of-Flight (TOF) Analysis*, accessed 07/07/2021 on: http://www.chm.bris.ac.uk/ms/tof.xhtml

[31] V. Thiel & P. Sjövall, , *CHAPTER 5 : Time-of-Flight Secondary Ion Mass Spectrometry (TOF-SIMS): Principles and Practice in the Biogeosciences* in: *Principles and Practice of Analytical Techniques in Geosciences*. 122–170, 2014.

[32] A. Brown & J.C. Vickerman, *Static SIMS for applied surface analysis*, Surface and Interface Analysis 6, 1–14, 1984.

[33] C.M. Mahoney & G. Gillen, *An Introduction to Cluster Secondary Ion Mass Spectrometry (Cluster SIMS)* in *Cluster secondary ion mass spectrometry: principles and applications 2nd Edition*, John Wiley & Sons, 1-11, 2013.

[34] P. Agüi-Gonzalez, S. Jähne & N.T.N. Phan, *SIMS imaging in neurobiology and cell biology*, J. Anal. At. Spectrom. 34, 1355–1368, 2019.

[35] IONTOF, *TOF-SIMS Technique*, accessed 14/07/2021 on: https://www.iontof.com/tof-sims-secondary-ion-mass-spectrometry-leis-\ technique-low-energy-ion-scattering.html

[36] J.S. Fletcher, S. Rabbani, A. Henderson, N.P. Lockyer & J.C. Vickerman, , *Three-dimensional mass spectral imaging of HeLa-M cells – sample preparation, data interpretation and visualisation*, Rapid Communications in Mass Spectrometry 25, 925–932, 2011.

[37] C.M. Mahoney, *Cluster secondary ion mass spectrometry of polymers and related materials*, Mass Spectrometry Reviews 29, 247–293, 2010

[38] A. Delcorte, O.A. Restrepo & B. Czerwinski, *Cluster SIMS of Organic Materials: Theoretical Insights* in: *Cluster Secondary Ion Mass Spectrometry* John Wiley & Sons, 13–55, 2013.

[39] P. Sigmund & C. Claussen, *Sputtering from elastic-collision spikes in heavy-ion-bombarded metals*, Journal of Applied Physics 52, 990–993, 1981.

[40] A. Delcorte, Ch. Leblanc, C. Poleunis & K. Hamraoui, *Computer Simulations of the Sputtering of Metallic, Organic, and Metal–Organic Surfaces with Bin and C60 Projectiles*, J. Phys. Chem. C 117, 2740–2752, 2013.

[41] L.W. Swanson, *Liquid metal ion sources: Mechanism and applications*, Nuclear Instruments and Methods in Physics Research 218, 347–353, 1983.

[42] N. Winograd, *Gas Cluster Ion Beams for Secondary Ion Mass Spectrometry*, Annual Review of Analytical Chemistry 11, 29–48, 2018.

[43] M. Lorenz, A.G. Shard, J.D.P. Counsell, S. Hutton & I.S. Gilmore, *Angular Distribution of Molecules Sputtered by Gas Cluster Ion Beams and Implications for Secondary Neutral Mass Spectrometry* J. Phys. Chem. C 120, 25317–25327, 2016.

[44] V. Delmez, H. Degand, C. Poleunis, K. Moshkunov, M. Chundak, C. Dupont-Gillain & A. Delcorte, *Deposition of Intact and Active Proteins In Vacuo Using Large Argon Cluster Ion Beams* J. Phys. Chem. Lett. 12, 952–957, 2021.

[45] H. Lodish, A. Berk, S.L. Zipursky, P. Matsudaira, D. Baltimore & J. Darnell, *Molecular Cell Biology*, 4th edition, 2000.

[46] *Strengths of Ionic and Covalent Bonds*, Chemistry LibreTexts, accessed 17/07/21 on:
https://chem.libretexts.org/Bookshelves/General_Chemistry/Book%3A_Chemistry_-_Atoms_First_(OpenSTAX)/04%3A_Chemical_Bonding_and_Molecular_Geometry/4.5%3A_Strengths_of_Ionic_and_Covalent_Bonds

[47] R.H. French, *Origins and Applications of London Dispersion Forces and Hamaker Constants in Ceramics*, Journal of the American Ceramic Society 83, 2117–2146, 2000.

[48] S.N. Eğe, *Organic chemistry: structure and reactivity, 5th ed*, ed. Houghton Mifflin Co, Boston, 2004.

[49] A.D. Buckingham, J.E. Del Bene & S.A.C. McDowell, *The hydrogen bond* Chemical Physics Letters 463, 1–10, 2008.

[50] Wikipedia, *Hydrogen bond*, accessed 17/07/21 on:
https://en.wikipedia.org/wiki/Hydrogen_bond

[51] E.V. Anslyn & D.A. Dougherty, *Modern Physical Organic Chemistry*, University Science Books, 2006.

[52] E.A. Meyer, R.K. Castellano & F. Diederich, *Interactions with Aromatic Rings in Chemical and Biological Recognition*, Angewandte Chemie International Edition 42, 1210–1250, 2003.

[53] D.R. Askeland & W.J. Wright, *The Science and Engineering of Materials*, Cengage Learning, 2015.

[54] *Intro to Coordination Chemistry* Chemistry LibreTexts, 2015, accessed 18/07/21 on:
https://chem.libretexts.org/Bookshelves/Inorganic_Chemistry/Supplemental_Modules_and_Websites_(Inorganic_Chemistry)/Coordination_Chemistry/Structure_and_Nomenclature_of_Coordination_Compounds/Intro_to_Coordination_Chemistry

[55] J.E. Huheey, E.A. Keiter, R.L. Keiter & G.B. Kaufman, *Inorganic chemistry: principles of structure and reactivity, 4th ed.*, J. Chem. Educ. 70, A279, 1993.

[56] N.T. Southall, K.A. Dill & A.D.J. Haymet,*A View of the Hydrophobic Effect*, J. Phys. Chem. B 106, 521–533, 2002.

[57] L.R. Pratt & D. Chandler, *Theory of the hydrophobic effect* J. Chem. Phys. 67, 3683–3704, 1977.

[58] A.J.R. Heck & T.J.D. Jørgensen, *Vancomycin in vacuo* International Journal of Mass Spectrometry, Special issue: In honour of Dudley H. Williams 236, 11–23, 2004.

[59] Y. Nitanai, T. Kikuchi, K. Kakoi, S., Hanamaki, I., Fujisawa & K. Aoki, *Crystal Structures of the Complexes between Vancomycin and Cell-Wall Precursor Analogs*, Journal of Molecular Biology 385, 1422–1432, 2009.
https://3dprint.nih.gov/discover/3dpx-008976

[60] G.J. Hughes, *"How it works" series: Vancomycin*, accessed 20/07/21 on:
http://www.hughesmedicine.com/2016/10/how-it-works-series-vancomycin.html

[61] T.J.D. Jørgensen, T. Staroske, P. Roepstorff, D.H. Williams & A.J.R. Heck, *bacterial receptor peptides identified by electrospray ionization mass spectrometry*, Journal of the Chemical Society, Perkin Transactions 2, 1859–1863, 1999.

[62] T.J.D. Jørgensen, P. Roepstorff & A.J.R. Heck, *Direct Determination of Solution Binding Constants for Noncovalent Complexes between Bacterial Cell Wall Peptide Analogues and Vancomycin Group Antibiotics by Electrospray Ionization Mass Spectrometry.* Anal. Chem. 70, 4427–4432, 1998.

[63] M. Schäfer, T.R. Schneider & G.M. Sheldrick, , *Crystal structure of vancomycin*, Structure 4, 1509–1515, 1996.

[64] L. Du, X. Yang, W. Li, H.Li, S. Feng, R. Zeng, B. Yu, L. Xiao, Y. Liu, M. Tu & H.-Y. Nie, *Time-of-flight secondary ion mass spectrometry analyses of vancomycin*, Biointerphases 13, 03B401, 2018.

[65] D. Shipp, B. Durham & R.C. Sadoski, *Metal Complexes of Trifluoropentanedione. An Experiment for the General Chemistry Laboratory.* J. Chem. Educ. 78, 665, 2001.

[66] Wikipedia, *Piranha solution*, accessed 24/07/21 on: https://en.wikipedia.org/wiki/Piranha_solution

[67] J.R. Vig, *UV/Ozone Cleaning of Surfaces*, Journal of Vacuum Science & Technology A: Vacuum, Surfaces, and Films 3, 1027–1034, 1985.

[68] Ossila,*Spin Coating: Complete Guide to Theory and Techniques*, accessed 26/07/2021 on: https://www.ossila.com/pages/spin-coating

[69] Z. Olumee, J.H. Callahan & A. Vertes, *Droplet Dynamics Changes in Electrostatic Sprays of Methanol-Water Mixtures*, J. Phys. Chem. A 102, 9154–9160, 1998.

[70] V. Cristaudo, C. Poleunis, P. Laha, P. Eloy, T. Hauffman, H. Terryn & A. Delcorte, *Ion yield enhancement at the organic/inorganic interface in SIMS analysis using Ar-GCIB.* Applied Surface Science 536, 147716, 2021.

[71] V. Cristaudo, C. Poleunis & A. Delcorte, *Effect of nanoconfinement on the sputter yield in ultrathin polymeric films: Experiments and model*, Applied Surface Science 444, 780–788, 2018.

[72] P.J. Vollmerhaus, E. Breukink & A.J.R. Heck, *Getting Closer to the Real Bacterial Cell Wall Target: Biomolecular Interactions of Water-Soluble Lipid II with Glycopeptide Antibiotics*, Chemistry – A European Journal 9, 1556–1565, 2003.

6 Annexes

6.1 Related to section 2

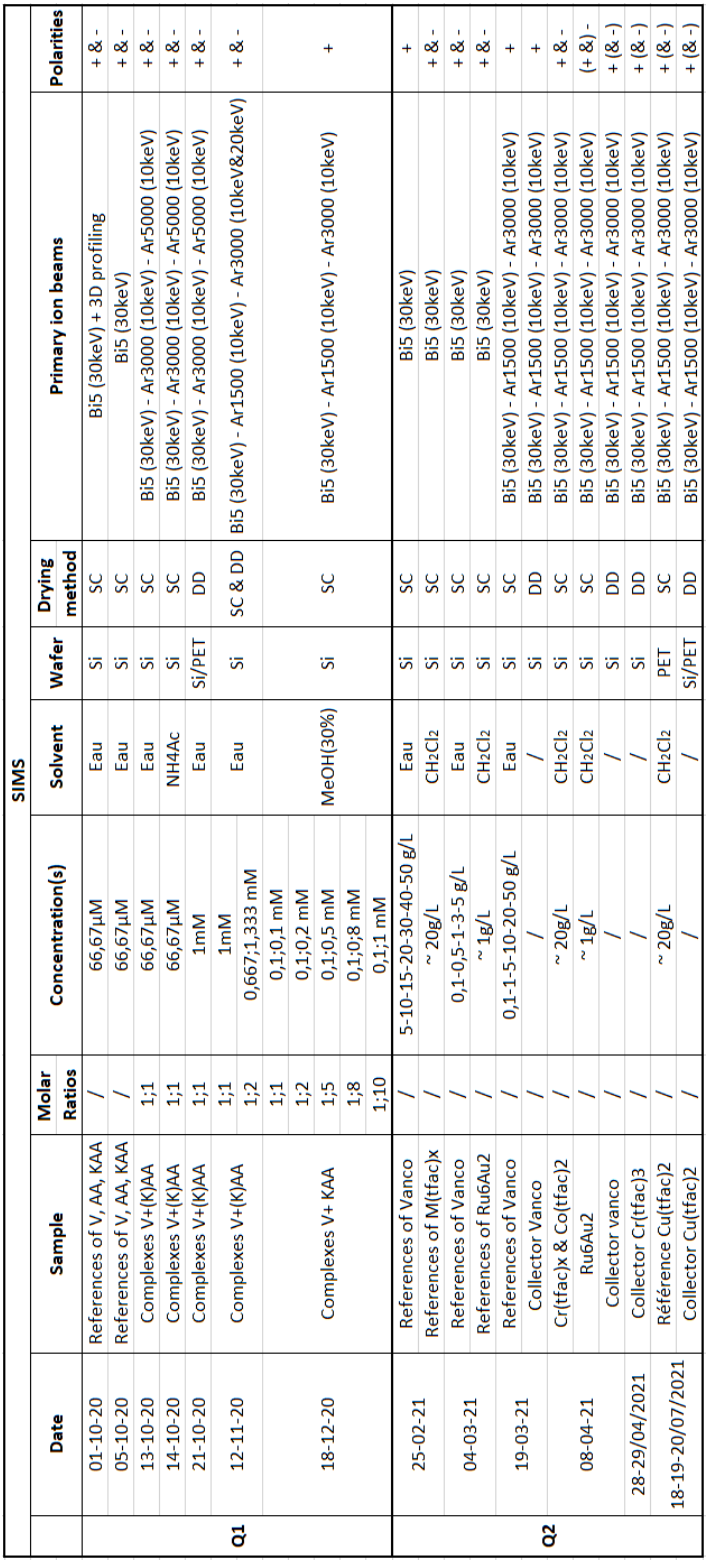

				SIMS					
	Date	Sample	Molar Ratios	Concentration(s)	Solvent	Wafer	Drying method	Primary ion beams	Polarities
Q1	01-10-20	References of V, AA, KAA	/	66,67µM	Eau	Si	SC	Bi5 (30keV) + 3D profiling	+ & -
	05-10-20	References of V, AA, KAA	/	66,67µM	Eau	Si	SC	Bi5 (30keV)	+ & -
	13-10-20	Complexes V+(K)AA	1;1	66,67µM	Eau	Si	SC	Bi5 (30keV) - Ar3000 (10keV) - Ar5000 (10keV)	+ & -
	14-10-20	Complexes V+(K)AA	1;1	66,67µM	NH4Ac	Si	SC	Bi5 (30keV) - Ar3000 (10keV) - Ar5000 (10keV)	+ & -
	21-10-20	Complexes V+(K)AA	1;1	1mM	Eau	Si/PET	DD	Bi5 (30keV) - Ar3000 (10keV) - Ar5000 (10keV)	+ & -
	12-11-20	Complexes V+(K)AA	1;1	1mM	Eau	Si	SC & DD	Bi5 (30keV) - Ar1500 (10keV) - Ar3000 (10keV&20keV)	+ & -
			1;2	0,667;1,333 mM					
	18-12-20	Complexes V+ KAA	1;1	0,1;0,1 mM	MeOH(30%)	Si	SC	Bi5 (30keV) - Ar1500 (10keV) - Ar3000 (10keV)	+
			1;2	0,1;0,2 mM					
			1;5	0,1;0,5 mM					
			1;8	0,1;0;8 mM					
			1;10	0,1;1 mM					
Q2	25-02-21	References of Vanco	/	5-10-15-20-30-40-50 g/L	Eau	Si	SC	Bi5 (30keV)	+
		References of M(tfac)x	/	~ 20g/L	CH_2Cl_2	Si	SC	Bi5 (30keV)	+ & -
	04-03-21	References of Vanco	/	0,1-0,5-1-3-5 g/L	Eau	Si	SC	Bi5 (30keV)	+ & -
		References of Ru6Au2	/	~ 1g/L	CH_2Cl_2	Si	SC	Bi5 (30keV)	+ & -
	19-03-21	References of Vanco	/	0,1-1-5-10-20-50 g/L	Eau	Si	SC	Bi5 (30keV) - Ar1500 (10keV) - Ar3000 (10keV)	+
		Collector Vanco	/	/	/	Si	DD	Bi5 (30keV) - Ar1500 (10keV) - Ar3000 (10keV)	+
	08-04-21	Cr(tfac)x & Co(tfac)2	/	~ 20g/L	CH_2Cl_2	Si	SC	Bi5 (30keV) - Ar1500 (10keV) - Ar3000 (10keV)	+ & -
		Ru6Au2	/	~ 1g/L	CH_2Cl_2	Si	SC	Bi5 (30keV) - Ar1500 (10keV) - Ar3000 (10keV)	(+ &) -
		Collector vanco	/	/	/	Si	DD	Bi5 (30keV) - Ar1500 (10keV) - Ar3000 (10keV)	+ (& -)
	28-29/04/2021	Collector Cr(tfac)3	/	/	/	Si	DD	Bi5 (30keV) - Ar1500 (10keV) - Ar3000 (10keV)	+ (& -)
	18-19-20/07/2021	Référence Cu(tfac)2	/	~ 20g/L	CH_2Cl_2	PET	SC	Bi5 (30keV) - Ar1500 (10keV) - Ar3000 (10keV)	+ (& -)
		Collector Cu(tfac)2	/	/	/	Si/PET	DD	Bi5 (30keV) - Ar1500 (10keV) - Ar3000 (10keV)	+ (& -)

Figure 6.1: Details of SIMS experiments done during the year.

ESI				
Date	**Sample**	**Molar ratios**	**Concentration(s)**	**Solvent**
14-10-20	Complexes V+(K)AA	1;1	~8µM	MeOH (30%V)
15-12-20	Complexes V+ KAA	1;1 - 1;2 - 1;5 - 1;8 - 1;10	0,1;0,1-0,2-0,5-0,8-1mM	MeOH (30%V)
	Références V et KAA	/	0,5mM	

Figure 6.2: Details of ESI experiments.

6.2 Related to section 3.1.1

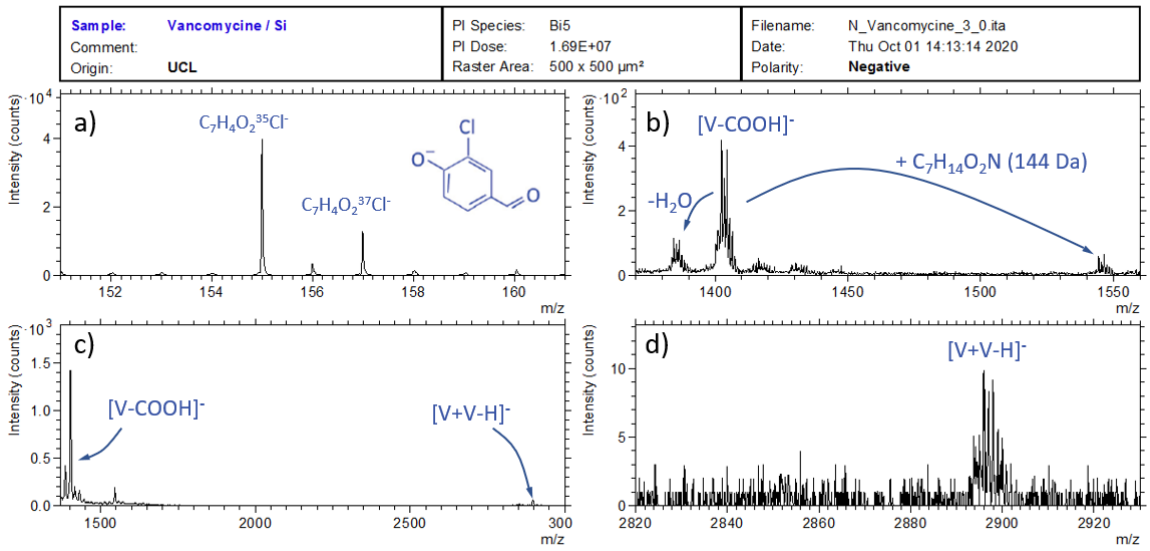

Figure 6.3: Negative mass spectra of characteristic fragment ions of vancomycin

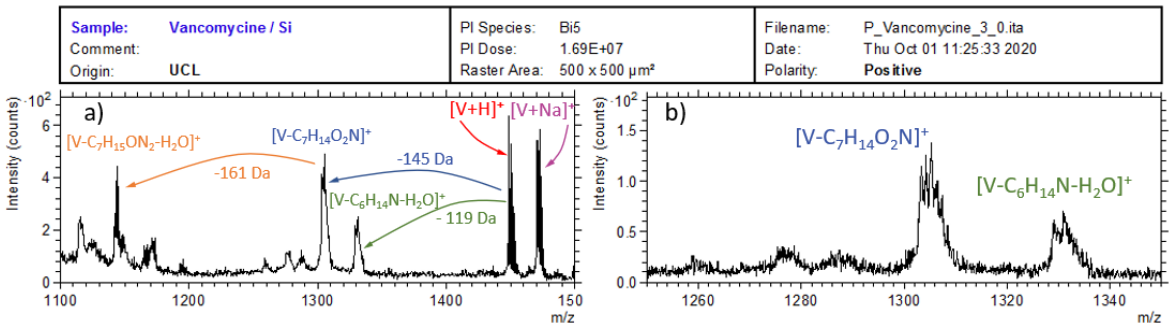

Figure 6.4: Positive mass spectra of the possible large vancomycin fragments. Assignments are hypothetical except for $[V\text{-}C_7H_{14}O_2N]^+$ which corresponds to a loss of a part of the vancosamine terminal group (144 Da).

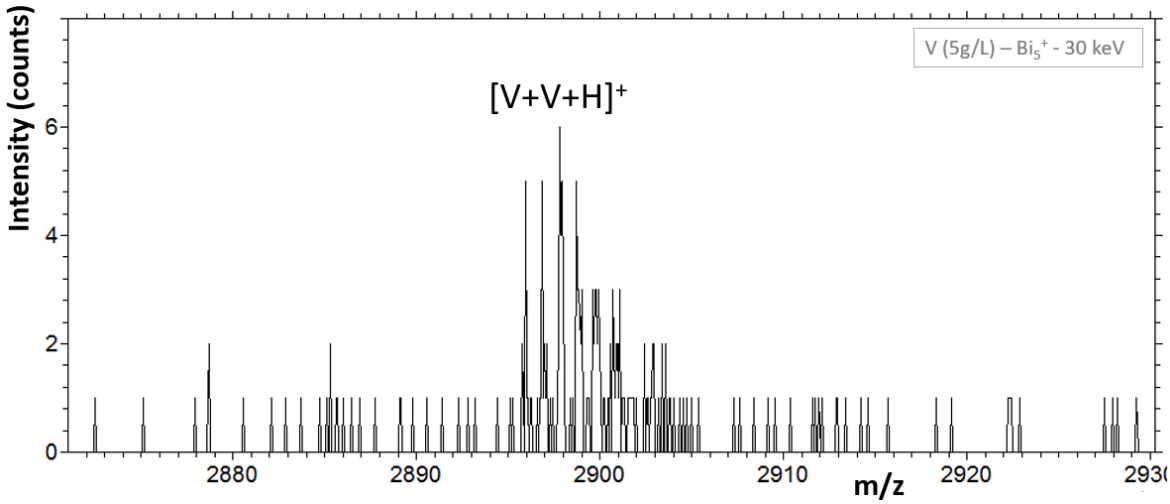

Figure 6.5: Positive mass spectrum showing the isotopic distribution of the vancomycin dimer. Monoisotopic peak at m/z 2895.87 corresponding to $C_{132}H_{151}Cl_4N_{18}O_{48} \equiv [V+V+H]^+$.

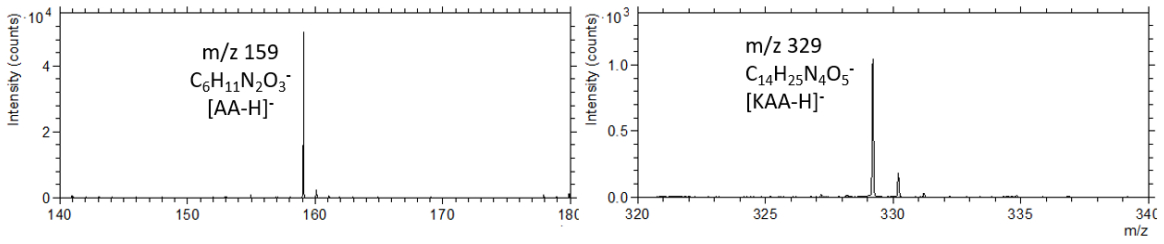

Figure 6.6: Negative mass spectra of AA (left) and KAA (right) showing the pseudomolecular peaks at m/z 159 and 329 respectively.

6.3 Related to section 3.1.2

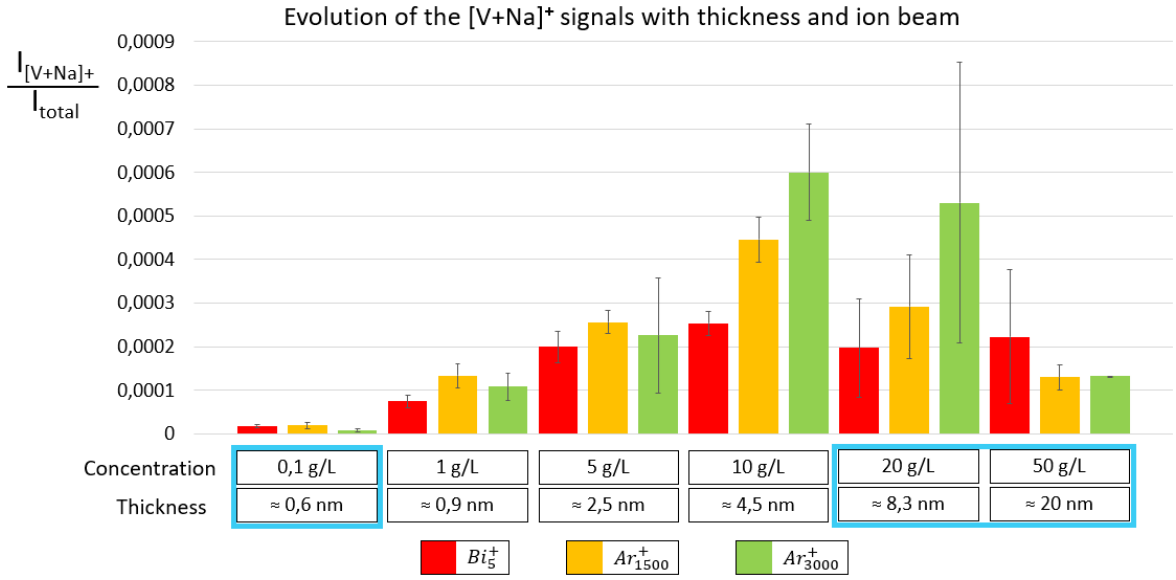

Figure 6.7: Histogram showing the $[V+Na]^+$ signals evolution with the vancomycin layer thickness and with different ion beams. The 0.1 to 50 g/L sample solutions were spin-coated and analyzed under Bi_5^+, Ar_{1500}^+ and Ar_{3000}^+ ion beams. The samples bordered in blue have to be taken carefully.

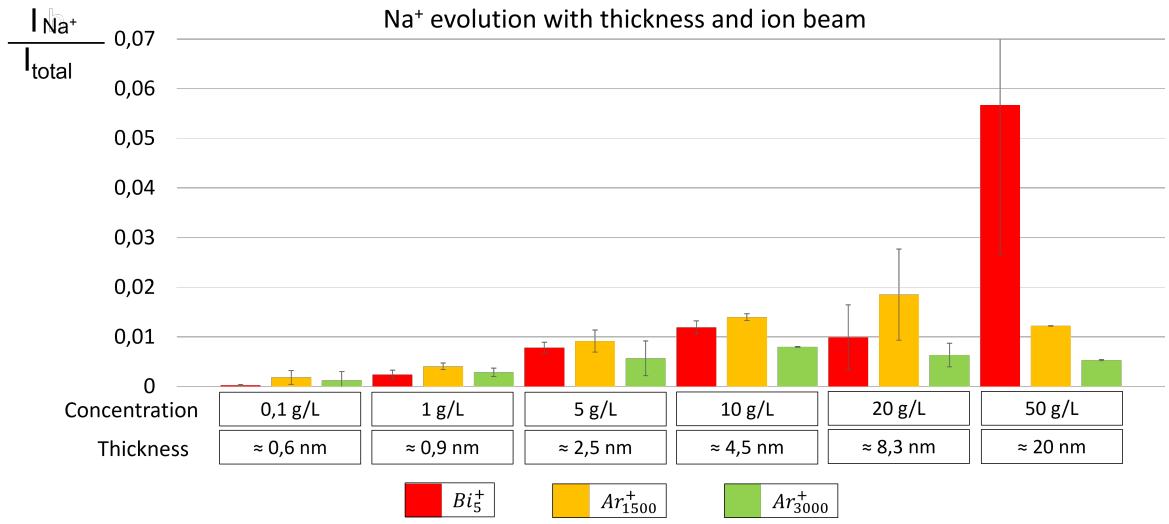

Figure 6.8: Histogram showing the sodium signals evolution with the vancomycin layer thickness and with different ion beams. The 0.1 to 50 g/L sample solutions were spin-coated and analyzed under Bi_5^+, Ar_{1500}^+ and Ar_{3000}^+ ion beams.

6.4 Related to section 3.1.3

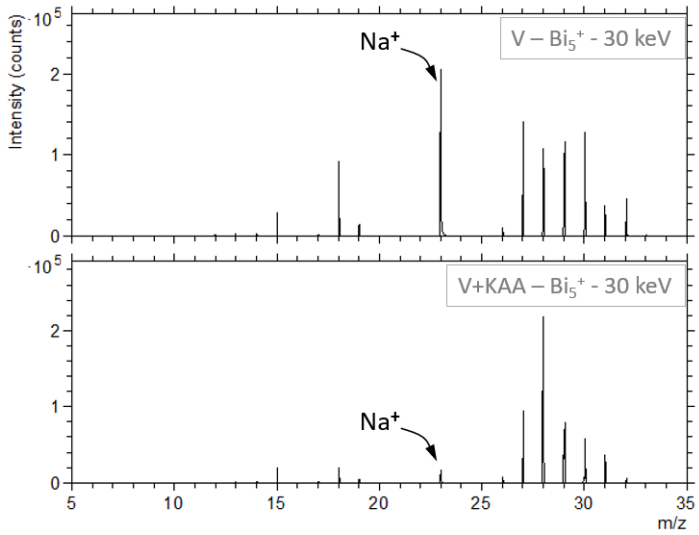

Figure 6.9: Sodium ion peaks on reference mass spectrum of V (up) and V+KAA (down) showing the Na-contamination

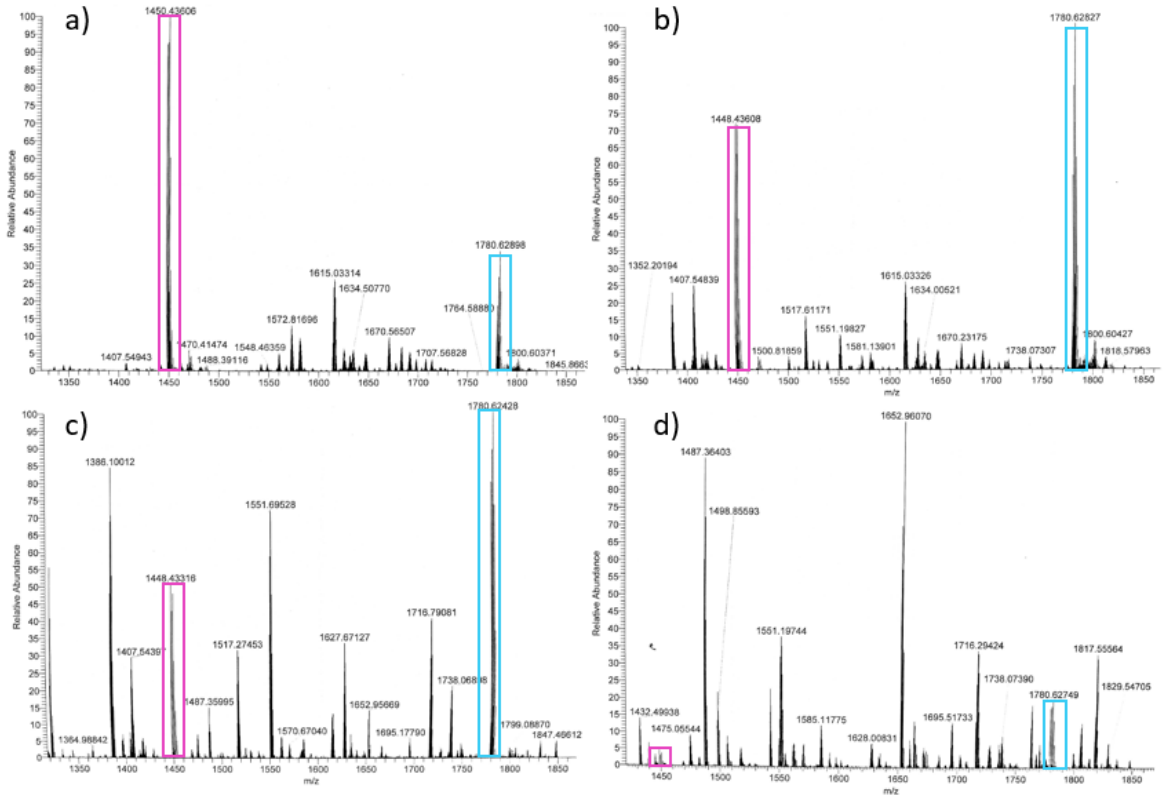

Figure 6.10: Positive ESI mass spectra showing that the KAA powder sample is contaminated. (a) 1:1, (b) 1:2, (c) 1:5 and (d) 1:8 V:KAA solutions. The peaks highlighted in pink are the $[V+H]^+$ pseudomolecular isotopic distribution while those highlighted in blue are th $[V+KAA]^+$ complexes.

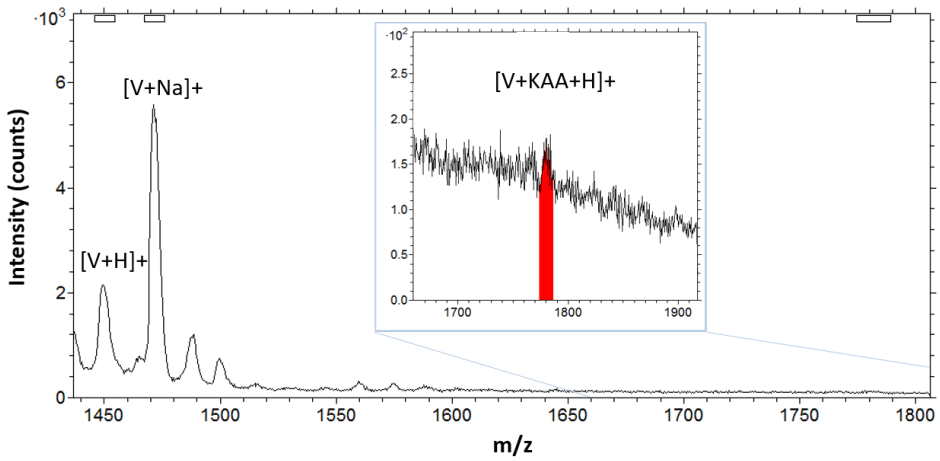

Figure 6.11: Positive mass spectrum showing the first visible V+KAA complex peak. Analysis beam : 10 keV Ar_3000^+.

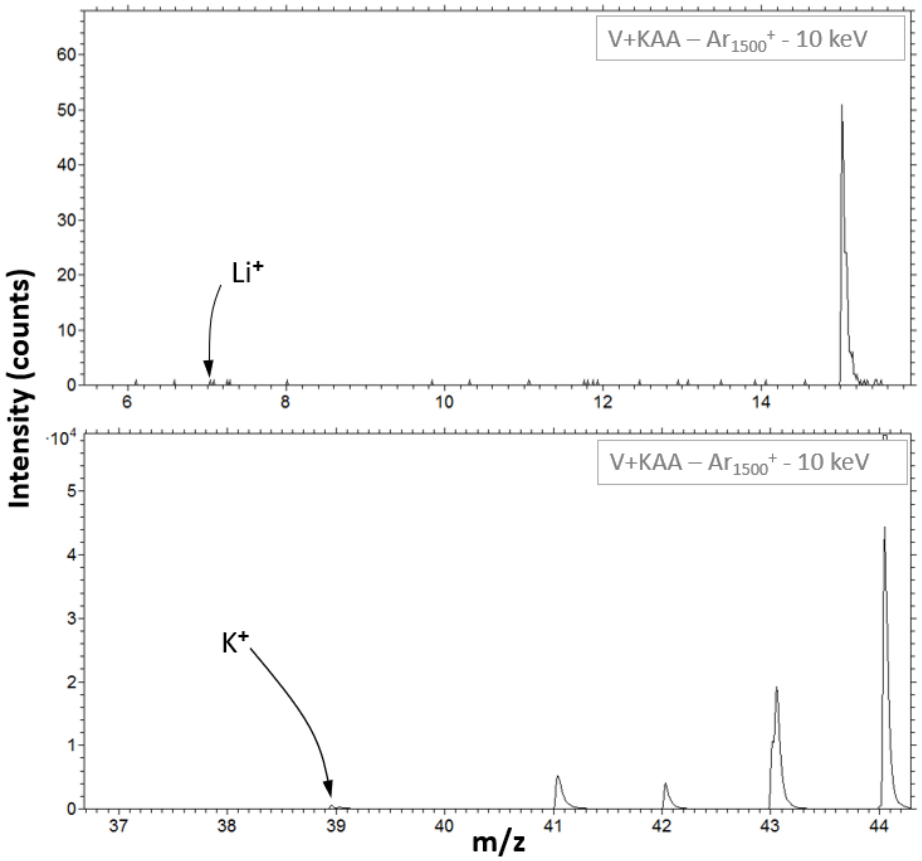

Figure 6.12: Positive mass spectra of V+KAA sample showing Li^+ K^+ peaks confirming that they could not provoke the additional peaks in Figure 3.12. Analysis beam : 10 keV Ar_1500^+.

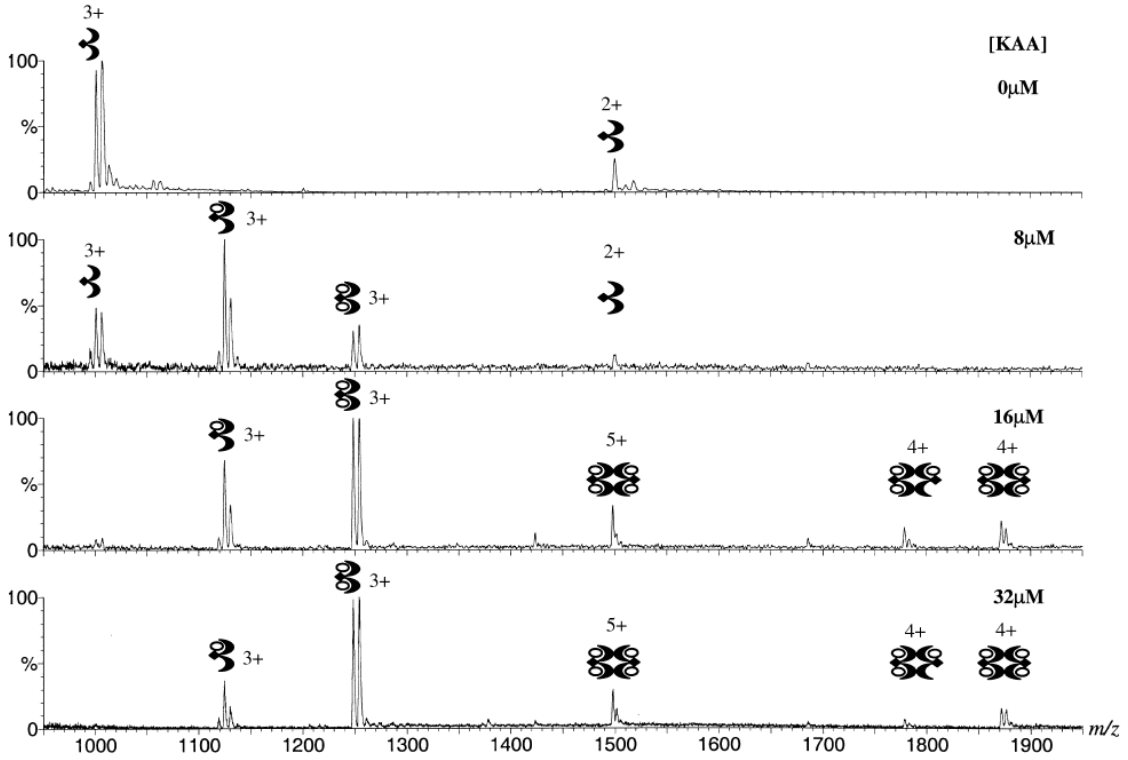

Figure 6.13: Positive ESI mass spectra showing different forms of vancomycin with its ligand, the black moon crossing representing vancomycin molecules and the white ellipses their KAA ligand. Taken from [72].

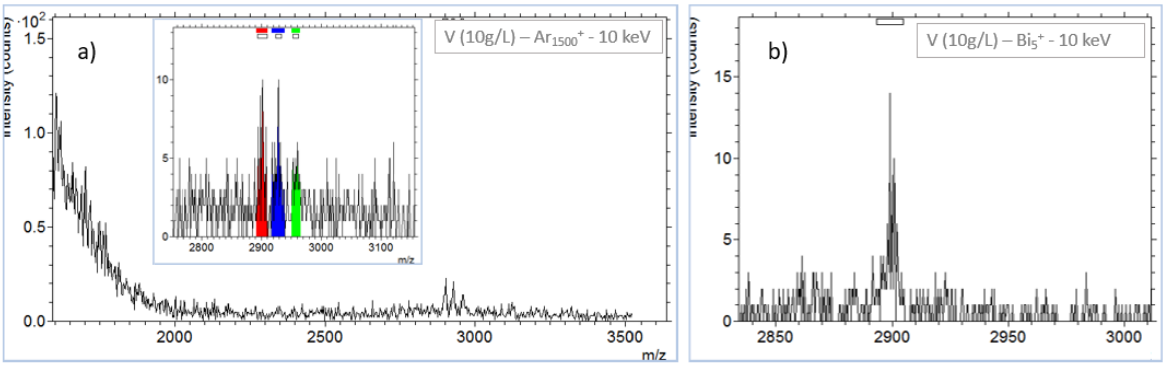

Figure 6.14: Spectra of the 10 g/L vancomycin sample analyzed by (a) Ar^+_{1500} (b) Bi^+_5 ion beams showing the vancomycin dimer region.

6.5 Related to section 3.1.4

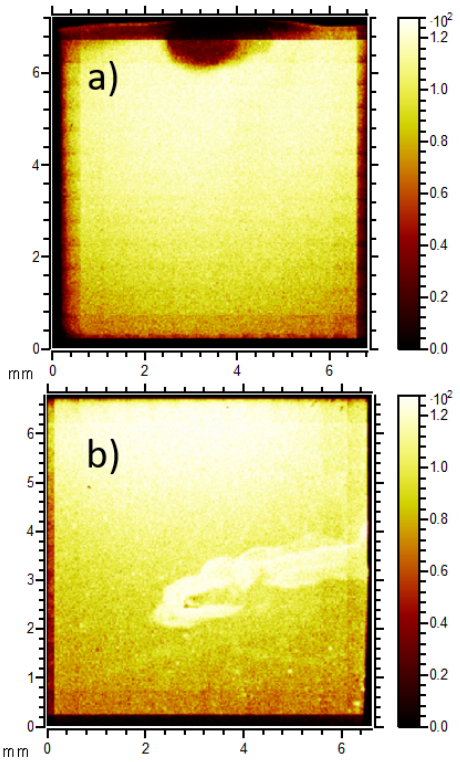

Figure 6.15: Chemical intensity images of Na^+ signal after Ar^+_{3000} (a) and Ar^+_{5000} (b) transfers.

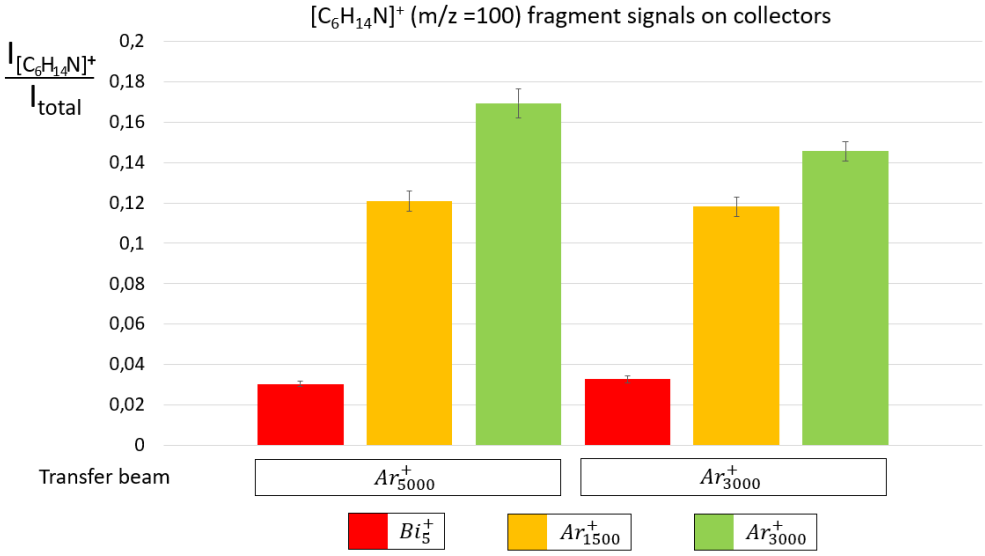

Figure 6.16: Histogram showing the $[C_6H_{14}N]^+$ fragment signals under the three usual analysis beams for both collectors of Ar^+_{3000} and Ar^+_{5000} transfers.

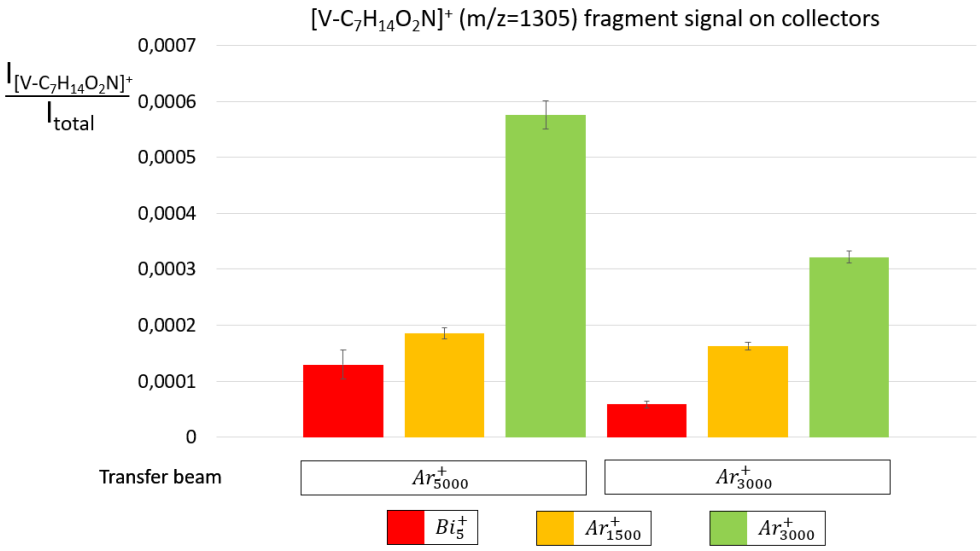

Figure 6.17: Histogram showing the $[V-C_7H_{14}O_2N]^+$ fragment signals under the three usual analysis beams for both collectors of Ar^+_{3000} and Ar^+_{5000} transfers.

6.6 Related to section 3.2.1

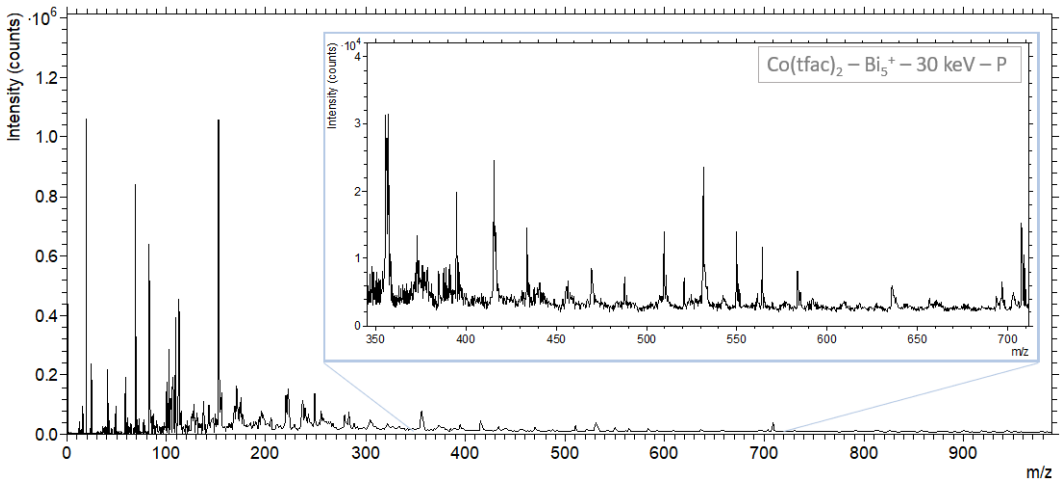

Figure 6.18: Positive mass spectrum of $Cr(tfac)_3$ showing the complexity of peak attribution of the $M(tfac)_n$ spectra.

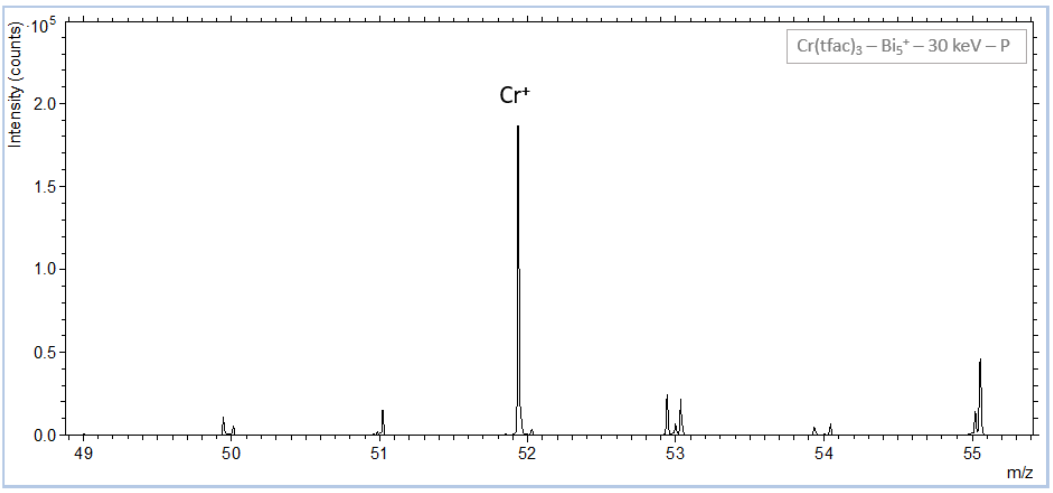

Figure 6.19: Positive mass spectrum of $Cr(tfac)_3$ obtained under 30 keV Bi^+ cluster ion beam showing the chromium cation peak at m/z 52.

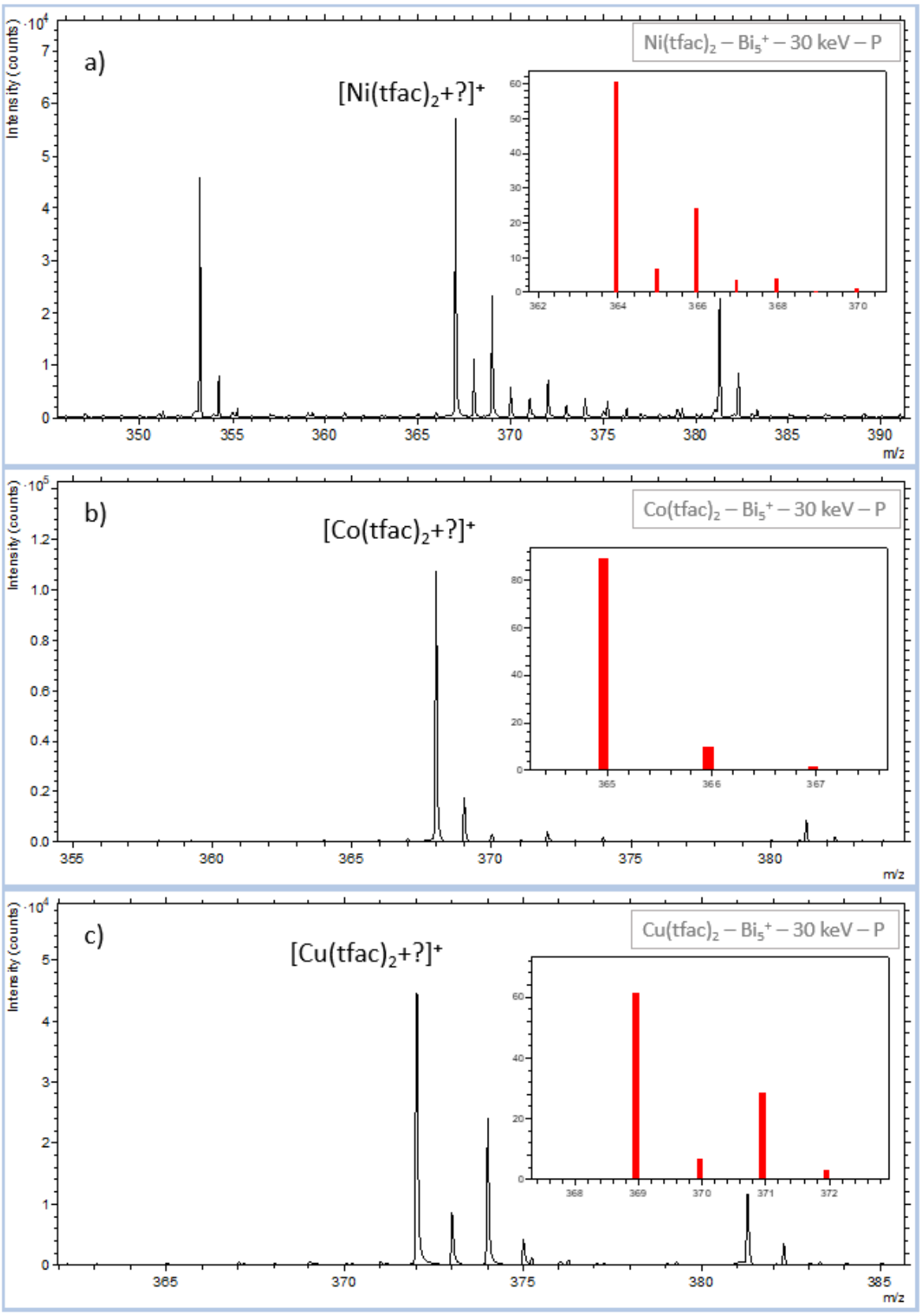

Figure 6.20: Positive mass spectra of (a) $Ni(tfac)_2$, (b) $Co(tfac)_2$ and (c) $Cu(tfac)_2$ and their respective isotopic distribution showing the complexity of peak attribution because of the +3 Da differences. All these spectra were obtained under 30 keV Bi^+ cluster ion beam in positive mode.

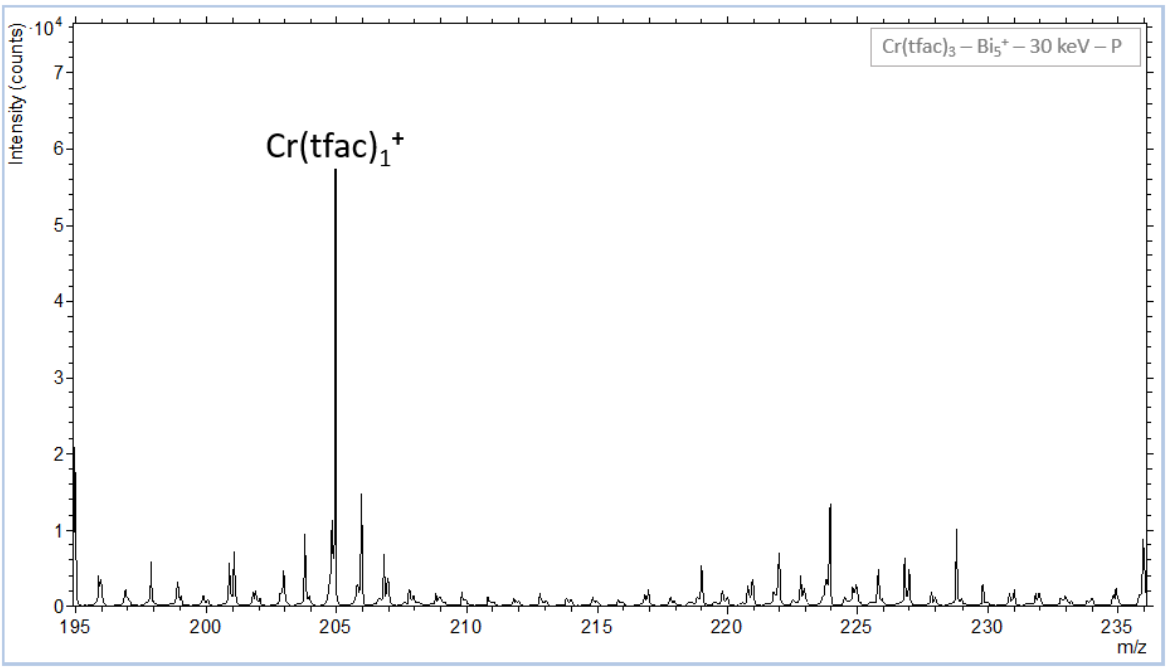

Figure 6.21: Positive mass spectrum of the $Cr(tfac)_3$ sample showing the groups of peaks of $Cr(tfac)_1^+$ (monoisotopic peak at m/z 205). Obtained under 30 keV Bi_5^+ cluster ion beam.

Table 6.1: Complexes associated with small fragments and their monoisotopic m/z.

Positive mode		**Negative mode**	
Ion	**m/z**	**Ion**	**m/z**
$[Cr(tfac)_1+F]^+$	224	$[Cr(tfac)_1+CH_3]^-$	220
$[Cr(tfac)_2\text{-}CF_3]^+$	289	$[Cr(tfac)_2+CH_3]^-$	373

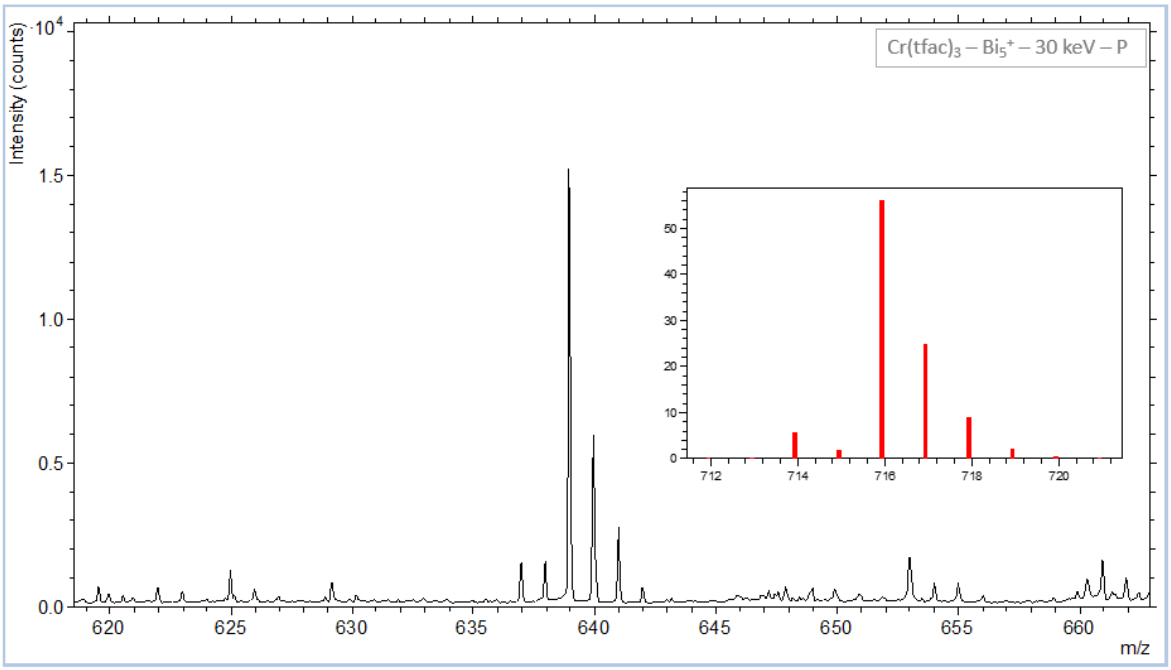

Figure 6.22: Positive mass spectrum of the $Cr(tfac)_3$ sample showing a group of peaks belonging to a species probably composed of two chromium atoms and organic compounds, probably fragments of ligands. In red, the isotopic distribution (monoisotopic peak at m/z 205). Obtained under 30 keV Bi_5^+ cluster ion beam.

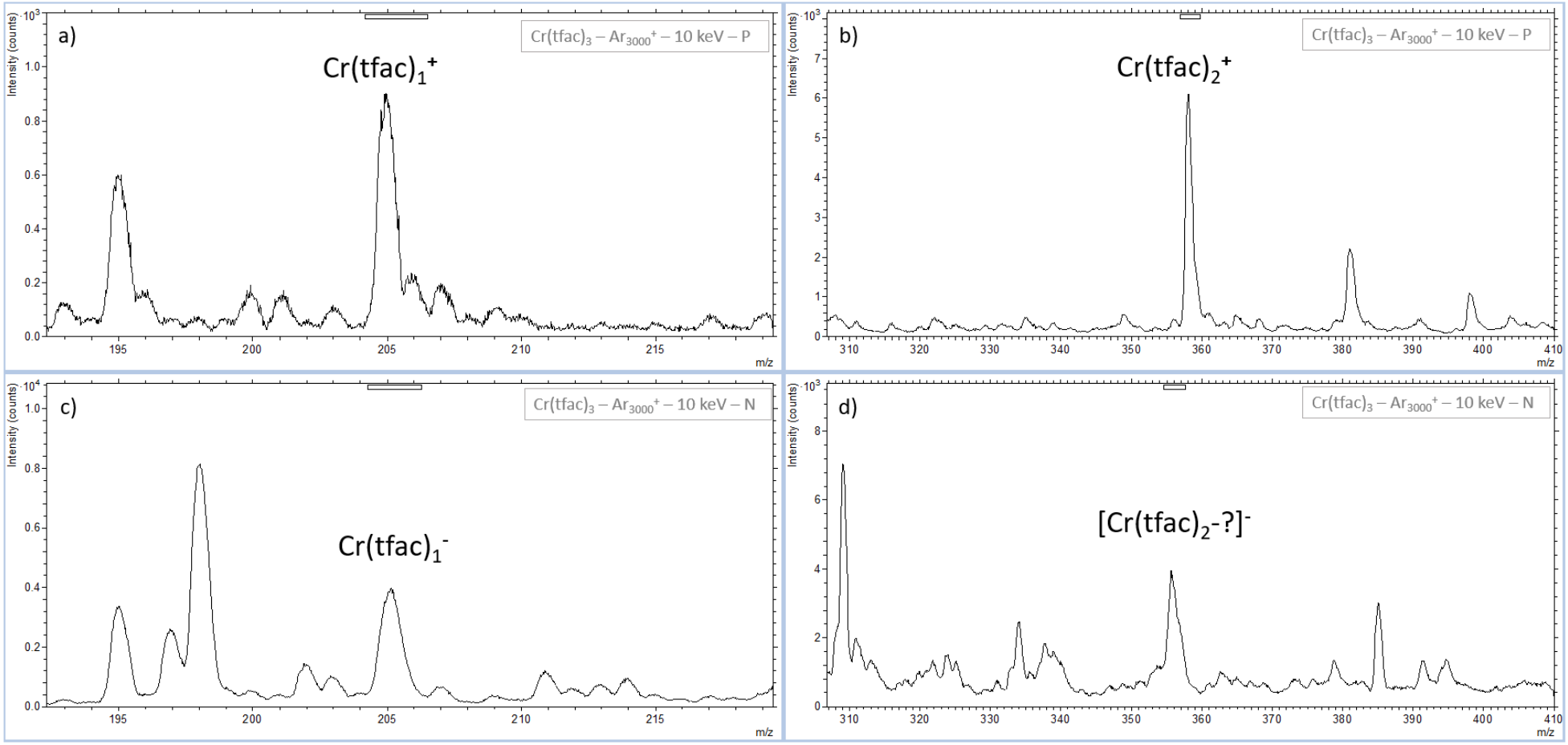

Figure 6.23: Positive (a & b) and negative (c & d) mass spectra of the $Cr(tfac)_3$ sample showing the peaks of the chromium atom bond to one tfac (a & c) and to two tfac's (b & d). Obtained under 10 keV Ar^+_{3000} cluster ion beam.

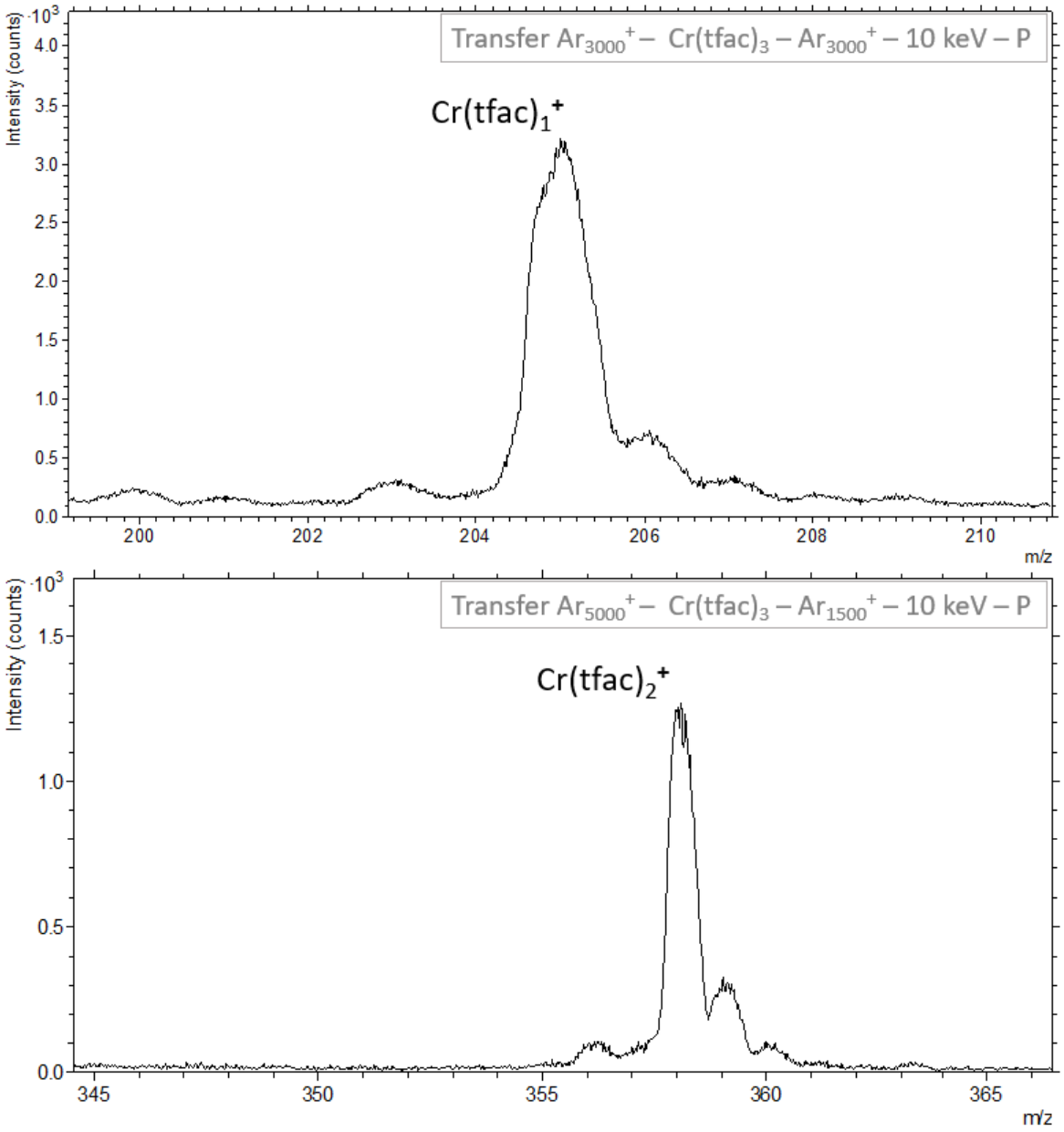

Figure 6.24: Positive mass spectra of the collectors after transfer under 10 keV Ar^+_{3000} (a) and Ar^+_{5000} (b) of the $Cr(tfac)_3$ sample showing isotopic peaks of (a) $Cr(tfac)^+_1$ and (b) $Cr(tfac)^+_2$ (monoisotopic peak at m/z 205 and 358). Obtained under 10 keV Ar^+_{3000} (a) and Ar^+_{1500} (b) cluster ion beams.

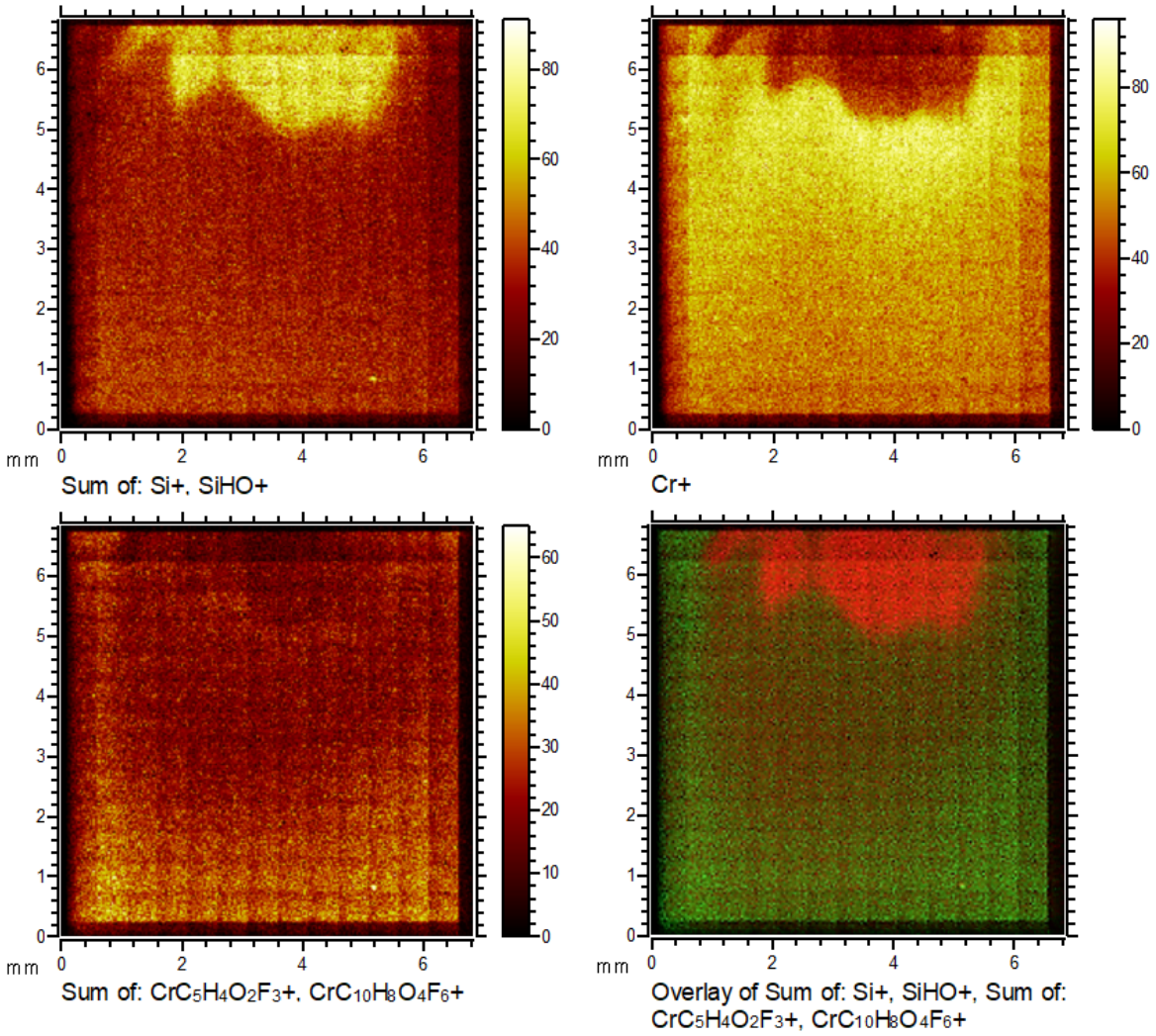

Figure 6.25: 2D SIMS mappings of the collector after transfer under 10 keV Ar^{+}_{3000} showing (upper left) sum of Si^{+} and $SiOH^{+}$ signals, (upper right) Cr^{+} signal, (down left) sum of $Cr(tfac)^{+}_{1}$ and $Cr(tfac)^{+}_{2}$ signals and (down right) an overlay between the substrate ions signals in red and complex ions signals in green.

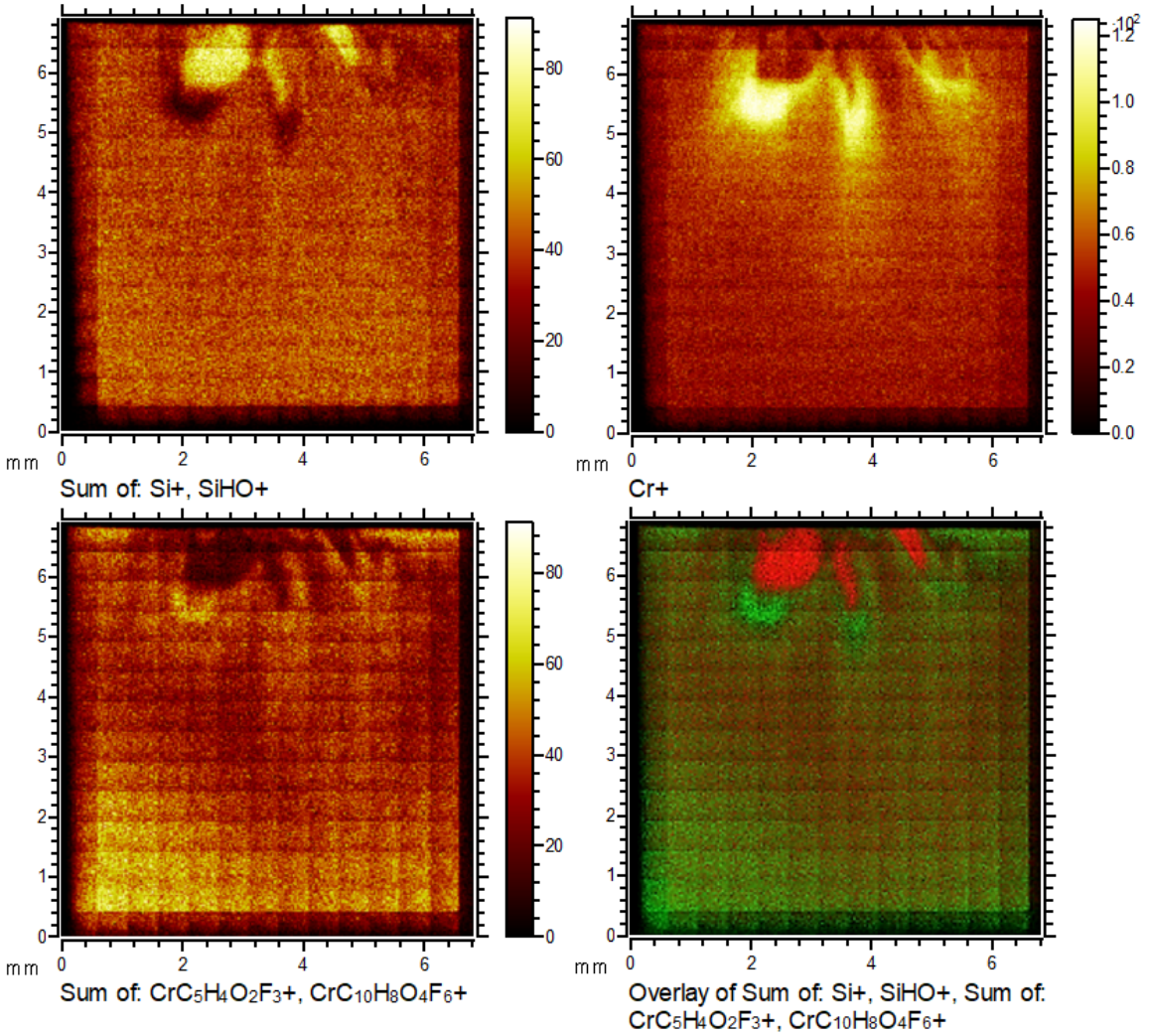

Figure 6.26: 2D SIMS mappings of the collector after transfer under 10 keV Ar^+_{5000} showing (upper left) sum of Si^+ and $SiOH^+$ signals, (upper right) Cr^+ signal, (down left) sum of $Cr(tfac)^+_1$ and $Cr(tfac)^+_2$ signals and (down right) an overlay between the substrate ions signals in red and complex ions signals in green.

6.7 Related to section 5

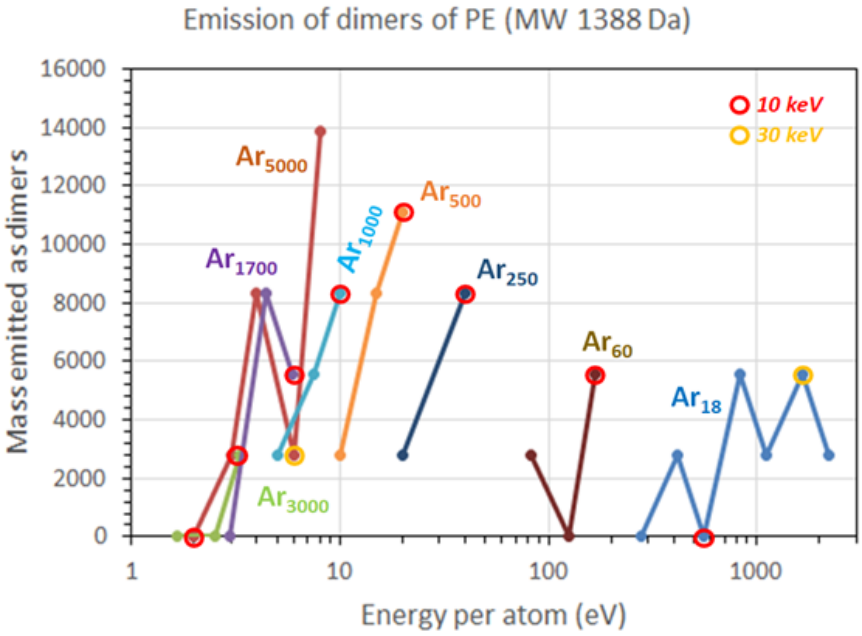

Figure 6.27: Molecular dynamics simulations showing the mass emitted as dimers in function of the cluster size and energy. Kindly provided by A. Delcorte.

Intact desorption and soft-landing of non-covalent complexes using ToF-SIMS

Master thesis presented by William Borsos

Nowadays, surfaces biofunctionalization is a subject of utmost interest, especially in medical and paramedical applications. Even if the immobilization of biomolecules from aqueous solutions has already shown efficiency, these methods suffer from negative aspects. Among others, the issues intrinsic to the drying process, such as the denaturation of the immobilized proteins, the limitation to monolayers and the poor control of spatial delivery, can reduce the achievable functions of the engineered biomaterials. Hence, researches and methods are increasingly being developed to counteract these drawbacks.

This master thesis investigates the detection and transfer of non-covalent complexes, using small bismuth and large argon cluster ion beams, with a time-of-flight secondary ion mass spectrometer (ToF-SIMS). The ultimate goal of this study is to succeed in the intact desorption from a surface and the soft-landing onto another without breaking weak interactions linking the two involved partners, in addition to covalent bonds. Two non-covalent systems have been studied in different conditions. These systems are, firstly, vancomycin, a glycopeptide antibiotic, which can specifically bind to small (acetyl-L-Lys-)D-Ala-D-Ala polypeptide and to itself by forming dimers and secondly, chromium trifluoroacetylacetonate ($Cr(tfac)_3$, *i.e.* more robust metallic complexes. Various parameters were tested: primary ion beam nature, cluster size and energy, sample thickness and substrate's hardness which are among the most impactful ones.

First, some reference analyses were achieved using Bi_5^+ and $Ar_{1500-3000-5000}^+$ beams to (i) make sure these complexes could be detected (and so desorbed intact) by ToF-SIMS and (ii) to identify their mass spectral signature. Second, these non-covalent complexes were transferred using large $Ar_{3000-5000}^+$ beams from a target, a silicon wafer on which high quantities of complexes have been deposited, onto a cleaned surface, the collector. These collectors were finally analyzed to assess if these complexes were transferred intact. A study on vancomycin fragmentation has also been achieved in function of the layer thickness, confirming previous theories and bringing additional information on ionization mechanisms of vancomycin pseudomolecular ions. Using optimized parameters, all complexes were successfully detected confirming that non-covalent complexes can be desorbed intact using ToF-SIMS. After being transferred, $Cr(tfac)_{1\text{-}2}$ complexes were detected on the collectors in positive mode. For the vancomycin-ligand complexes and the vancomycin dimers, it resulted that these were too weakly bonded to allow detection after an additional ion impact compared to the analyses. Nevertheless, intact vancomycin molecules were transferred with a semi-circular deposition pattern confirming that large argon clusters, with their low energy per atom, significantly reduced the molecules fragmentation upon ion impacts.

UNIVERSITÉ CATHOLIQUE DE LOUVAIN
Faculté des bioingénieurs
Croix du Sud, 2 bte L7.05.01, 1348 Louvain-la-Neuve, Belgique | **www.uclouvain.be/agro**